https://doi.org/10.15388/vu.thesis.577
https://orcid.org/0009-0009-3473-0611

VILNIUS UNIVERSITY
CENTER FOR PHYSICAL SCIENCES AND TECHNOLOGY

Vaidas Pudžaitis

# Surface Enhanced Infrared Absorption Spectroscopy of Biomolecular Layers and Water at Gold Surface

**DOCTORAL DISSERTATION**

Natural Sciences,
Chemistry (N 003)

VILNIUS 2023

The dissertation was prepared between 2017 and 2023 at department of Organic Chemistry at the Center for Physical Sciences and Technology.

**Academic supervisor – Prof. Habil. Dr. Gediminas Niaura** (Center for Physical Sciences and Technology, Natural Sciences, Chemistry – N 003).

This doctoral dissertation will be defended in a public meeting of the Dissertation Defence Panel:

**Chairman – Prof. Habil. Dr. Rimantas Ramanauskas** (Center for Physical Sciences and Technology, Natural sciences, Chemistry – N 003).

Members:

**Dr. Justas Barauskas** („Camurus“ International pharmaceutical company, Natural Sciences, Biochemistry – N 004),

**Dr. Rima Budvytytė** (Vilnius University, Natural Sciences, Biochemistry – N 004),

**Dr. Renata Karpicz** (Center for Physical Sciences and Technology, Natural Sciences, Physics – N 002)

**Dr. Marijonas Tutkus** (Vilnius University, Natural Sciences, Physics – N 002).

The dissertation shall be defended at a public meeting of the Dissertation Defence Panel at 11 h on 19 th of January 2024 in meeting room D401 of the of the Center for Physical Sciences and Technology. Address: Saulėtekio Ave. 3, Vilnius, Lithuania. Tel. +370 52649211, e-mail: office@ftmc.lt

The text of this dissertation can be accessed at the libraries of Vilnius University and Center for Physical Sciences and Technology, as well as on the website of Vilnius University: *www.vu.lt/lt/naujienos/ivykiu-kalendorius*

https://doi.org/10.15388/vu.thesis.577
https://orcid.org/0009-0009-3473-0611

VILNIAUS UNIVERSITETAS
FIZINIŲ IR TECHNOLOGIJOS MOKSLŲ CENTRAS

Vaidas Pudžaitis

# Biomolekulinių sluoksnių ir vandens ant aukso paviršiaus tyrimas paviršiaus sustiprintos infraraudonosios sugerties spektroskopijos metodu

**DAKTARO DISERTACIJA**

Gamtos mokslai,
Chemija (N 003)

VILNIUS 2023

Disertacija rengta 2017–2023 metais Fizinių ir technologijos mokslų centre, Organinės chemijos skyriuje.

**Mokslinis vadovas – prof. habil. dr. Gediminas Niaura** (Fizinių ir technologijos mokslų centras, gamtos mokslai, chemija – N 003).

Gynimo taryba:

**Pirmininkas – Prof. habil. dr. Rimantas Ramanauskas** (Fizinių ir technologijos mokslų centras, gamtos mokslai, chemija – N 003).

Nariai:

**Dr. Justas Barauskas** („Camurus“ tarptautinė farmacijos įmonė, gamtos mokslai, biochemija – N 004),

**Dr. Rima Budvytytė** (Vilniaus universitetas, gamtos mokslai, biochemija – N 004),

**Dr. Renata Karpicz** (Fizinių ir technologijos mokslų centras, gamtos mokslai, fizika – N 002),

**Dr. Marijonas Tutkus** (Vilniaus universitetas, gamtos mokslai, fizika – N 002).

Disertacija ginama viešame Gynybos tarybos posėdyje 2024 metų sausio mėn. 19 d. 11 val. Fizinių ir technologijos mokslų centre D401 posėdžių auditorijoje. Adresas: Saulėtekio al. 3, Vilnius, Lietuva, tel. +370 52649211; el. paštas: office@ftmc.lt

Disertaciją galima peržiūrėti Vilniaus universiteto ir Fizinių ir technologijos mokslų centro bibliotekose ir VU interneto svetainėje adresu: *https://www.vu.lt/naujienos/ivykiu-kalendorius*

CONTENTS

# ACKNOWLEDGMENTS

I am very grateful to my supervisor, prof. habil. dr. Gediminas Niaura and colleague dr. Martynas Talaikis, for their support and guidance throughout my Ph.D. project. Their expertise in vibrational spectroscopy and electrochemistry and their willingness to share new techniques and approaches with me proved to be instrumental in achieving the final results. I appreciate the help navigating the SEIRAS application and the encouragement to persevere despite setbacks.

I would also like to express my sincere gratitude to the Center for Physical Sciences and Technology and Vilnius University, for providing me with a scholarship and the opportunity to work alongside teaching assistants, which helped develop my skills and knowledge.

My dear colleague, dr. Jūratė Senvaitienė from the Lithuanian National Museum of Art, Pranas Gudynas Center for Restoration, deserves a special mention for her support and assistance with my research. Her time, expertise, and unwavering commitment to my success were invaluable.

Last but certainly not least, I want to express my gratitude towards my dear wife, Rasa, for her patience, understanding, and support throughout this journey.

# INTRODUCTION

*„God made the bulk; surfaces were invented by the devil"*[1]

Wolfgang Pauli

Surfaces and interfaces have unfathomable significance for all life-supporting processes, whether simple water condensation or a complex biomolecule interaction in catalysis, energy transformation, or electron transfer at the lipid membrane. It is reasonable to believe that interfaces are one of the main factors that helped "accelerate" the appearance of the first self-replicating molecules, which evolved into life forms as we know them today.[2] A lot of studies have been devoted to the topic, which in one way or another is related to the interactions at the interface, from the surface tension[3] to the cell membrane.[4] Interactions at the structurally ordered molecular layers, for example, self-assembled monolayers (SAMs) or phospholipid membranes, are well known and documented. It is unfortunate that molecules on the surface may have completely different properties than the molecules in bulk. Therefore, our knowledge of the bulk material could not be simply applied to surface-bound molecules. For that reason, many modern instrumental methods have been adapted to investigate interface processes. These methods encompass atomic force and electron microscopy, mass spectrometry, neutron and X-ray techniques, microfluidics, and optical techniques.[5] Methods based on optical principles, primarily in visible and infrared light range, are frequently used to study biomolecules. Modern optical spectroscopy allows for the direct observation of biomolecular interactions at interfaces with a very high sensitivity. **Surface enhanced infrared absorption spectroscopy** – SEIRAS is one of these methods. It emerged in the last couple of decades but has only found its application in studies of biological membranes and proteins during the last decade.[6] Additionally, SEIRAS is only one of a few techniques capable of directly observing water molecules behavior at interfaces. Coupled with in situ studies of SAM and lipid membranes, it became an unmatched tool for this research study.

In this thesis, a variety of techniques were used. Attenuated total reflection (ATR)-SEIRAS was the primary optical method integrated with potentiometry. This setup used gold-coated silicon ATR crystal as a working electrode. Conventional infrared (IR) spectrometry, predominantly in transmission and ATR configuration, was applied to collect vibrational spectra of bulk compounds. In addition, isotopic substitution, scanning electron microscopy, and density functional theory (DFT) modeling were

utilized as supplementary techniques for vibrational spectroscopy data interpretation.

This research was motivated by the ambitious objective of investigating the assembly, structure, and dynamics of SAMs, model lipid membranes, and pore-forming membrane proteins at electrified interface. It sought to unravel the complexities of their mutual interactions and their responses to environmental stimuli. It also examined how the variations in the gold substrate's electric potential affect the assembled layers' characteristics and the extent to which it could be regulated. These inquiries were just a subset of the broader questions aimed at understanding better the formation of biologically relevant synthetic membranes and their interactions with surrounding entities.

**This work aimed** to study the structural changes in SAMs, artificial bilayer lipid membranes (BLMs), and membrane interaction with the pore-forming toxin melittin in situ using the SEIRAS technique.

**The objectives of the work**

1. To form and characterize SAMs formed from imidazole ring terminated IMHA and fragment molecules using ATR-SEIRAS.
2. To examine hydrogen bonding interaction and electric potential dependence on the functional imidazole ring group structure at the solid support-solution interface.
3. To investigate the formation of the anchoring mixed self-assembled monolayers and the development of the tethered lipid bilayers on these mixed SAMs.
4. To comparatively analyze the water structure near the biomimetic tethered and hybrid bilayer lipid membranes (tBLM and hBLM) and under varying electric potential conditions.
5. To determine the dielectric constant of confined water in the submembrane space of tBLM using a reporter molecule.
6. To investigate the impact of environmental pH changes on the structure and properties of tBLM.
7. To study the interactions of pore-forming protein melittin with tBLM and hBLM using time-resolved ATR-SEIRAS.

**The novelty of the work**

The essential role of histidine in protein structure and catalytic function primarily arises from the interactions facilitated by its side chain, imidazole ring (Im).[7] Im serves as an aromatic system, participates in hydrogen bond interactions, and coordinates metal (II) cations through its nitrogen's lone electron pair.[8] Among these interactions, hydrogen donating and accepting

bonds are frequently observed at charged interfaces. Despite their biological significance, investigating hydrogen bond interactions at electrochemical interfaces remains challenging due to the absence of suitable experimental techniques.

The hydrogen bonding interaction strength of histidine's imidazole ring (Im) with its immediate environment was studied for the first time using electrochemical ATR-SEIRAS. Additionally, Im-bearing molecule adsorption and self-assembly on the Au surface were analyzed. The relation between the concentration of the imidazole group bearing alkanethiol molecules on the surface and the orientation of the Im was demonstrated. It was shown that for SAMs composed of surface alkanethiol molecules with Im end groups, the bulky ring precludes the formation of an optimal arrangement, affecting the monolayer formation kinetics.

Theoretical analysis revealed the sensitivity of =C–H stretching modes frequencies towards imidazole ring hydrogen bonding strength. Subsequently, a reversible dependence between the external electric field and hydrogen bonding interaction strength between Im and water was defined. Also, the transition to a negative potential was linked with Im's reversible orientation changes, evidenced by the alterations in the relative intensities of two Im =C–H vibrational modes at 3150/3115 $cm^{-1}$.

The behavior of water molecules at interfaces and submembrane layers is critical as it can significantly impact the adsorption, organization, and stability of SAM and BLM and their interactions with other biomolecules.[9,10] However, directly measuring water dielectric properties at thin interface layers presents a formidable challenge, even with the latest highly sensitive techniques. In this work, for the first time, the structure and potential-responsive behavior of water molecules within the inner layer of the tBLM membrane were probed by ATR-SEIRAS. This research also touched on water involvement in model membrane formation and their reaction to electrical stimuli once formed. A spectrometric marker was employed to investigate water's dielectric properties in the tBLM system's submembrane region. Furthermore, the study explored how pH affects water within the tBLM system, correlating observed shifts in submembrane resistivity to changes in ion concentrations, as opposed to alterations in membrane integrity.

To better understand the mechanisms behind pore-forming peptides, such as melittin, their interactions with biomimetic tBLM and hBLM systems using the in situ SEIRAS method were investigated. This approach is crucial as it allows us to directly observe and analyze these interactions at the molecular level, providing valuable information into their mechanism of action and

potential applications. Notably, the tBLM system, with its submembrane space, offers a unique opportunity to study peptide behavior in a more biologically relevant environment compared to the hBLM system, which lacks a submembrane space.

Distinct lipid-protein interaction behaviors were identified and linked to membrane structure. During the initial stages, it was observed that toxin accumulates on the membrane and causes disturbance and water expulsion in both the hBLM and tBLM systems. Subsequently, the removal of water molecules from the vicinity of the gold surface and changes in the SAM layer confirmed an increase in melittin molecules in the submembrane space of the tBLM system. Notably, both systems exhibited membrane disruption after incubation times exceeding 90 minutes, attributed to the aggregation of melittin with lipids.

**The defense statements of the work**:

1. Bulky imidazole ring group precludes neatly packed SAM formation from IMHA molecules and affects the dynamics of monolayer formation.
2. Electric potential excursion from 0.3 to –0.5 V reduces hydrogen bonding strength at the imidazole ring of the IMHA molecule.
3. The tBLM submembrane reservoir contains water with altered, solid-like properties, with considerably decreased dielectric constant of the tBLM submembrane reservoir.
4. pH shift from acidic to neutral induces a surge in ion concentration in the submembrane
5. The interaction between melittin and tBLM induces a rapid transition of melittin's secondary structure from unordered to α-helix within less than 15 seconds. Following this structural change, melittin then accumulates in the submembrane space.

**Contribution of the author**

All the IR, ATR, and ATR-SEIRAS experiments were performed in the Spectroelectrochemistry laboratory, Department of Organic Chemistry, Center for Physical Sciences and Technology. SEM measurements were performed in the Pranas Gudynas Center for Restoration at the Lithuanian National Museum of Art. The author did all microscopy, spectroscopy, and electrochemical measurements. DFT calculations and multilamellar vesicle preparations were carried out by dr. Martynas Talaikis. Data analysis and preparation of published articles were performed by the author and co-authors of manuscripts.

# LIST OF ABBREVIATIONS

| | |
|---|---|
| AOI | Angle of incidence |
| AMP | Small antimicrobial peptide |
| ATR | Attenuated total reflection |
| BLM | Bilayer lipid membranes |
| βME | β-mercaptoethanol |
| CV | Cyclic voltammetry |
| DFT | Density functional theory |
| DOPC | 1,2-dioleoyl-sn-glycero-3-phosphocholine |
| DPPC | 1,2-dipalmitoyl-d62-sn-glycero-3-phosphocholine |
| DTGS | Deuterated triglycine sulfate |
| EIS | Electrochemical impedance spectroscopy |
| FAC | Face angled crystal |
| FIR | Far-infrared |
| FTIR | Fourier transformation infrared spectroscopy |
| fBLM | Floating bilayer lipid membrane |
| hBLM | Hybrid bilayer lipid membrane |
| IRE | Internal reflection element |
| IR | Infrared |
| IRRAS | Infrared reflection absorption spectrometry |
| Im | Imidazole ring |
| LSP | Localized surface plasmon |
| LSPR | Localized surface plasmon resonance |
| MCT | Mercury cadmium telluride |
| MIR | Middle-infrared |
| MLV | Multilamellar vesicle |
| MHP | N-(6-mercapto)hexylpyridinium |
| MSSR | Metal surface selection rule |
| NIR | Near-infrared |
| OCP | Open circuit potential |
| PEG | Polyethylene glycol |
| SAM | Self-assembled monolayer |
| SEM | Scanning electron microscope |
| SEIRAS | Surface enhanced infrared absorption spectroscopy |
| SERS | Surface-enhanced Raman spectroscopy |
| sBLM | Suspended bilayer lipid membrane |
| SPR | Surface plasmon resonance |
| TDM | Transition dipole moment |
| tBLM | Tethered bilayer lipid membrane |
| UV | Ultraviolet |
| VIS | Visible |
| WC14 | 20-tetradecyloxy- 3,6,9,12,15,18,22-heptaoxatricontane-1-thiol |

# 1. THEORY OVERVIEW

## 1.1. Vibrational spectroscopy

Vibrational spectroscopy is a group of optical techniques that provides information on molecular systems by analyzing vibrations of a wide range of organic and inorganic compounds. The methods include infrared spectroscopy, Raman spectroscopy, sum frequency generation spectroscopy, and others (terahertz, photoacoustic spectroscopy, etc.). The spectral range in regard to the full light spectrum is shown in Figure 1.

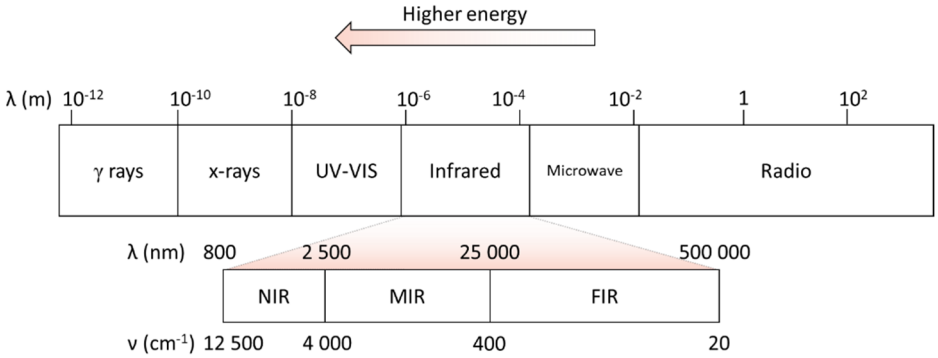


Figure 1. Schematic representation of light spectrum zones from highest to lowest energy. The infrared region is divided into near, middle, and far regions (adapted from [11]).

Light scattering is mainly associated with Raman spectroscopy, whereas the transmission and absorption are more related to infrared spectroscopy (IR). When light passes through the molecular system, it becomes absorbed at frequencies corresponding to particular molecules' transitions (Figure 2). In the case of ultraviolet (UV) and visible (VIS) light, energy is sufficient to promote electron transitions to an excited electronic state and is called electronic spectroscopy. Infrared (IR) light has enough energy to promote molecular transitions from one vibrational level to another, inducing electron redistribution and causing vibrational amplitude and rotational frequency increase. The frequency-dependent light intensity changes are then plotted to give a vibrational spectrum.[12]

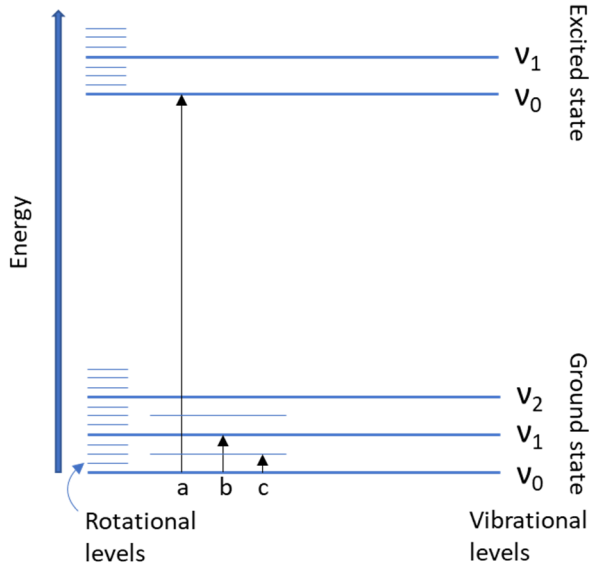


Figure 2. Diagram for molecular energy levels. Electronic (a), vibrational (b), and rotational (c) transitions are displayed by the black arrows (adapted from [12]).

Various dimensions describing energy metrics for absorption can be met throughout literature, but the wavenumber $\tilde{\nu}$ is most commonly met. It is expressed in $cm^{-1}$ and has a relation:

$$\tilde{\nu} = \frac{1}{\lambda_0} = \frac{\nu}{c}, (1)$$

were $\lambda_0$ – wavelength in vacuum, $\nu$ – frequency, $c$ – speed of light. Absorption is the process by which a molecule takes in light energy at a specific wavelength and undergoes a vibrational transition to an excited vibrational level. According to the Plank equation describing the energy value of two energetical states:

$$E = E_1 - E_2 = h\nu, (2)$$

where h is Planck's constant, energy ($E$) is directly proportional to vibrational frequency, so the higher $\nu$ value represents the higher energy of the vibration.

The IR spectrum is typically divided into three regions: the near-infrared (NIR) region, the mid-infrared (MIR) region, and the far-infrared (FIR) region. The NIR region covers the range from 12500 to 4000 $cm^{-1}$ and is mainly used to analyze overtone and combination bands of functional groups. The MIR region covers the range from 4000 to 400 $cm^{-1}$ and is the most

commonly used region for IR vibrational spectroscopy. The FIR region covers the range from 400 to 10 $cm^{-1}$ and is used to analyze lattice vibrations and rotational transitions.[11] In the MIR range of vibrational spectroscopy, the position and intensity of the absorption bands in the spectrum provide information about the functional groups and the chemical structure of the molecules. The position of the absorption bands is determined by the energy required to excite a particular vibrational mode, which is related to the atom masses and the stiffness of the chemical bond involved in the vibration. The harmonic oscillator model describes the frequency of molecular vibration. Atoms, considered as a point mass, are connected by a weightless spring. And their vibrational frequency $\nu$ is then equal:

$$\nu = \frac{\sqrt{k/m_r}}{2\pi}, \quad (3)$$

where $k$ – bond force constant and $m_r$ – reduced mass ($\frac{1}{m_r} = \frac{1}{m_1} + \frac{1}{m_2}$). This equation shows that vibrational frequency is directly proportional to bond strength and inversely proportional to the reduced mass of bond-forming atoms. A good example of how the force constant affects vibrational frequency is given for carbon-carbon bonds, which are essential to almost every element of organics (Figure 3). The force constant increases as the bond strength increases from single to triple bond. Correspondingly, the vibrational frequency of these bonds also increases.[13]

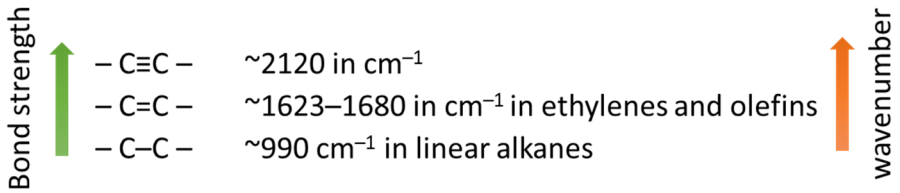


Figure 3. Carbon bond strength influence over vibrational frequency.

Moreover, as different environments and molecule structures influence bond strength, IR spectroscopy provides information on molecular surroundings and structure. Overall, IR vibrational spectroscopy is a versatile and powerful technique with a wide range of applications in many fields of science and technology. Its ability to provide information about the chemical structure and dynamics of molecules makes it an indispensable tool for studying molecular systems at the atomic level.

### 1.1.1. FTIR spectroscopy

Fourier transformation infrared spectroscopy (FTIR) is a spectroscopic method based on the IR light absorption of matter. The absorption is wavelength dependent, and the ratio of the radiation intensity that passed through the sample ($I$) to the original intensity ($I_0$) results in the transmission spectrum, which is expressed as a transmission ratio ($T$) with values between 0 and 1, therefore $T=I/I_0$. T is typically converted to absorption (Abs) using a logarithmic transformation:

$$\mathrm{Abs} = -\log \mathrm{T} \quad (4)$$

Spectra in transmission are more often met in older literature, whereas in newer ones, the absorbance spectrum dominates. Besides the subjective view of somehow more straightforward to read upwards-looking peaks, absorbance is linearly dependent on the analyte concentration, which is described by the Beer-Lambert law:

$$\mathrm{Abs} = \varepsilon c l, \quad (5)$$

where $\varepsilon$ – molar absorption coefficient ($M^{-1}cm^{-1}$), $c$ – analyte concentration (M), and $l$ – optical path length (cm). Overall, the IR spectrum can provide information about:

**1) Chemical structure of molecules**. Every molecule has a different set of bonds, which results in a unique absorption spectrum. As discussed above, the MIR range provides the most information on molecular vibrations, mainly the 600–1400 cm–1 range, often called the fingerprint region. In contrast to the higher frequency region above 2700 cm–1, which has information mostly on C–H stretching and wide O–H and N–H vibrations common to many compounds, the fingerprint region has a rich set of stretching, bending, and combination vibrational bands unique for a particular molecule. And even in a complex mixture of molecules, it can be instrumental in identifying or quantifying the molecules of the composition. For example, in Figure 4, a complex IR spectrum of milk is presented. Spectral modes of water, proteins, sugars, and fats may be identified. In higher frequency regions, vibrational bands assigned to stretching O–H, N–H, and C–H vibrations overlap from many compounds and are difficult to assign to a particular molecule. Contrary, from the fingerprint region, biomolecular entities may be identified. For example, the stretching C=O vibration at around 1730 cm–1 is related to lipids, amide I and II vibrations at 1650 and 1550 cm–1 are associated with proteins, and the stretching C–O bands at the ~1000 cm–1 region belongs to sugars.

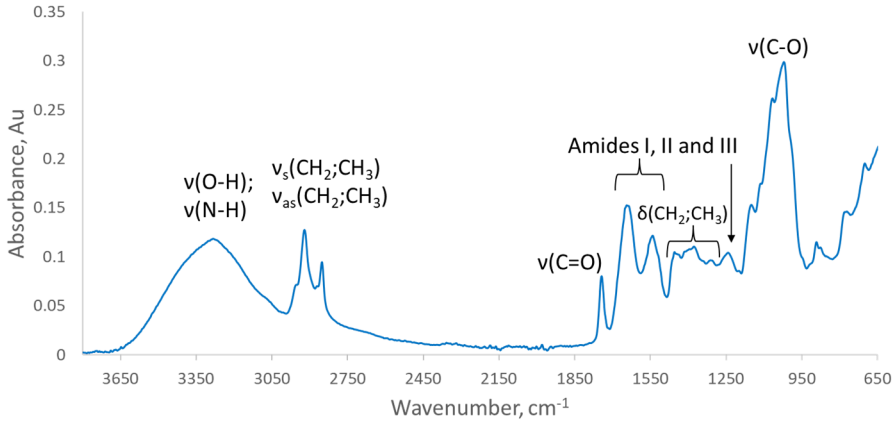


Figure 4. The FTIR spectrum of milk measured with diamond crystal attenuated total reflection (ATR) cell.

**2) Hydrogen bonding** is ubiquitous in biochemical systems, and it strongly affects the vibrational spectrum because it modulates bond stiffness. Hydrogen bonding effectively decreases the related group's vibrational frequency of stretching motion and increases the frequency of the bending motion. IR is one of the few techniques that can report directly on the changes in hydrogen bonding interaction.

**3) Strength of the chemical bond.** The strength of a chemical bond is related to its force constant, which in turn affects the vibrational frequency. The force constant measures how stiff a bond is and how much energy is required to stretch or compress it. The stronger the bond, the higher the force constant and the higher the vibrational frequency. Conversely, weaker bonds have lower force constants and lower vibrational frequencies. This means that IR spectroscopy can study the strength of chemical bonds and provide important insights into molecular structures (see Figure 3).

**4) Steric interferences.** The vibrational spectrum of a molecule can be affected by its conformation and the degree of conformational freedom it has. When a molecule has more conformational freedom, its vibrational modes are broader and less well-defined. This is because the different conformations of the molecule can have slightly different bond lengths and angles, which can lead to slight variations in vibrational frequencies. On the other hand, molecules with less conformational freedom have sharper and more well-defined vibrational modes. The molecular structure is more restricted, resulting in more consistent bond lengths and angles. By analyzing the vibrational spectrum of a molecule, it is possible to gain insights into its conformational freedom and how it affects its behavior in different environments.

As an example, the C=C bond in lipids is affected by isomerization. In particular, the stretching vibration of the C=C bond is very sensitive to the molecule's orientation, which is affected by conformational freedom. In a trans conformation, the C=C bond is generally more rigid and has a higher vibrational frequency than the cis conformation molecule. Typically, the vibrational frequency of the C=C bond in lipids is observed in the MIR range of the IR spectrum, at around 1650–1700 $cm^{-1}$. [14,15] By analyzing the vibrational frequency of the C=C bond, it is possible to gain insights into the conformational freedom and degree of unsaturation of the lipid molecule, which can, in turn, provide information about the lipid's biochemical properties and functions.

**5) Conformation and bond angles.** Individual bond vibrations may be coupled to other vibrations and are molecular geometry sensitive. As a result, it occasionally offers details on the molecule's three-dimensional (3D) structure. It is essential in biochemical applications, such as protein analysis. For example, the amide bond is sensitive to the protein backbone's conformation and hydrogen bonding pattern. Several vibrational spectral modes characterize the amide bond. The most informative are the amide I and amide II bands, which correspond to C=O stretching and C=N stretching coupled with N–H bending, respectively.[16] The amide I band is particularly sensitive to the secondary structure of the protein, such as alpha helices, beta sheets, or random coils, and can be used to determine the protein conformation. The amide I band of alpha-helical and beta-sheet proteins are located at around 1650 and 1630 $cm^{-1}$, respectively, while random coil proteins have a broader and less defined amide I band.[16] The amide II band, on the other hand, is less sensitive to the secondary structure and is influenced by the hydrogen bonding pattern of the protein backbone. The position and shape of the amide II band can provide information on the degree of hydrogen bonding between neighboring peptide units.[17]

**6) Electric fields.** Locally or externally created potential impacts molecular electron density, which affects vibrational frequencies and is still a new field known as electric field-induced spectroscopy. This effect is similar to hydrogen bonding, which can also modify the electron density distribution of a molecule and influence its vibrational frequencies.

Strong local electric field is present in molecules that contain fully or partially charged atoms, for example, the active site of enzymes, where the electric field may act as a force for the catalytic reaction. In dehalogenase enzymes, the electric field in the active site has been shown to play a role in catalysis.[18] Additionally, there is an inverse correlation between the C=O stretching frequency of carboxyl groups (bands above 1740 $cm^{-1}$) and the

dielectric constant $\varepsilon$. Indicating that the interfacial electric field can significantly impact the vibrational frequencies of carboxyl groups, observed in IR spectra.[19]

**7) Chemical reactions and molecular dynamics.** IR spectroscopy can provide insights into both. Changes in the vibrational spectrum during a reaction can give information on changes in chemical bonds and molecular structures, making it helpful in studying reaction mechanisms and monitoring the progress of a reaction in real time.[20–22] In addition, time-dependent changes in vibrational frequencies can provide insights into molecular dynamics, such as bond rotations and vibrations, as well as other types of motion like hydrogen-bond breaking and forming.[23]

**8) Surface chemistry**. IR spectroscopy can study the surface chemistry of materials, including the adsorption and desorption of molecules on surfaces. One advantage of IR spectroscopy for surface analysis is its ability to probe only a few molecular layers into a material. This allows to analyze the surface properties without interference from the bulk properties of the material.

### 1.1.2. SEIRAS – principles of surface enhancement for IR light

SEIRAS is a vibrational spectroscopy technique that utilizes localized surface plasmon resonance to enhance the infrared absorption of material in direct contact or near the nanostructured Au, Ag, or other plasmonic material. The phenomenon of surface plasmon resonance (SPR) involves the oscillation of electrons in nanostructures in response to light, producing highly confined areas known as hotspots with intense optical fields. This phenomenon is related to significantly enhanced light-matter interaction, which leads to increased molecular sensitivity in various techniques that take advantage of SPR like Raman, fluorescence, and infrared absorption spectroscopies.[24,25] Surface-enhanced infrared absorption spectroscopy proved a powerful surface-sensitive technique utilizing the SPR enhancement phenomenon. With advantages similar to those of infrared reflection absorption spectrometry (IRRAS), including the metal surface selection rule (MSSR) and the ability to probe molecular systems in absorbing environments like water, SEIRAS has recently become a desirable tool for the analysis of molecular interactions at the metal interface, showing great potential for chemical and biological applications.[26–28]

**Recognition of electric field enhancement effect induced by the surface.** It was inevitable that the 1970s discovery of surface-enhanced Raman spectroscopy (SERS) would lead to the development of SEIRAS,[29,30]

which was experimentally demonstrated by Hartstein in 1980[24] and later verified by Hatta.[31,32] After a couple of decades, reports on the practical and theoretical aspects of SEIRAS appeared.[25,33] The importance of SEIRAS was recognized with the first symposium held at the Pittsburgh Conference in 1997 (March, Atlanta). The main reasons SEIRAS fell behind SERS in terms of development time were the need for more precise instrumentation and the generally higher signal-to-noise ratio due to the lower infrared (IR) energy level.[34,35] Unlike Raman scattering, where the signal is generated by scattered light, IR absorption involves direct radiation absorption by the molecule, and the signal strength is proportional to the amount of radiation absorbed. However, the near-field enhancement effect in SEIRA is not as pronounced as in SERS, especially for weak vibrational oscillators. In SEIRA, the enhancement is proportional to the square of the near-field amplitude enhancement (see equation 6), whereas in SERS, it is proportional to the fourth power.

$$A \propto \left|\frac{\partial \mu}{\partial Q} \cdot E\right|^2 = \left|\frac{\partial \mu}{\partial Q}\right|^2 |E|^2 \cos^2 \theta \qquad (6)$$

In here, absorption is proportional to the square of the derivative of dipole moment ($\mu$) with respect to normal coordinate ($Q$) $\partial\mu/\partial Q$ multiplied by the electric field exciting molecule and to the angle $\theta$ between $\partial\mu/\partial Q$ and $E$.[25]

Nonetheless, molecular absorption has a larger cross-section than Raman scattering, as shown in Figure 5, which makes it a more direct process for detecting molecular vibrations.[35–38]

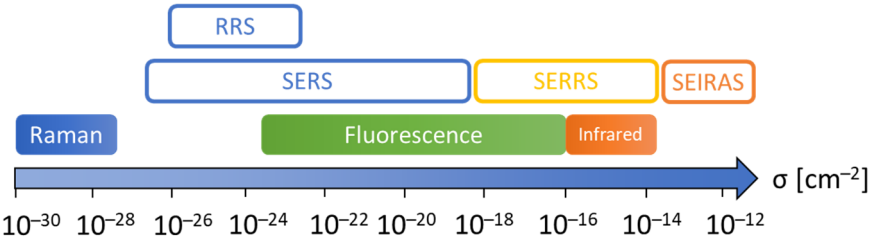


Figure 5. Comparison of different optical method cross sections. Abbreviations: RRS, resonance Raman scattering; SERS, surface-enhanced Raman scattering; SERRS, surface-enhanced resonance Raman scattering (adapted from [36])

Similar to SERS, the overall SEIRAS enhancement is powered by two distinct mechanisms: electromagnetic and chemical.

**The electromagnetic mechanism** is considered to have a predominant role in IR light enhancement. When IR electromagnetic radiation interacts with a metal-dielectric interface, free surface electrons are excited and form a collective motion confined by the nanoparticle. This is known as localized surface plasmons (LSP) (Figure 6). When the vibration frequency of the LSP

matches the frequency of the IR light, a localized surface plasmon resonance effect (LSPR) is created. The frequency of LSPR depends on the metal used and the shape and size of the nanoparticles (aspect ratio η=a/b as in Figure 6).

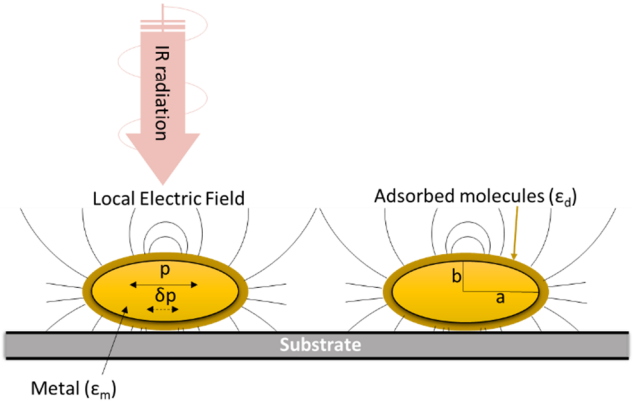


Figure 6. Illustrates the electromagnetic enhancement mechanism in SEIRAS on metal surfaces. In this mechanism, ellipsoid-shaped metal particles are polarized by the incoming IR radiation, resulting in dipole changes that create a localized electric field around the particles stronger than the incident photon field. Adsorbed molecule layer interacts with this stronger field, and their absorbance of incoming IR radiation is enhanced if particular requirements are met, such as transitional dipole moment direction and frequency (adapted from [25]).

The electromagnetic field formed around the metal particles due to LSPR is greater than the incident photon electromagnetic field. Adsorbed molecules with dielectric function $\varepsilon_d$ interact with this field and change their vibrational states. The induced field is polarized along the particle's surface normal, and its strength rapidly diminishes further from the surface. It is represented by the equation:

$$|E_{\text{local}}|^2 \propto \left(\frac{a}{a+b}\right)^6, \qquad (7)$$

where a represents the local radius of curvature of the island (Figure 6). Osawa[25] showed that the simulated peak intensity of a model molecule on a thin 5 nm gold layer is more significant, up to only around 10 nm of molecular layer thickness, compared with the system without a gold layer (Figure 7). SEIRAS is, therefore, highly sensitive to molecules located in the immediate vicinity of the plasmonic surface, typically within 10 nm.[39]

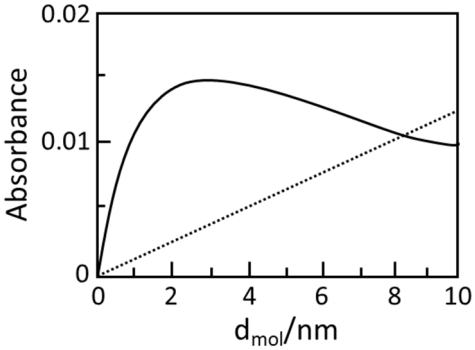


Figure 7. Simulation of model molecule peak intensity on a surface with a 5 nm Au layer (solid line) and without (dashed line) plotted against the thickness of the molecular layer, $d_{mol}$ (adapted from [25]).

SEIRAS is therefore highly sensitive to molecules located in the immediate vicinity of the plasmonic surface, typically within 10 nm.[39]

However, overall electromagnetic enhancement for middle-infrared is less than 10 times (as shown in Figure 8), which is significantly lower than the enhancement factors observed experimentally in SEIRAS, typically 10 to 1000 times. This suggests that other factors besides electromagnetic enhancement contribute to the SEIRAS effect. Furthermore, SEIRA has been observed on transition metals such as Pt, Ni, and Pd, which do not exhibit plasmon excitation in the visible–MIR region, indicating that electromagnetic enhancement alone is not the sole contributing factor.[40–42]

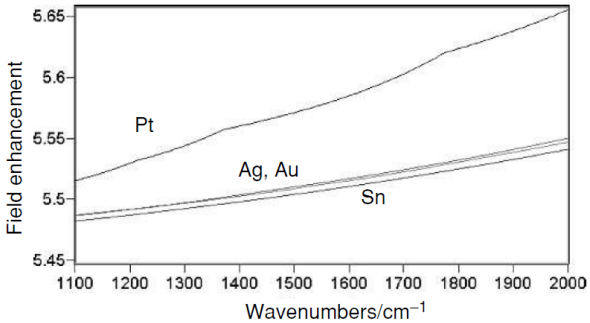


Figure 8. Calculations showing the average field enhancement in vacuum for isolated spheroids of Pt, Ag, Au, and Sn, with major axes of 90 nm and minor axes of 30 nm (adapted from [43]).

The effective medium theory considers the roughness of the metal surface as an active factor in SEIRA, leading to a more accurate explanation of the SEIRAS enhancement mechanism. When a surface is formed by metal spheres smaller than the wavelength of light, a composite medium of metal, adsorbed molecules, and an environment is formed. Due to the roughness of the metal

surface, such a medium has a broad absorption in the near and middle IR regions. By exciting with IR light, the induced dipole of the metal is coupled with the oscillating dipole of the adsorbed molecules, resulting in a change in the metal's dielectric function. As a result, the effective medium has higher absorbance at the analyte's vibrational frequency. Due to the larger volume and higher metal absorption coefficient, the contribution from the effective medium absorption becomes dominant to the surface enhancement.[44] Metal islands, therefore, act as signal enhancers in SEIRAS experiments.[25]

**Chemical mechanism** is another important factor contributing to the SEIRAS signal enhancement, although it is weaker than the electromagnetic mechanism.[45] Chemically adsorbed molecules on a metal surface show a more significant enhancement than physically adsorbed ones.[46,47] This is due to changes in their absorption coefficient $|\partial\mu/\partial Q|^2$.[48] Charge oscillations between molecular orbitals and metal surface increase the absorption coefficient.[49,50] Although the complete chemical mechanism remains unclear, there are experimental findings that suggest the presence of chemical interactions between the surface and molecules.[25,51]

In conclusion, SEIRAS is influenced not only by electromagnetic and chemical enhancements but also by the surface selection rule and preferred orientation of molecules on the metal surface. The absorption of IR light is greater for vibrational modes perpendicular to the surface than bulk solvent molecules without a specific direction. Furthermore, adsorbed molecules generally display a distinct orientation relative to the surface. Considering that the space average of $\cos^2\theta$ is 1/3 for randomly oriented molecules, the orientation effect can offer a maximum enhancement factor of three for vibrational modes with dipole changes parallel to the electric field (E).

### 1.1.3. Attenuated Total Reflection (ATR)

**Importance of hardware configuration.** SEIRAS experiments can be performed using either transmission or reflection hardware configuration. The ATR configuration has a significant advantage over the transmission configuration as it allows for probing samples in IR-absorbing environments, such as $H_2O$. This has led to ATR becoming the standard configuration in SEIRAS, sometimes referred to as ATR-SEIRAS. In ATR, reflection can be measured through external and internal configurations (Figure 9). The internal reflection configuration, the Kretschmann configuration, is the most commonly used in SEIRAS.

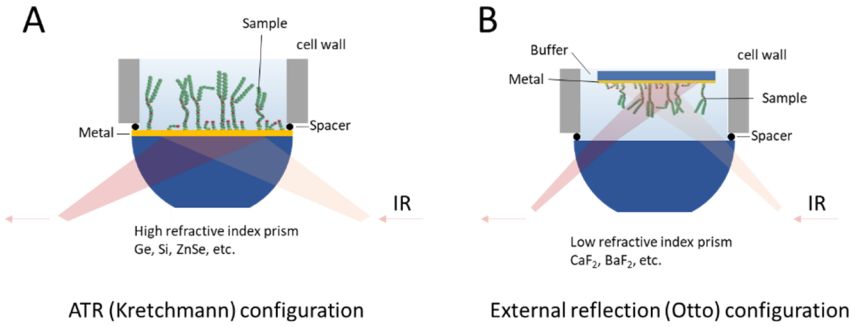


Figure 9. Schematic representation of internal (A) and external (B) reflection hardware configurations for IR experiments.

The throughput of an ATR crystal critically depends on the angle of the incident (AOI) at which light passes through it. Manufacturers offer fixed or variable-angle ATR assemblies that can fit most conventional FTIR spectrometers to accommodate different experimental setups. However, to achieve a successful SEIRAS experiment, several variables need to be considered.

The internal reflection element, the crystal, is the primary component of every ATR setup. Materials suited for ATR prism must have a high refractive index and fulfill relation sin (AOI) > $\eta_s/\eta_p$ (Figure 10A), where η represents the refractive index of the sample (s) and the prism (p). Moreover, as it is commonly phrased, $\eta_p$ must be bigger than $\eta_s$, or of a higher optical density material.

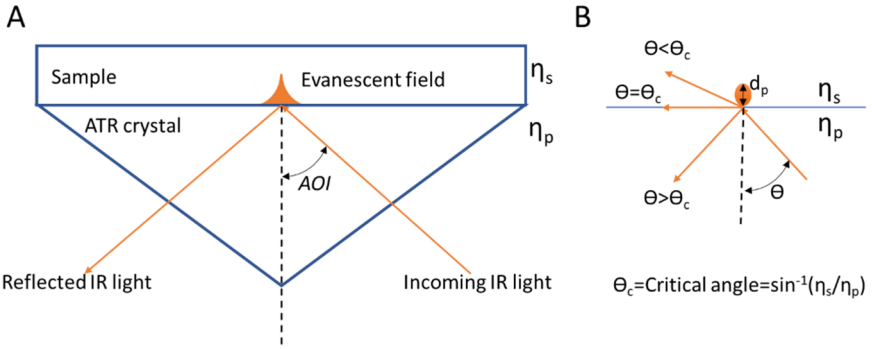


Figure 10. Principal schematics of one reflection ATR prism experiment (A). Reflected light angle dependence in relation to critical AOI (B).

The critical angle ($\Theta_c$) of the incoming IR light must also be considered to achieve total reflection conditions (Figure 10B) which can be calculated using Snell's law relation $\sin^{-1}(\eta_s/\eta_p)$ if refraction indexes of sample and prism

materials are known. Table 1 summarizes the parameters of several commonly used materials used as ATR prisms.

Table 1. Optical and physical parameters of ATR prism materials. *Calculated at 1000 $cm^{-1}$ wavenumber and sample refractive index of 1.4 where applicable (adapted from [11]).

| | *$d_p$, μm @ 45/60 deg | $\Theta_c$, deg | η | Hardness, MP | Spectral range, $cm^{-1}$ |
|---|---|---|---|---|---|
| **Ge** | 0.65/0.50 | 22 | 4.0 | 7644 | 5000–550 |
| **ZnSe** | 1.66/1.06 | 40 | 2.4 | 1274 | 20000–500 |
| **Diamond** | 1.66/1.06 | 40 | 2.4 | 88200 | 50000–2500<br>1600–0 |
| **Si** | 0.81/0.61 | 26 | 3.4 | 11270 | 5000–400 |

*Depth of light penetration

However, total internal reflection does not explain the interaction of the IR beam with the sample because the IR beam outside the ATR crystal does not propagate as a conventional electromagnetic wave. Instead, the interaction occurs through an evanescent field, or "evanescent wave", which penetrates the sample to a depth $d_p$ expressed by the equation:

$$d_p = \frac{\lambda}{2\pi\eta_s\sqrt{\sin^2\theta-(\frac{\eta_s}{\eta_p})^2}}, \quad (6)$$

where $\lambda$ expresses the wavelength of incoming IR light. Table 1 shows that increasing the AOI decreases light penetration into the sample, resulting in a lower overall absorption. This characteristic is particularly beneficial for SEIRAS experiments, where monolayers and thin films are involved, since it reduces the interference from the absorption of the bulk solution. Considering other factors, like material hardness, spectral range, or even price (the case of a diamond), only three principal choices are available for ATR-SEIRAS experiments: ZnSe, Ge, and Si. Si is the most popular due to its cost-effectiveness and inertness. ZnSe is toxic and sensitive to pH range, which limits its application. Ge is soft and more demanding for the formation of metal coatings, which complicates its use. Therefore, the choice of crystal should consider several factors, including the nature of the sample, the experimental conditions, and the available resources.

The crystal's geometrical form is another factor that should be considered. Hemispherical crystals were initially used because they were readily available from focusing optics. However, face angle crystals (FAC) with predefined AOIs (usually 45 or 60 degrees) eventually emerged. Both crystal forms produce comparable results, but FAC is less sensitive to focus

alignment and allows for the incorporation of antireflective coatings, which can increase the total signal-to-noise (S/N) ratio by a factor of 2.[52]

To further boost the total signal, a polarizer is frequently employed due to the surface selection rule (section 1.3). However, the polarizing grating reduces total signal throughput by 50%, making it a choice in experimental settings whether it should be implemented or not, as it can also increase noise intensity by a factor of two. I. J. Burgess' group provides an excellent evaluation of these factors and minor ones not covered here.[52]

In brief, before ATR-SEIRAS experimentation, various criteria should be considered, including the selection of an ATR accessory (commercial or homemade), crystal material, form, and application of an antireflective coating, as well as AOI optimization (primarily for the highest throughput, as approximately 50% of unpolarized light is dissipated due to IRE interaction in all crystal choices).

## 1.2. Gold layer formation techniques

SEIRAS, pioneered by Osawa,[53] has become a valuable tool for the in situ analysis of supramolecular systems adsorbed on Au or Ag surfaces.[54] In recent years, the method has become technologically simpler and even commercialized.[52] Various techniques can be utilized to form thin Au layers, including electroless, vapor, electrochemical deposition[55], and hybrid ones,[56] which may benefit the higher signal-to-noise ratio, increased Au film rigidity, and allow multiple reuses of the same film. The most readily available method today remains electroless plating, a term introduced by Brenner and Riddell[57] in 1946. Electroless plating is relatively fast and requires less investment in equipment, making it affordable for starting laboratories. The method is not complicated and even time-efficient, but care should be taken because of the harmful chemicals used.[58]

**Electroless plating** defines 3 essentially different processes: autocatalytic, substrate-catalyzed, and galvanic displacement. The latter is usually utilized for SEIRAS surface preparations on Si or Ge crystals. Although the precise process behind galvanic displacement is not yet fully understood, its basic principles are generally known and may be expressed in terms of two straightforward half-cell equations:

$$\text{Anodic: } Si + 6HF \rightarrow SiF_6^{2-} + 6H^+ + 4e^-,$$

$$\text{Cathodic: } Me^{n+} + ne^- \rightarrow Me,$$

where Me is any noble metal from Table 2.[59]

Table 2. Redox potentials for all metals more noble than hydrogen (referred to the hydrogen standard electrode) (adapted from [59]).

| Element | Redox potential (V vs NHE) |
|---|---|
| **Au** | $Au^{3+}/Au$, 1.42 |
| **Pt** | $Pt^{2+}/Pt$, 1.18 |
| **Ir** | $Ir^{4+}/Ir$, 0.93 |
| **Pd** | $Pd^{2+}/Pd$, 0.83 |
| **Ru** | $Ru^{2+}/Ru$, 0.80 |
| **Ag** | $Ag^{+}/A$, 0.79 |
| **Rh** | $Rh^{3+}/Rh$, 0.76 |
| **Cu** | $Cu^{2+}/Cu$, 0.34 |
| **Ge** | $Ge^{4+}/Ge$, 0.12 |
| **Re** | $Re^{3+}/Re$, 0.30 |
| **Ni** | $Ni^{2+}/Ni$, –0.23 |

In this manner, the metal layer is formed of nanoparticles until electrons from the oxidized Si or Ge substrate can no longer penetrate it to the solution. That is not a limiting factor for SEIRAS application as the desired layer is thinner than what can be achieved.[60]

**The vacuum deposition** technique is a straightforward gold application procedure where layers of atoms are deposited on solid surfaces under a vacuum. Sputtering, laser ablation, thermal evaporation, and other processes can produce condensed particles, and different characteristic layers can be formed by manipulating particle production. This reproductive method is resistant to mishandling-related inconsistencies (human error) in metal layer preparation. Therefore, it has become one of the most popular methods for SEIRAS substrate preparation.

Nevertheless, minor issues with this approach still exist. Due to mechanical stress during cell assembly or fluid exchanges and electric potential excursions to hydrogen or oxygen evolution regions, the gold coating may not firmly adhere to the crystal surface and can peel off. Base layers such as IZO or chromium can be added to solve this issue.[56,61] Additionally, contamination with saturated hydrocarbons is often observed and is permanently trapped within a formed layer.[58] Finally, vacuum deposition equipment is expensive to purchase and maintain and is justified only for dedicated usage.

**Electrochemical deposition of the gold layer.** This method deposits gold on a crystal using a chemical reaction activated by an electrical current. This technique requires a conductive substrate to be used. Therefore, it should be noted that the electrodeposition method is not ideal and is often unsuitable for ATR-SEIRAS, as the experiments typically involve non-conductive Si

prisms due to their high chemical stability and high transparency to IR light.[62] As a result, this method is mainly reported for external reflection (Figure 9B) SEIRAS configurations.[63,64] With some exceptions that include IR transparent base layer (e. g. ITO) application to serve as a conductive substrate for electrochemical gold deposition.[56]

### 1.3. The metal surface selection rule

The metal surface selection rule (MSSR), initially described and experimentally demonstrated by H.A. Pearce and N. Sheppard, applies to metal surfaces and relies on the dipole moment and orientation of bond vibrations.[65] Specifically, molecular vibrations with a transition dipole moment (TDM) direction perpendicular to the metal surface will enhance IR spectral absorbance. At the same time, those with TDM orientations parallel to the surface will be suppressed. This effect is largely facilitated by the excellent electron conductivity of metals and the resulting interaction of electromagnetic fields at the surface (Figure 11A). As a result, a bond stretching vibration parallel to the surface will produce a dipole charge in the opposite direction to counteract the effect and cancel it out (Figure 11B). A perpendicular TDM direction creates a charge "image" of the same direction and strengthens electromagnetic interactions such as infrared light absorption.

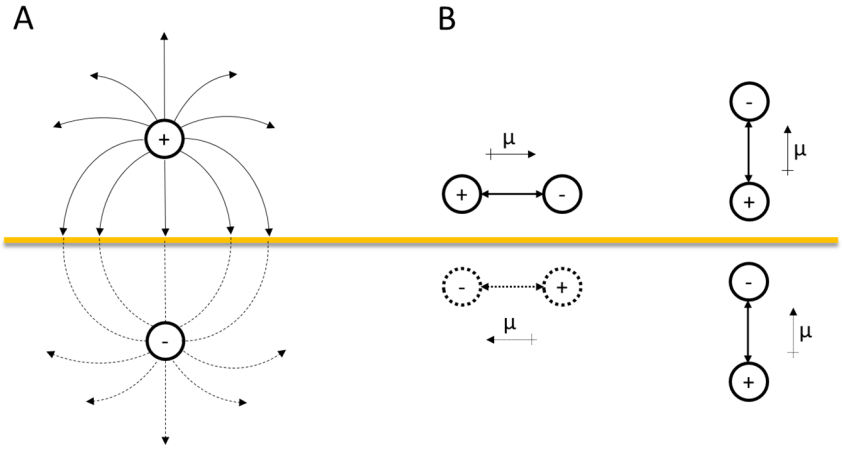


Figure 11. Simplified representation of (A) electrical field "image" of the positive charge at the metal surface; (B) dipole moment of parallel and perpendicular to the surface (yellow line) vibrations (adapted from [65]).

It is important to note that the MSSR rule only applies when the thin film thickness is smaller than the wavelength; otherwise, the IR spectrum would be affected by parallel TDM vibrations. Under these conditions, the technique is known as transflection spectroscopy.[66]

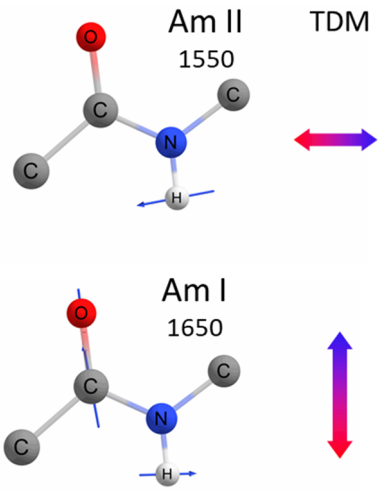


Figure 12. Directions of TDM vector in amide I and II vibrations.

The MSSR rule can be used to extract structural and orientational information on the molecules adsorbed directly on the metal surface. Experimentally, this approach involves measuring the reflected IR light's P and S polarizations, or $I_p$ and $I_s$, and presenting the results as a ratio to $\Delta R/R = (I_p–I_s)/(I_p+I_s)$. This approach is commonly used in infrared reflection absorption spectroscopy (IRRAS) and polarization modulation IRRAS techniques. Importantly, since only vibrations with TDM directions perpendicular to the surface absorb IR light, a spectrum obtained using this technique contains information on the orientation of molecules at the surface. These details can even be calculated with accurate angular values for specific molecules. A pair of mutually perpendicular molecular vibrations may serve as spectral markers sensitive to the spatial orientation of a particular group with respect to the metal surface. For example, a molecule with a peptide bond can be considered (Figure 12), where the TDM directions of amide I (Am-I) and amide II (Am-II) meet the "requirement". Any changes in the orientation of the amide group would result in alterations in Am-I and Am-II intensities. Figure 13 illustrates a simplified molecule at the surface with one vibration and its TDM orientation at an angle $\Theta$ to the surface normal.[67]

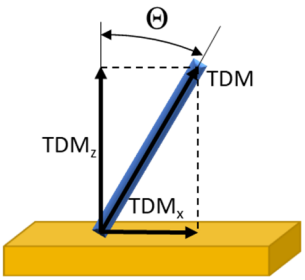


Figure 13. Orientation of the transition dipole moment (TDM) of molecular vibration with respect to a metal surface. The tilt angle ($\Theta$) of the molecule backbone compared to the surface is shown (adapted from [67]).

The orientation of every TDM can be described by two components – parallel to the surface ($TDM_x$) and perpendicular ($TDM_z$). While equation (7) can be used to calculate the molecular orientation angle if the MSSR rule does not apply to the parallel component, in practice, this is not feasible due to the suppression of $TDM_x$ by MSSR unless the absolute amplitude for |TDM| is known.

$$\tan\Theta = TDM_x/TDM_z \qquad (7)$$

For self-assembled monolayers (SAMs) on a gold surface, relation (8) can be used instead.

$$I^{SAM} \propto TDM_z \propto I^{bulk} \cos^2\Theta, \quad (8)$$

where $I^{SAM}$ is associated with the monolayer's IR band intensity, while $I^{bulk}$ is related to the spectrum of the same molecules in a solution phase. By analyzing the TDMs of two differently oriented vibrations, it is possible to estimate the tilt angle $\Theta$ using equation (9) since the intensity is proportional to the absolute values of the TDMs (Figure 14).

$$\tan^2\Theta = \frac{I_1^{bulk} I_2^{SAM}}{I_2^{bulk} I_1^{SAM}} \qquad (9)$$

Specifically, the intensity ratio of $I_1^{bulk}/I_2^{bulk}$ is equal to $(TDM_1/TDM_2)^2$ ratio, while $I_1^{SAM}/I_2^{SAM}$ is equal to $(TDM_{1z}/TDM_{2z})^2$ ratio. From experimental data, the tilt angle can be estimated by comparing the vibration intensities of the SAM and bulk samples for two distinct orientations. Figure 14 shows an example of the TDM orientations of various vibrations in a SAM-forming molecule and how the tilt angle can be determined.

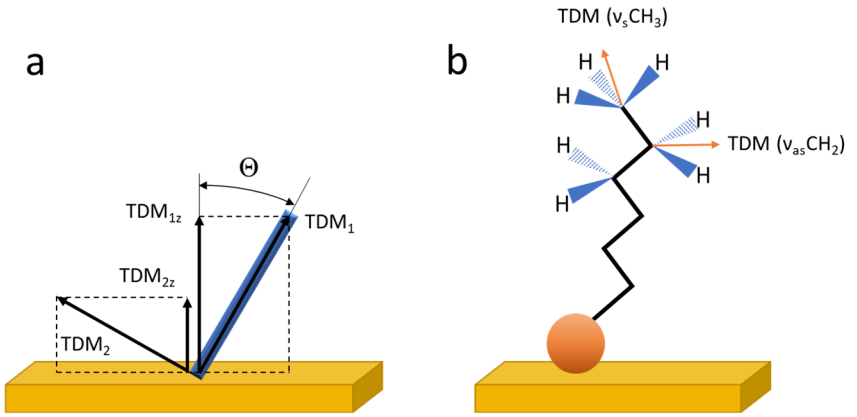


Figure 14. Orientation of the transition dipole moments (TDM) of two molecular vibrations. $\Theta$ – tilt angle of the molecule backbone compared to the surface (a). Example of various vibrations TDM orientations in SAM forming molecule (b).

## 1.4. Self-assembled monolayers

Self-assembled monolayers are molecular assemblies that spontaneously form on a surface in an organized and structured manner. SAMs have essential applications in both fundamental and commercial research, such as creating biological and electrochemical sensors,[68,69] constructing artificial lipid membranes and researching their interactions with proteins,[70] electron transfer processes at interfaces,[71] and catalysis.[72]

In technological research, SAM is used to analyze surface wetting, lubrication, friction, and depreciation[73] or to create an anticorrosive protection layer to metals[74] and antiadhesive layers for bacterial protection.[75] SAMs increase the stability of nanostructures by acting as a physical and electrostatic barrier that prevents particle aggregation. Additionally, SAM decreases the reactivity of surface atoms and thus acts as an electrical insulator layer.[76]

The application of SAMs is highly dependent on the structure and orientation of their molecules at the surface. The main factors defining a monolayer's final structure and properties are the surface morphology (macroscopic structure, defects, dislocations, etc.), chemical composition, molecular interactions with the surface, and intermolecular forces (electrostatic, hydrophobic, van der Waals, and hydrogen bonding). These parameters critically depend on the integral parts of the molecules comprising the SAM, namely the head, tail, and end group (Figure 15). Each of these groups has its function.

The head group serves as an anchor, immobilizing the molecule to the surface. It is usually either thiol, disulfide, amine, silane, phosphate,

carboxylic acid, or another group that can bind covalently to the substrate's surface.[77]

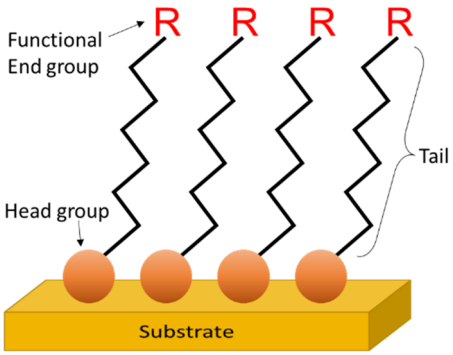


Figure 15. Schematic representation of SAM forming molecule's functional parts.

The tail group controls the thickness of the monolayer. Hydrocarbon chains in the range of ~ 2–18 carbons are usually used for this purpose and can also be aromatic or aliphatic. This domain serves as a physical barrier, increases the stability of SAM, and changes the system's electrical conductivity and optical properties. A longer chain results in stronger hydrophobic intermolecular interaction due to the thermodynamics of hydrophobic group hydration.[78] Monomer molecules with an aliphatic chain length above 10 carbon atoms form structurally ordered, more stable SAMs with smoother surface coverage and fewer defects. Additional SAM stability can be obtained by inserting chemical groups (e.g., amide) forming intermolecular hydrogen bonds.[79]

The end group of the SAM-forming molecule interacts with the solvent at the interface, participates in surface modifications, allows solution molecules to bind to the surface, and can be used for other chemical reactions.[76] For example, carboxylic acid as an end group (–COOH) may attach proteins, biomolecules, and cells, securing them to the surface. Specifically composed SAMs of lipid-like thiol molecules may act as surface anchors for a lipid bilayer to attach. Such systems mimic biological phospholipid membranes and are helpful in researching membrane-related processes and biosensor applications.[80]

## 1.5. Bilayer lipid membranes

Biological membranes are complex physical structures that form a barrier between a living cell's inner and outer compartments. They provide structural integrity, conduct the transportation of materials into and out of the cell, and

have a crucial role in energy transformation and nerve signal transmission due to their impermeability to ions.[10,81]

Lipid membranes are composed of lipids and proteins, with sugars often attached to the bilayer's outer side. Amphipathic lipid molecules in a polar solvent naturally form a self-assembling double layer where inserted proteins can perform transportation and bioanalytical functions.[81] Lipids exhibit lateral mobility and rotational freedom around their long axis within the membrane, contributing to their dynamic, fluid nature. Nonetheless, membranes have varied inner and outer layer compositions and are asymmetrical. Protein mobility within the membrane is present but substantially more restricted than lipids. Typically, the inner layer of most biological membranes is negatively charged, an essential feature for cellular functions.[82]

The most common lipids in animal cell membranes are phosphatidylcholine, sphingomyelin, phosphatidylethanolamine, phosphatidylserine, and phosphatidylglycerol.[83] Animal and plant cell lipids commonly consist of 12 to 24-carbon-atom-long fatty acids. One of the most widespread is olein ($CH_3(CH_2)_7CH{=}CH(CH_2)_7COOH$). The molecular composition of the membrane defines its fluidity, melting point, and asymmetry.[84] Cholesterol, one of the most often occurring compounds in eukaryotic membranes, can affect membrane characteristics due to its polar hydroxyl group and hydrophobic part made of four carbon rings (Figure 21). Its primary function is to change the membrane's fluidity by increasing packing between the chains of fatty acid, thus ensuring the integrity of the membrane.[85]

Living cell membranes are highly dynamic and heterogeneous, making isolating and studying specific components or processes difficult. On the other hand, synthetic membranes can be designed to have particular properties useful for research, such as high stability, permeability, or selectivity. They are relatively easy to prepare and highly adaptable to research conditions, making them an essential tool for studying membrane biology.

Many diseases have been associated with membrane protein malfunctions, which has stimulated faster research spread of biological membranes.[86] Synthetic membranes must have physical and chemical parameters similar to natural cell membranes to maintain their functionality. They should withstand fluid exchange both inside and outside and maintain electrical permeability. At the same time, they must retain fluidity and lateral molecule mobility, which is critical for keeping protein structure integrity and functionality inside the membrane. Changes in membrane fluidity can affect the activity of membrane-bound enzymes, alter membrane permeability to

different types of molecules, and influence the organization and signaling of membrane-associated proteins.

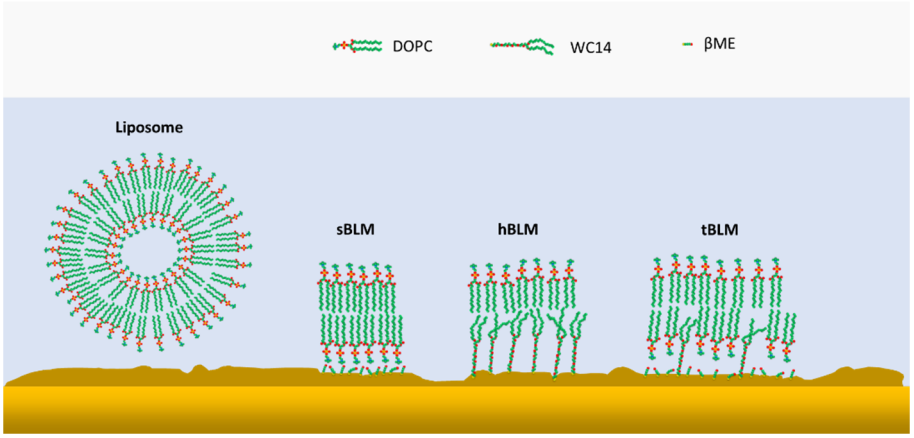


Figure 16. Types of synthetic membranes: bilayer liposome, suspended bilayer lipid membrane (sBLM), hybrid bilayer lipid membrane (hBLM), tethered bilayer lipid membrane (tBLM). The structure of monomers used in schematic representation can be found in Figure 21.

Figure 16 illustrates different types of synthetic membranes commonly used in research. Liposomes are the simplest type, consisting of one or several lipid layers forming a vesicle. Liposomes can accumulate functional membrane proteins but are not ideal for in situ monitoring or biosensor applications.[86]

Suspended bilayer lipid membranes (sBLMs) are created by merging liquid liposomes on a metal surface. sBLMs are useful for electrochemical and biosensor research. Still, they are unsuitable for studying membrane proteins, as they tend to degrade quickly due to the membrane's proximity to the metal surface.[87,88] This membrane type has many defects and is not very stable. Thus, it is hard to work with.

Hybrid bilayer lipid membranes (hBLMs) are created by merging monolayered liposomes on a SAM-covered metal surface.[89] hBLMs are stable but dense and have low fluidity, which limits their use for biological applications. However, they are useful for studying outside-layer processes, such as receptor interactions.[9,90]

The stiffness and direct interaction with the metal surface of sBLMs and hBLMs make them far from ideal for studying membrane proteins. Tethered bilayer lipid membranes (tBLMs) overcome this disadvantage by allowing the membrane to be immobilized several nanometers from the metal surface, with a water reservoir in between.[91,92] This is achieved by preparing the tBLM in several steps, which involves forming SAMs with a tethering functional end group on the metal surface, followed by creating the lipid bilayer via solvent

exchange or liposome fusion methods.[70,92] Alternatively, a less complex approach involving a 20–30 minute incubation of multilayered liposome solution on an already formed SAM has also been reported.[93]

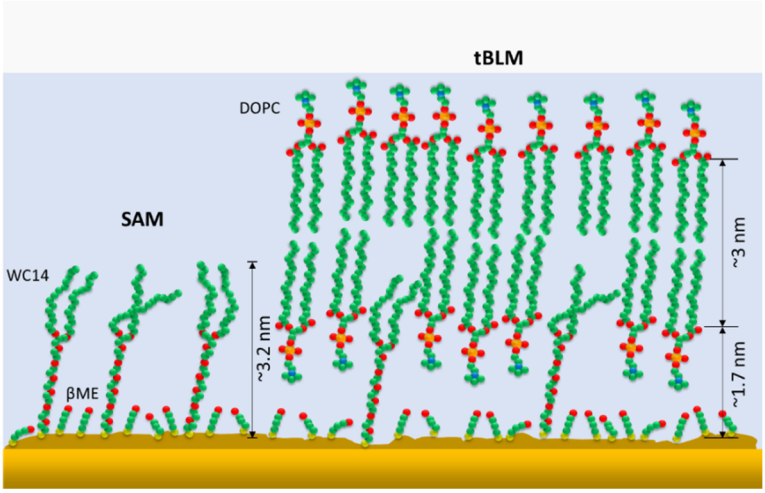


Figure 17. The synthetic tBLM-type membrane at the gold surface fixed through the SAM tether. SAM is composed of β-mercaptoethanol and WC14, and tBLM is composed of DOPC (1,2-dioleoyl-sn-glycero-3-phosphocholine) molecules. All measurements are presented according to neutron reflectometry data.[94]

The lipid bilayer is anchored to the surface at a 1.5 nm distance through the tethered monolayer, as shown in Figure 17. This enables the sustenance of a submembrane ion reservoir and reduces the metal-induced surface roughness effect on the membrane.[94] The tBLM system is often used as a matrix for studying membrane proteins, and the inner domains of integral proteins can protrude freely into the inner space without interacting with the metal surface, thereby preserving their integrity. It is a stable system suitable for studying the reconstitution of proteins into the membrane, lipid-protein interactions, receptor and enzyme functionality, and biosensor investigations.[95–97] Furthermore, the physical characteristics of the tBLM can be adjusted by manipulating the composition ratio of tethering and nontethering SAM-forming molecules or modifying the chemical structure of the end group. Tethers with unsaturated carbon chains form more fluid monolayers even at high tether concentrations in tBLM composition (~80%).[98]

To adequately mimic the processes that occur in living cell membranes, synthetic membranes should have compositions as similar to living cell membranes as possible. In this work, 1,2-dioleoyl-sn-glycero-3-phosphocholine and cholesterol were used to form membranes for SEIRAS monitoring. Additionally, deuterated analogs of 1,2-dipalmitoyl-$d_{62}$-sn-

glycero-3-phosphocholine and cholesterol-$d_7$ were used to resolve spectral band overlaps.

## 1.6. Membrane active peptides

Membrane active peptides are a type of peptide that interact with the cell membrane. They can either disrupt the membrane, pass through it, or reside at the membrane interface and fuse with it. Over the last two decades, there has been a growing interest in studying membrane active peptides, as evidenced by the increasing number of research studies conducted on them (Figure 18).[99]

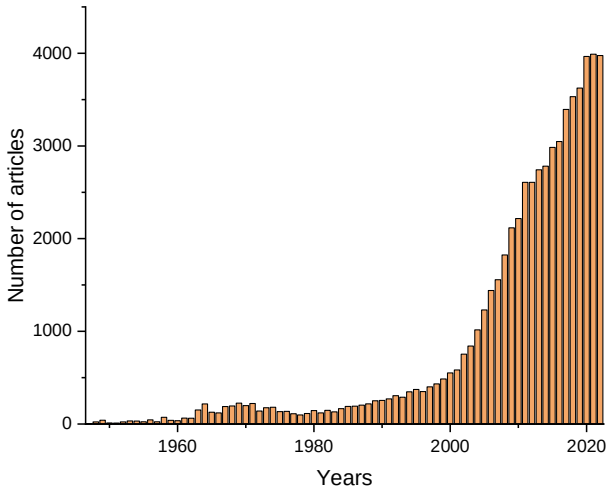


Figure 18. Combined number of publications that uses phrases “cell-penetrating peptide” and “antimicrobial peptide” (Statistical data from: https://pubmed.ncbi.nlm.nih.gov/).

The discovery of gramicidin in 1939 marked the beginning of antimicrobial peptides (AMPs).[100] Increasing microbial resistance to traditional antibiotics has led to a persistent need to discover new antimicrobial agents, generating ongoing interest in this area. A total of 3569 AMPs have been reported in the antimicrobial peptide database (APD; https://aps.unmc.edu), updated on November 17th, 2023. Classifying natural AMPs is a challenging task due to their diversity.[101] Peptide database shows 7 groups of classification criteria: based on (1) the biosynthetic machines, (2) biological source, (3) functions, (4) peptide properties, (5) covalent bonding pattern, (6) structural characteristics, and (7) molecular targets.

Different types of AMPs share specific characteristics: their number of amino acid residues is usually less than 60, and they are mostly positively charged or cationic. AMPs are naturally found in six life kingdoms, namely

bacteria, archaea, protists, fungi, plants, and animals, where they serve as a vital component of the host defense system.[99,102] As per statistics available on the ADP database, the activity of AMPs can be classified into 18 different categories, which include antibacterial,[103] antiviral,[104] antifungal,[105] antiparasitic,[106] anti-human immunodeficiency virus, and anti-tumor peptides.[107]

AMPs present a wide range of secondary structures, as demonstrated by various peptide structural studies conducted by Fjell and Hiss.[108] These peptides can be divided into four categories based on their structures, namely linear extension, α-helical, β-sheet, and mixed peptides that exhibit both α-helical and β-sheet structural features (Figure 19).[102] Moreover, the literature reports progressively cyclic peptides and more complex AMPs with diverse topologies.[109]

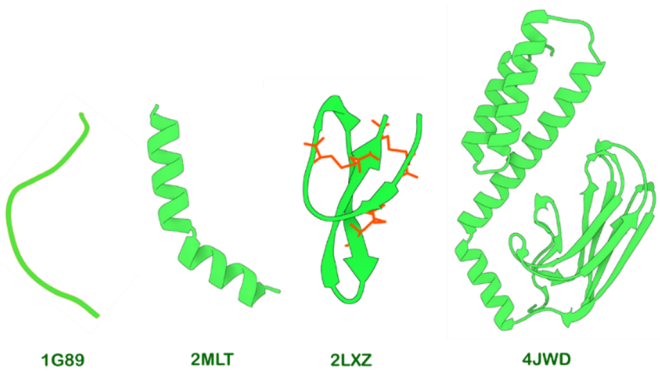


Figure 19. Examples of various secondary structure AMPs: indolicidin (1G89) has a linear extended structure, melittin (2MLT) is composed entirely of α-helices, defensin (2LXZ) is an all β-sheet structure, and bactenecin (4JWD) is a mixed α-helix and β-sheet structure. The RCSB protein data bank (available at https://www.rcsb.org/) was used to prepare the 3D images.

AMPs typically contact microbial membranes through nonspecific electrostatic and hydrophobic interactions. The mechanism of action of AMPs can be categorized into two models: membrane targeting and non-membrane targeting.[102] Membrane-targeting AMPs interact with the membrane, while non-membrane-targeting AMPs inhibit vital processes like nucleic acid[110] and protein[111] synthesis, protein catalytical activity,[112] or cell division[113] within the host's cytoplasm.

The mechanisms by which AMPs target the membrane can be explained using four main models: toroidal and barrel-stave pore-forming models, carpet model, and aggregate model (Figure 20).[102,114]

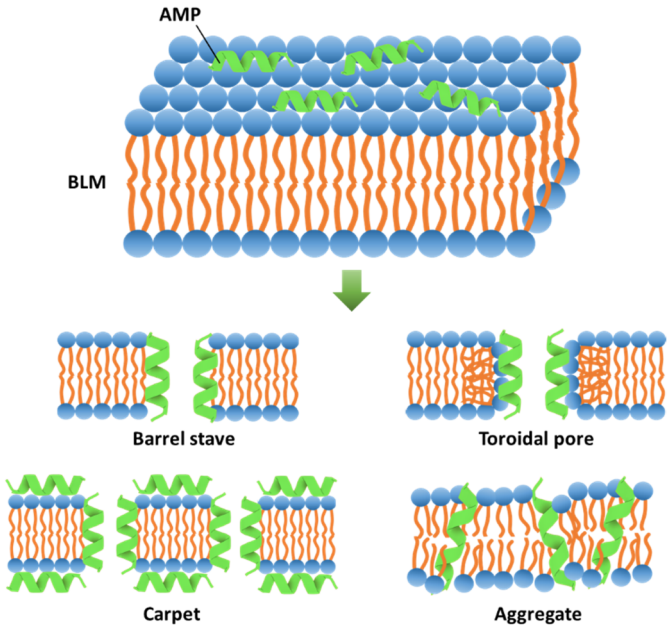


Figure 20. Membrane action models of AMPs (adapted from [114]).

According to the toroidal pore model, peptides have the ability to disrupt the normal separation of polar and nonpolar regions of the membrane.[115] This model suggests that AMPs, when embedded in the cell membrane, accumulate and subsequently bend to create a ring-shaped hole with a diameter of approximately 2 nanometers. It is worth mentioning that in this toroidal structure, the peptides can either be perpendicular or tilted with respect to the plane of the membrane.[116] These pores are known to be transient, which allows the peptide to enter the cytoplasm and target intracellular components.[117] Additionally, the toroidal pores exhibit ion selectivity and discrete sizes.[118] Some examples of toroidal pore-forming peptides include melittin and magainin.[119,120]

The barrel stave pores forming peptides aggregate with each other and create multimers that penetrate the cell membrane by forming cytoplasmic outflow channels. These peptides are oriented perpendicularly to the membrane plane to generate a relatively firm cylindrical barrel. According to this model, AMPs initially bind to the membrane surface as monomers, followed by oligomerization and pore formation. The minimum length of the structures should span the lipid bilayer, and they could be either α-helical or β-sheet. Alamethicin[120] and pardaxin[121] are known to form barrel stave pores.

In a carpet model, peptides do not form pores. Instead, they lie parallel to the membrane surface, with their hydrophilic part facing the solution and

hydrophobic part facing the phospholipid bilayer. Membrane permeabilization occurs through nonspecific interaction,[122] destabilizes the membrane structure, and leads to disintegration.[123,124] This model is utilized by antimicrobial peptides like cathelicidin LL-37[125] and cecropin c1[126] to perform their functions.

AMPs in the aggregate model bind to the anionic cytoplasmic membrane, resulting in the formation of a peptide-lipid complex micelle.[127] Unlike the carpet model, the channels formed by AMPs, lipids, and water allow ions and intracellular contents to leak, ultimately leading to cell death.

While research on AMPs is continuously progressing, and vast amounts of data on AMPs have been stored in AMP databases, the mechanism of action of these peptides remains incompletely understood. Therefore, further elucidation of the mechanism of action of AMPs is crucial in understanding the specific conditions in which these peptides function.[102]

# 2. MATERIALS AND METHODS

## 2.1 Materials

| | |
|---|---|
| ***Deionized water*** | Milli-Q plus, USA, 18.2 MΩ·cm; |
| ***Ethanol*** | Vilniaus degtine, Lithuania, 96%; |
| ***DOPC****, (1,2-dioleoyl-sn-glycero-3-phosphocholine)* | Avanti Polar Lipids, USA; |
| ***Cholesterol*** | Avanti Polar Lipids, USA; |
| ***WC14,*** *(20-tetradecyloxy-3,6,9,12,15,18,22-heptaoxatricontane-1-thiol)* | The compound was synthesized by David J. Vanderah at NIST Chemical Science and Technology Laboratory, Gaithersburg, Maryland, USA;[70] |
| ***βME,*** *(β-mercaptoethanol)* | 99%, Sigma-Aldrich (St. Louis, MO, USA) |
| ***NaCl,*** | 99.5% Fluka, Switzerland; |
| $NaH_2PO_4 \cdot H_2O$ | 98% Sigma-Aldrich (St. Louis, MO, USA), ACS grade |
| $Na_2S_2O_3 \cdot 5H_2O$ | 99.5% Sigma-Aldrich (St. Louis, MO, USA), ACS grade |
| $NaAuCl_4 \cdot 2H_2O$ | 99%, Sigma-Aldrich (St. Louis, MO, USA) |
| $Na_2SO_4$ | 99% Sigma-Aldrich (St. Louis, MO, USA), ACS grade |
| $Na_2SO_3$ | 98%, Fluka (Buchs, Switzerland) |
| $H_2SO_4$ | 98% Concentrated, Roth (Karlsruhe, Germany) |
| $HNO_3$ | 65% Fluka (Buchs, Switzerland) |
| ***HCl*** | 30% Roth (Karlsruhe, Germany) |
| $C_3H_6O$ ***(Acetone)*** | 99.9% Roth (Karlsruhe, Germany) |
| $NaCH_3COOH$ | 98.5% Fluka (Buchs, Switzerland) |

| | |
|---|---|
| ***$NH_4Cl$*** | 99.5% Sigma-Aldrich (St. Louis, MO, USA) |
| ***$NH_4F$*** | 98% Sigma-Aldrich (St. Louis, MO, USA) |
| ***HF*** | 48% Sigma-Aldrich (St. Louis, MO, USA) |
| ***$CD_3CD_2OD$ (Ethanol-d6)*** | 99 atom% D, Roth (Karlsruhe, Germany) |
| ***$CD_3OD$ (Methanol-d4)*** | 99 atom% D, Roth (Karlsruhe, Germany) |
| ***$D_2O$*** | 99 atom% D, Roth (Karlsruhe, Germany) |
| ***3, 1 and 0.25 µm diamond particle suspension in water*** | QATM (Mammelzen, Germany) |
| ***N-(2-(1H-imidazol-4-yl)ethyl)-6-mercaptohexanamide (IMHA) and 6-mercapto-N-methylhexanamide (fragment molecule, Frag)*** | Synthesized in-house.[128] |

Chemical compounds shown in Figure 21 were used in formation of various monolayers and membranes. Deuterium-substituted compounds were used for clarification of band assignments.

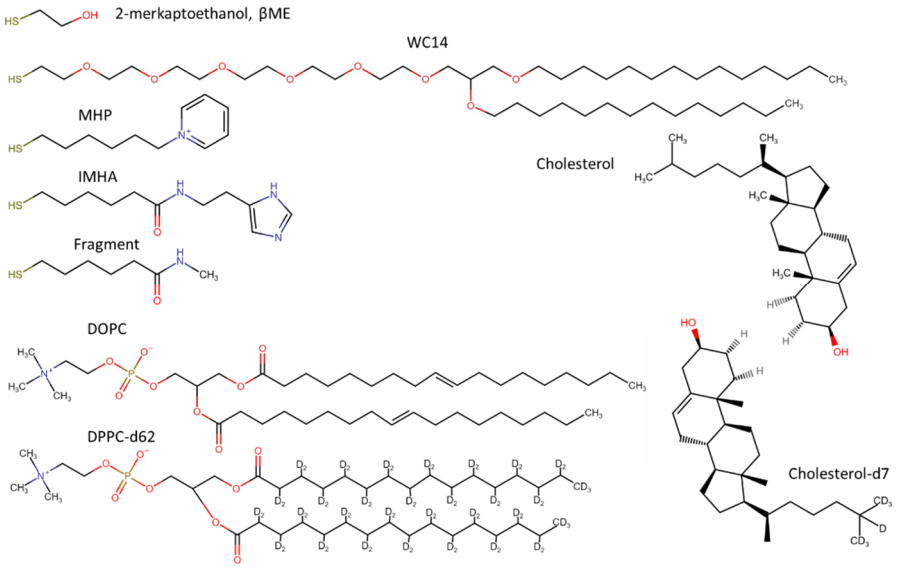


Figure 21. Chemical structure of compounds used in thesis.

## 2.2 Methods

### 2.2.1 Isotopic substitution

The exchange of stable isotopes in the molecules enables the identification of vibrational bands and helps to resolve any overlapping with other bands. The vibration frequency is directly proportional to the restoring force constant ($K$) and inversely proportional to the reduced mass ($\mu$) of the atoms forming the bond, as shown in equation 3. The reduced mass is calculated as $\frac{1}{\mu} = \frac{1}{m_1} + \frac{1}{m_2}$, where $m_1$ and $m_2$ represent the masses of both nuclei. Since the bonding force, $K$, depends only on the constituent charge of the nucleus and electrons, the vibrational frequency ($\omega_e$) is affected by the difference in mass. As a result, exchanging a lighter isotope for a heavier one „shifts“ the frequency to a lower value.[129]

Our experiments used initially deuterated compounds or solvents such as $D_2O$ and $CD_3–CD_2–OD$ to resolve overlapping bands. The exchange between solvent deuterium and hydrogens attached to the target molecule's N, O, and S atoms occurs instantly due to their high mobility.[130] The symmetric and asymmetric C–H area investigation has greatly benefited from this property.

### 2.2.2 FTIR spectroscopy systems

**ATR-FTIR** spectra were obtained using an Alpha spectrometer (Bruker, Germany) equipped with a diamond ATR accessory and a DTGS (*deuterated triglycine sulfate*) detector. The spectrometer was operated at a scan speed of 7.5 kHz, and the spectral resolution was set to 4 $cm^{-1}$. For both sample and background channels, 200 scans were co-added unless stated otherwise.

**ATR-SEIRAS** measurements were carried out using a Vertex 80v spectrometer (Bruker, Germany) equipped with a liquid nitrogen-cooled narrow band MCT (*mercury cadmium telluride*) detector. The spectrometer operated at a scanner speed of 40 kHz and a resolution of 4 $cm^{-1}$ with a 2 mm aperture. Sample and background scans were collected with 50 and 100 iterations, respectively, unless otherwise stated. The experiments used a freshly prepared nitrogen-blow-dried Au/Si crystal assembled into a VeeMax III variable-angle accessory with a Jackfish cell J1F (Pike Technologies, USA, Figure 22). The ATR unit was set to an angle of 63 degrees. After assembly, the spectrometer was purged with dry air overnight to remove any residual water vapor from the spectrometer chambers.

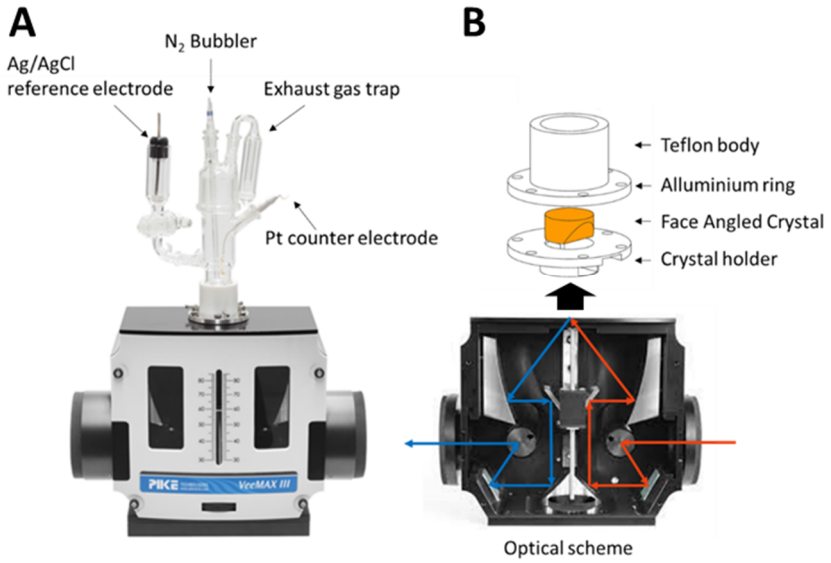


Figure 22. (A) VeeMax® variable angle ATR cell (Pike Technologies) with electrochemical cell (Jackfish SEC Manufacturing). (B) Schematics of the optical beam path and main cell body construct.

### 2.2.3 Electrochemical measurements

Electrochemical measurements were carried out using a three-electrode system comprising a gold layer as the working electrode, a reference Ag/AgCl electrode, and a counter Pt electrode. Before each SEIRAS experiment, the gold layer of the Si crystal was electropolished and activated in a pH 5.8 sodium acetate solution (0.1 M) using cyclic voltammetry (CV) scans controlled by a PGSTAT101 potentiostat (Methrom, USA).

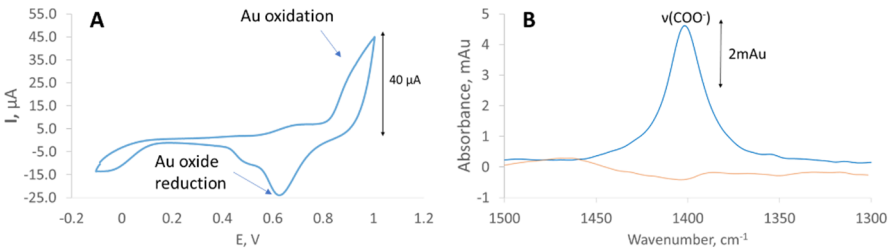


Figure 23. (A) CV performed at 20 mV/s in 5.8 pH 0.1 M acetate. (B) ν(COO⁻) mode measured at 0.6 V potential at the Au layer surface acetate solution (blue) and spectra after surface washed with deionized water (orange) (–0.1 V potential in acetate was used as a reference).

The cell was filled with sodium acetate solution (0.1 M) and purged with nitrogen for 30 minutes before the CV scans, which were performed starting in the range of ±200 mV from the open circuit potential (OCP) at a scan rate of 20 mV/s. A detailed gold layer activation procedure can be found described in section 2.2.7. A typical CV obtained at the final cycle and $\nu(COO^-)$ peak is shown in Figure 23.

### 2.2.4 Scanning electron microscopy

SEM images were acquired using a JSM-IT200 InTouchScopeTM (Jeol, Japan) microscope operating at 20–25 kV accelerating voltage, as indicated in the figures, with a secondary electron detector. The samples were washed with deionized water and dried under a nitrogen gas flow before being glued to the stage with an adhesive carbon sticker to improve stability.

### 2.2.5 Density functional theory modeling

Theoretical modeling was performed using Gaussian 09W.[131] Geometry optimization, and frequency calculations were completed using the B3LYP functional and the 6-311++G(2d,p) basis set. The calculated frequencies and intensities were scaled according to the procedure described elsewhere.[132] No imaginary wavenumbers were obtained in the calculated spectra.

### 2.2.6 Gold layer formation

The gold layer was formed using an electroless deposition method called the chemical deposition method. This method basis has been modified from the original M. Osawa published method,[58]. The protocol used for gold preparation in this work was adapted considering conditions mentioned in several literature sources.[52,55,58,133–137] The following steps were taken to prepare the crystal surface.

**Crystal surface preparation.** First, the reflecting plane of the Si crystal was polished by hand using a polishing pad (QATM, Germany) and water-based diamond suspensions with decreasing particle sizes, starting with 3 μm (5 min), then 1 μm (5 min), and 0.25 μm (20 min). Polishing was performed by shaping the "∞" symbol and turning the crystal 90 degrees every 15 seconds with thorough water rinsing between each polishing step. Then, the mirror-polished Si crystal was ultrasonicated with acetone and water twice for 10 minutes and dried under a nitrogen stream. The prism sides were protected with 0.1 mm Teflon ribbon to prevent mirror antireflective coatings from damage.

**One-step electroless Au plating** was performed by preparing a fresh Au plating mixture in a Teflon container and stirring it continuously. Equal volumes of (1) salt solution (0.15 M $Na_2SO_3$, 0.05 M $Na_2S_2O_3$, 0.05 M $NH_4Cl$), (2) $NH_4F$ (20 wt%), (3) HF (2 wt%), and (4) $NaAuCl_4$ (0.03 M) were mixed to at least 2 mL in total. The (4) solution was freshly prepared for every plating series performed. To hydrogenate the Si surface, the polished crystal was incubated with 1 mL HF (2 wt%) for 4 min, after which it was removed, and 1 mL Au plating mixture was added for another 3–4 min in room temperature conditions. The crystal surface attained a bright yellow color during Au plating, and the reaction was stopped by transferring the crystal directly into a water bath for 5–10 minutes intervals. SEM images in Figure 24A show the formation of even and approximately 50 nm diameter nanostructures.

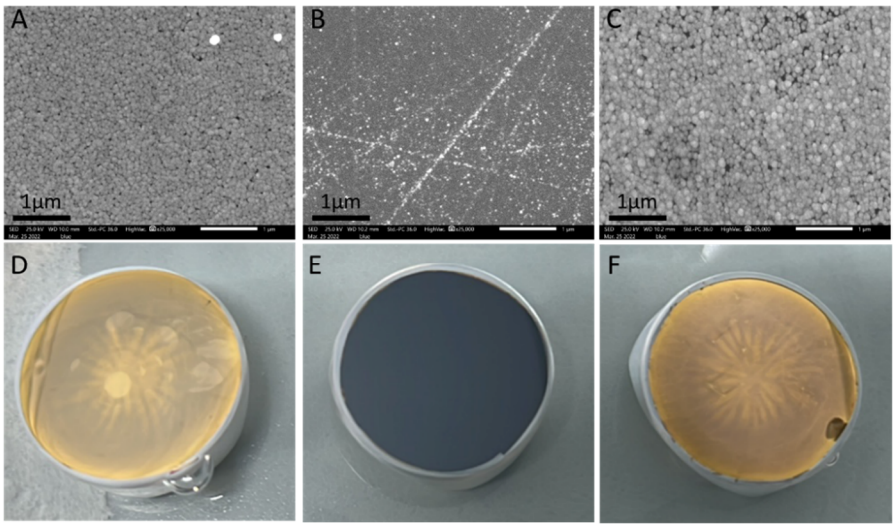


Figure 24. SEM images of silicon crystal surface (A–C) after first electroless deposition of gold layer (A), gold removal with *aqua regia* solution (B), and after second deposition of gold layer (C). Respective photo images of Si crystals used for SEM analysis (D–E).

**Two-step electroless Au platting** was performed to improve the stability of the gold layer, according to Yaguchi and Uchida's published data.[136] After the first gold layer formed, the surface was washed with deionized water and dried under nitrogen flow. A few drops (~ 0.6 to 0.8 ml) of concentrated *aqua regia* acid solution (4:1 $HCl/HNO_3$) were added to the surface to dissolve the formed gold layer, which was washed away immediately with deionized water, followed by nitrogen drying. The revealed silicon surface became grey and opaque (Figure 24E). The second deposition of gold was performed by adding an Au plating mixture for the same period as used in the first Au layer

formation. The plating was stopped by placing the Si crystal in a water bath for 5 min, and then the blow-dried crystal was mounted into the SEIRAS accessory. Each crystal preparation took place just before the experiment to avoid prolonged storage as they degrade with time.

The removal of the first gold layer left some firmly attached remnant gold nanoparticles (Figure 24B) that acted as crystallization centers, which initiated the formation of a second layer and greatly improved gold layer attachment to silicon and even increased formed gold platforms in size (Figure 24C), which are beneficial for SEIRAS signal. This method increases the success rate of gold preparation for SEIRAS experiments. It improves the reproducibility of the signal, with less variation in signal strength compared to the single-layer formation technique.

### 2.2.7 Gold layer activation.

Before using the gold surface for experiments, it was cleaned and activated using electrochemical polishing, a process known to enhance the SEIRAS signal. The process involves (i) removing surface contamination to allow for greater analyte adsorption and (ii) introducing additional roughness by producing various steps, ad-atoms, and other defects. Electrochemical polishing restructures the texture of the gold islands, which is essential for SEIRAS signal enhancement.[55,138]

Cyclic voltamperometry (CV) was performed using PGSTAT101 potentiostat in 0.1 M pH 5.8 sodium acetate solution. The gold layer was used as a working electrode with an Ag/AgCl reference electrode and platinum counter electrode (Figure 22A). A cell containing a 0.1 M sodium acetate solution was purged with nitrogen for 30 minutes before performing CV. The process began in the range of ±200 mV from the open circuit potential (OCP) registered, with a speed of 20 mV/s. The potential range was extended by 100 mV in the anodic direction every three complete cycles (Table 3). For cycles 1 to 3, a cathodic limit was the OCP value minus 200 mV and an anodic limit was OCP value plus 200 mV. For cycles 4 to 6, the cathodic limit was –100 mV, and the anodic limit was OCP + 300 mV, and for cycles 7 to 9, the cathodic limit was –100 mV and the anodic limit was OCP + 400 mV. The process was continued until the desired limit was reached, and for subsequent cycles, the cathodic limit remained constant at –100 mV, while the anodic limit increased by 100 mV with each cycle.

SEIRAS measurements were performed at the designated CV steps to verify surface cleaning. Reference and sample spectra were collected at –100 mV and 600 mV, respectively, to locate the marker band of the gold surface-

adsorbed acetate. With each CV treatment step, there was an increase in the $\nu(COO^-)$ band intensity at 1400 $cm^{-1}$ observed (Figure 23B). The procedure was stopped when the gold oxidation became visible since lengthier CV treatment raises the danger of the gold layer delamination. A few milli-absorptions intensity of the $\nu(COO^-)$ mode was sought to be sufficient for the experiments.

Table 3. Cathodic and anodic limits for SEIRAS gold layer activation.

| CV Cycle | Cathodic limit | Anodic limit |
|---|---|---|
| **1, 2, 3** | OCP – 200 mV | OCP + 200 mV |
| **4, 5, 6** | –100 mV | OCP + 300 mV |
| **7, 8, 9** | –100 mV | OCP + 400 mV |
| **….** | … | … |
| **n, n+1, n+2, …** | –100 mV | 1000 mV |

### 2.2.8 SAM and BLM formation

To form self-assembled monolayers, ethanol dissolved thiol molecules (Figure 21) were added on a freshly prepared gold layer. Several different preparations were used in this work: (i) WC14, (ii) WC14/βME 3:7, (iii) WC14/βME/MHP 3:3:4, (iv) IMHA, (v) IMHA/Frag 1:1, (vi) IMHA/Frag 1:5, and (vii) Frag. Before the formation of SAM, the Au surface was washed several times with water, and the reference spectrum was collected for future use in order to subtract water spectral bands from the sample spectrum. The cell was then rinsed with ethanol, and the SAM incubation solution (about 0.2 mL) was injected to a total concentration of 0.5 mM and incubated for more than 1 hour. The surface was washed with pure ethanol to ensure the SEIRAS signal originates solely from the surface-attached monolayer.

**Membrane formation:**

The formation of lipid bilayer membranes involves several processes, including:

- deposition of membrane-anchoring SAM;
- preparation of multilamellar vesicles (MLVs);
- fusion of MLVs on a SAM surface to form a bilayer membrane (BLM).

SAM suitable for a tBLM formation was created by immersing a freshly gold-coated substrate in a 0.5 mM ethanol solution containing compounds of WC14 and β-mercaptoethanol (βME) with a respective molar ratio of 3:7. For

the creation of the hBLM, solely WC14 molecule was utilized. The mixed SAM-forming molecules were incubated on the gold surface for an hour, after which they were carefully washed with ethanol and phosphate buffer (0.1 M NaCl, 0.01 M $NaH_2PO_4$, pH 4.4).

To prepare multilamellar vesicles, a constant molar ratio of 4:6 was used for cholesterol and 1,2-dioleoyl-sn-glycero-3-phosphocholine (DOPC), respectively. The lipids were then dissolved in 99% chloroform to a final concentration of 10 mM, and the chloroform was evaporated with nitrogen flow to create a thin lipid film. The film was then resuspended into a homogenous and milky opaque solution by injecting phosphate buffer solution into the vial and slowly aspirating-dispensed with an automated pipette (~1 cycle/s).[93]

To form BLMs, a solution of multilamellar vesicles was added to freshly formed self-assembled monolayer samples and incubated for an hour at room temperature. The reaction cell was covered to avoid evaporation during all procedural steps. The phosphate buffer solution was used to cleanse excessive vesicles and cleanse the lipid bilayer membrane prior to the melittin insertion experiments.

### 2.2.9 Formation of tBLM for SEIRAS pH measurements

SAM was formed from WC14 at a 35:65 mol% to βME ratio. After 1 hour of incubation, SAM was washed with ethanol and phosphate buffer solution (0.1 M NaCl, 0.01 M $NaH_2PO_4$, pH 4.5). Then, tBLM was formed from DOPC/Chol 70:30 ratio compositions. The pH shift experiment used 0.05 M phosphate solutions with 0.1 M $Na_2SO_4$ and pH values of 4.5 and 7.3.

### 2.2.10 Anomalies

The adsorption of SAM molecules on the surface results in emerged SAM-related spectral modes that are positive in intensity. At the same time, solvent molecules become withdrawn from the surface as they vacate the available surface area for the thiols that form strong covalent bonds with Au. Therefore, the negative spectral modes appear. Sometimes, a thin gold layer produces spectral anomalies, which occur as inverted and, in some cases, shifted peaks. This effect is known and has been sensitively mentioned in several publications.[47,63,139–143] However, it is not well understood. In this work, the same effect was noticed several times under similar conditions. An example of the ordinary and inverted spectrum shown in Figure 25 is related to two distinctively different Au layer thicknesses, evaluated by Au layer electric

resistance (Ω) measurements conducted between two electrode pins touching the Au layer. A higher resistance indicates a thinner gold layer and vice versa. Resistance differs in order of 4 times in the presented example. The SAM peaks on the thinner gold layer appear as a negative absorption, while ethanol is positive. The fact that the effect was observed many times on similar experimental and hardware conditions suggests that it is a natural phenomenon and not a computational artifact. While increasing the thickness of the gold layer can avoid this effect, it is still intriguing enough to give a brief mention in this work.

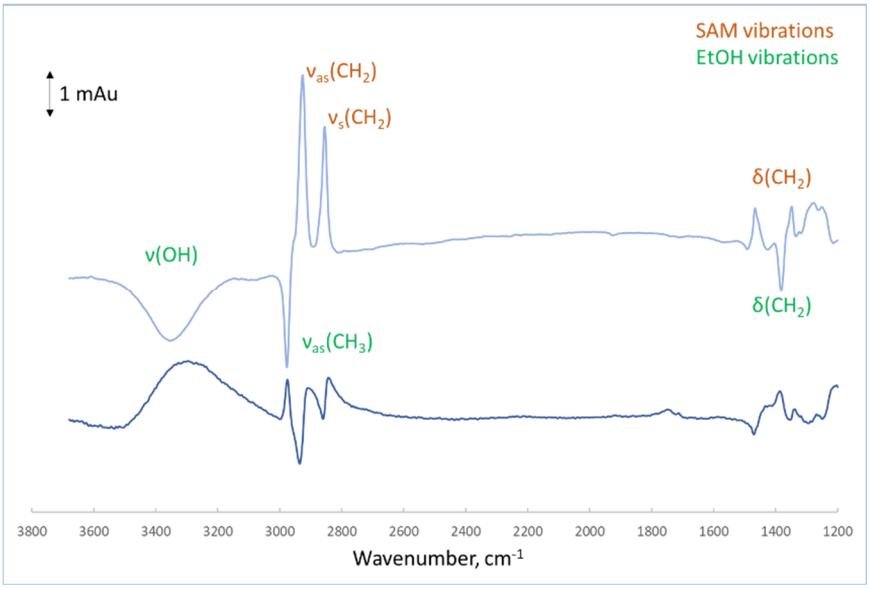


Figure 25. SEIRAS spectra of SAM formed from WC14 and βME with a ratio of 3:7, respectively, on a thinner (dark blue) and thicker (light blue) gold surface in ethanol solution. Pure ethanol was used as a reference spectrum. The light blue spectrum shifted upwards for clarity.

### 2.2.11 Data handling

All raw spectral data were processed using OPUS 7.5 software (Bruker, Germany). The processed spectra were then exported into data table format for further analysis and visualization using Origin 9.5 (OriginLab, USA) or Excel 2019 (Microsoft Corporation, USA). GRAMS/AI 8.0 software (Thermo Scientific Inc., USA) was used to fit the spectral bands.

# 3. ELECTROCHEMICAL SEIRAS ANALYSIS OF IMIDAZOLE RING FUNCTIONALIZED SELF-ASSEMBLED MONOLAYERS

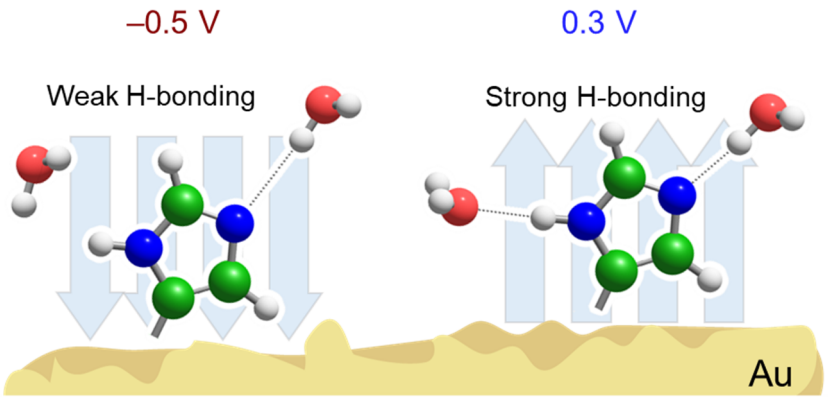

## 3.1. Histidine's importance and properties

Histidine is an essential amino acid that stands out due to its unique properties among all amino acids. Its pKa value of 5.9 is the closest to physiological pH, and its side chain imidazole (Im) can participate in a wide variety of interactions, crucial for protein architecture and catalytic activity.[7,144] Im can participate in hydrogen bond interactions, function as an aromatic system, and utilize the nitrogen's lone electron pair to coordinate metal (II) cations.[8] The pKa value of Im is 6.9, with only one nitrogen protonated under physiological conditions, resulting in two potential neutral tautomeric forms (Figure 26). Tautomer-I (T-I) is protonated at the N1 atom (N1-H, N3), while Tautomer-II (T-II) is protonated at the N3 atom (N1, N3–H). The T-I form predominates in neutral pH solutions at room temperature due to a slight energy advantage.[145] The tautomeric equilibrium can be affected by temperature, intermolecular interactions, chemical Im group environment, and other environmental factors. For example, chemisorption on a metal surface was found to cause a distinct T-I to T-II shift in a molecule containing imidazole.[146]

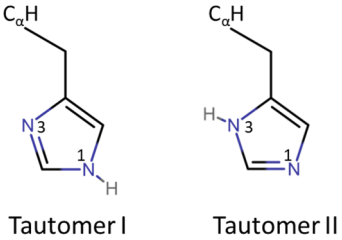


Figure 26. Structure of histidine's side chain tautomer I and II at physiological pH conditions.

Hydrogen bonding is one of the most critical interactions that control protein folding, molecular conformation, and packing. The Im, in its neutral state, can act as both a hydrogen acceptor and donor. However, studying these hydrogen interactions at electrified interfaces is challenging due to the lack of suitable experimental methods. Vibrational spectroscopy can probe the physical surroundings of the investigated molecules as well as intermolecular interactions and electric field-induced molecular changes. Raman spectroscopy, for instance, offers specific information on Im structure and interactions with divalent metal cations in natural biomolecules and model compounds.[145–154]

In contrast, Fourier-transform infrared absorption spectroscopy (FTIR) has a much larger absorption cross-section, making it particularly beneficial

for dynamic studies and cases with a limited number of molecules under investigation.

## 3.2. Objectives and experimental approach

This study employed the electrochemical-SEIRAS approach to gain a deeper understanding of the Im interactions with the local surroundings at the organic layer-water interface on electrically polarized electrodes. For this purpose, N-(2-(1H-imidazol-4-yl)ethyl)-6-mercaptohexanamide (IMHA) molecule was synthesized in our lab, and this compound was used to form a self-assembling monolayers on the surface of gold (Figure 21). Focusing on the alterations in the functional Im group, the SEIRAS approach provided insights into the adsorption and reorientation dynamics of the SAM molecules. The investigation of their changes at the electrified interface was conducted, along with the identification of spectroscopic markers for hydrogen bond interactions at the Im group. This research contributes to our understanding of histidine interfacial behavior, which is crucial for the structure and function of proteins and may benefit surface chemistry applications.

## 3.3. Results and discussion

### 3.3.1. The assignment of spectral bands for IMHA and fragment molecules

The IMHA molecule consists of four structural components: (1) the thiol group (–SH), which interacts with the gold surface, (2) the alkane chain (–$CH_2$–)$_5$ spacer, (3) an amide group that enhances SAM stability,[155] and (4) a functional Im that acts as the terminal end group. Additionally, a surface backfiller (fragment molecule, Frag) was added to the monolayers to adjust the concentration of imidazole rings at the interface. Except for the Im, which is replaced by a methyl group, its chemical structure is similar to that of IMHA (Figure 21). ATR-FTIR spectra of IMHA, Frag, and recrystallized IMHA molecules from ethanol-$d_6$ (IMHA-d) are displayed in Figure 27, and their assignments are presented in Table 4. All assignments are based on the literature and our density functional theory calculations.[146,148,149,154,156–160]

The two highest intensity bands in the ATR-FTIR spectra of solid IMHA are attributed to the Amide-I (Am-I) vibration at 1635 $cm^{-1}$, mainly involving C=O coupled with out-of-phase C–N stretching and C–C–N bending motion, and the Amide-II (Am-II) mode at 1573 $cm^{-1}$, associated with NH bending combined with C–N stretching.[18,130] The mobile N-hydrogens readily exchange with D from the solvent, such as ethanol-$d_6$, which lowers the vibrational frequencies of the Am-I and Am-II modes to 1622 $cm^{-1}$ and 1467

$cm^{-1}$, respectively. Furthermore, due to deuterium substitution, ND bending and C–N stretching of Am-II are no longer coupled, which effectively changes the direction of the TDM vector.[161]

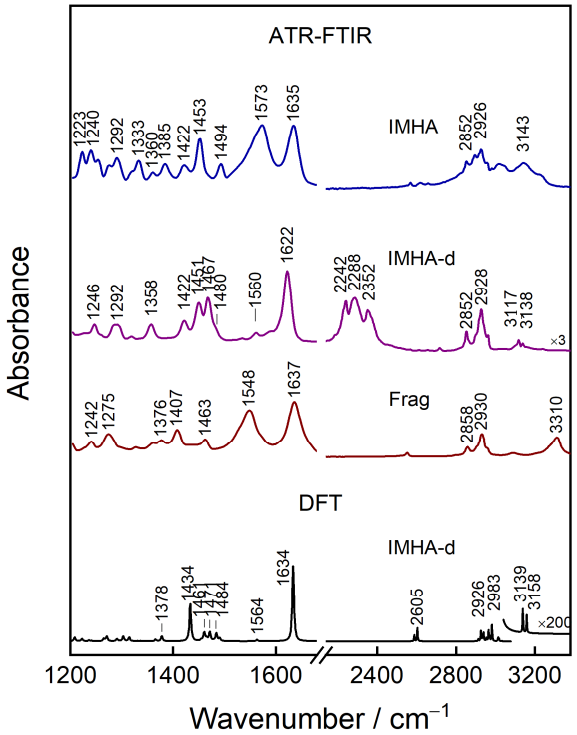


Figure 27. ATR-FTIR and DFT spectra of bulk IMHA and fragment molecules. IMHA-d refers to S–D and N–D substituted IMHA molecules.

The aliphatic chains of IMHA and Frag give rise to modes around 2852 $cm^{-1}$ and 2926 $cm^{-1}$, attributed to symmetric and asymmetric methylene stretching motion and scissoring deformation of $CH_2$ at 1451–1463 $cm^{-1}$. The frequency at 1407 $cm^{-1}$ is assigned to the symmetric deformation of the terminal methyl group $\delta_s(CH_3)$ in the fragment molecule, with its vibrational energy being affected by the induction effect from the neighboring nitrogen of the amide group.[162] Upon H/D exchange, the complex N–H stretching pattern above 3000 $cm^{-1}$ shifts to the 2240–2350 $cm^{-1}$ region, where two distinct bands, Amide-A' and Amide-B', can be observed at 2352 $cm^{-1}$ and 2288 $cm^{-1}$.[163,164] The third band ascribed to the imidazole ring is attributed to the 2242 $cm^{-1}$ mode.

Some of Im's features had been masked by strong IR absorption bands in standard solutions, and only the H/D exchange revealed it. Modes in the IMHA-d spectrum are attributed to the ν(C5–H) and ν(C2–H) at 3138 $cm^{-1}$ and 3117 $cm^{-1}$, respectively; 2242 $cm^{-1}$ to the $N_1$–D stretching and 1560 $cm^{-1}$

to the ν(C4=C5). The mode at 1494 $cm^{-1}$ in the IMHA spectrum can be identified as a C2–N3 stretch combined with in-plane C2H bending of the Im, appearing in the IMHA-d spectrum as a 1480 $cm^{-1}$ frequency shoulder (1484 $cm^{-1}$ in DFT for IMHA).[158,160]

Table 4. ATR-FTIR, SEIRAS, and DFT Vibrational Modes and Assignments of IMHA and Deuterium Substituted IMHA

| ATR-FTIR | | SEIRAS | | DFT | Assignment |
|---|---|---|---|---|---|
| IMHA | IMHA-d | IMHA | IMHA-d | IMHA-d (T-I) | |
| Im related modes | | | | | |
| | 3138 vw | | 3152 m | 3158 vw | ν(C5–H) |
| | 3117 vw | | 3115 m | 3139 vw | ν(C2–H) |
| | 1560 vw | | | 1564 vw | ν(C4=C5) |
| 1494 w | 1480 sh | 1493 vw | | 1484 w | ν(C2–N3) + β(C2H) + ν(C2–N1) + ν(C5–N1) |
| Amide bond related modes | | | | | |
| 1635 s | 1622 s | 1645 m | | 1634 s | Am-I or Am-I', ν(C=O) |
| 1573 s | 1467 m | 1556 s | | 1434 m | Am-II, ν(C–N) + δ(NH) or Am-II', ν(C–N) |

Abbreviations: vw, very weak; w, weak; m, medium; s, strong; sh, shoulder; ν, stretching; δ, deformation; β, in-plane; Am-II', deuterium substituted Am-II; Am-I', deuterium substituted Am-I.

### 3.3.2. SEIRAS characterization of IMHA self-assembled monolayer formation

In this experiment, several monolayers with different IMHA and fragment ratios were formed on a gold surface in ethanol solution. The formation process was monitored by recording SEIRAS spectra with a 15-second time resolution during the first 20 minutes and a 2-minute resolution for up to 90 minutes of monolayer formation. Figure 28A shows the time-dependent SEIRAS spectra of IMHA monolayer formation in ethanol. Am-I and Am-II vibrations have their TDM vectors perpendicular to each other in planar –CO–NH– amide bond (Figure 29).[156] TDMs conveniently correlate with the spectral intensities, as the vibrational modes are highly dependent on TDM orientation with respect to the surface, according to the metal surface selection rule. Any changes in amide plane orientation will be reflected in the Am-I to Am-II intensity ratio.[39] Some spectral changes can already be observed in the first seconds of SAM formation. A prominent feature of Am-I vibration peak is visible at 1649 $cm^{-1}$ with a shoulder at 1626 $cm^{-1}$ and stretching of the C–N group of imidazole ring at 1487 $cm^{-1}$. Am-II band at 1558 $cm^{-1}$ appeared later and dominated in intensity for the rest of the measurement time. Previous

studies on atomically flat Au surface have shown Am-II band to be the most intense absorption in SAMs formed from alkanethiols with interchain amide groups. [165–168] This demonstrates a direct relationship between strong Am-II absorption and its vertical orientation with respect to the surface.

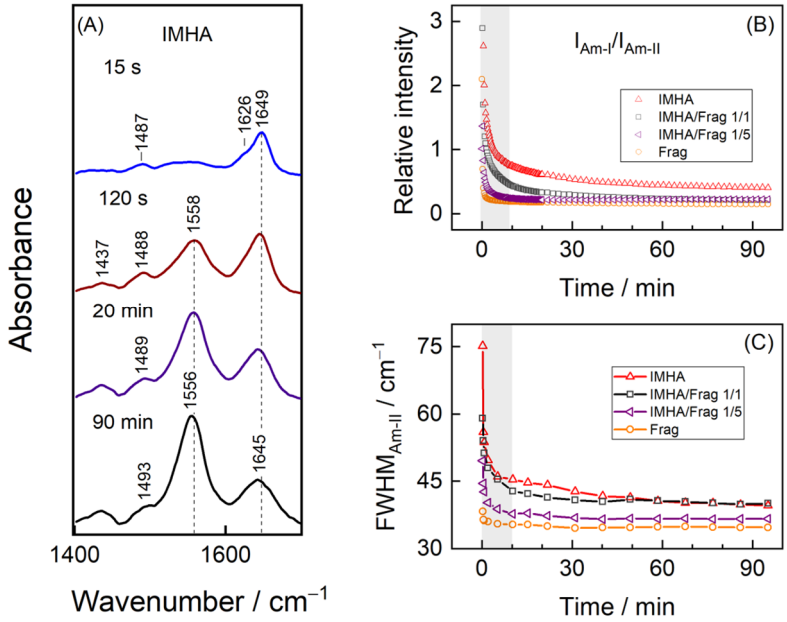


Figure 28. (A) SEIRAS spectra of IMHA SAM in ethanol adsorption solution at various incubation times. (B) The time-dependent evolution of the Am-I/Am-II intensity ratio of SAMs composed of IMHA, Frag, and their mixtures (1/1 and 1/5). (C) FWHM of Am-II spectral mode of different composition SAMs.

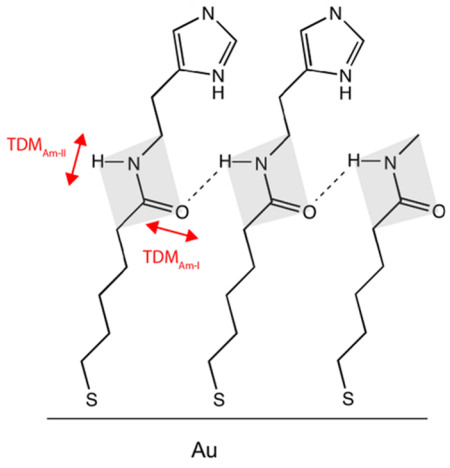


Figure 29. Two-dimensional schematic representation of the interchain hydrogen bond network at the amide group in a binary IMHA/Frag monolayer on Au. Shaded

regions represent amide group planes, while red lines illustrate the approximate directions of the Am-I and Am-II transition dipole moment (TDM) vectors.

The intensity and position of amide spectral modes provide valuable information, as they are heavily influenced by the strength of hydrogen bonding. Am-I is sensitive to the hydrogen bonding strength at the carbonyl group and the coupling between neighboring carbonyls. In contrast, Am-II is primarily affected by H-bonding at the N–H site.[17] As the hydrogen bonding interaction weakens at C=O···H and N–H···O sites, Am-I shifts to higher frequencies, while Am-II shifts to lower frequencies.[156,168,169] Based on this information, it can be inferred that SAM formation negatively impacts the intrachain packing of IMHA at the amide group.

Comparing the ATR-FTIR spectrum of bulk IMHA solution with an absorption maximum for Am-II at 1573 $cm^{-1}$ to IMHA on a gold surface (15 s), a downshift by 21 $cm^{-1}$ to 1552 $cm^{-1}$ is observed. It increases to 1559 $cm^{-1}$ within the next few minutes and then decrease again by several $cm^{-1}$ over the entire experiment (90 min) (Figure 30).

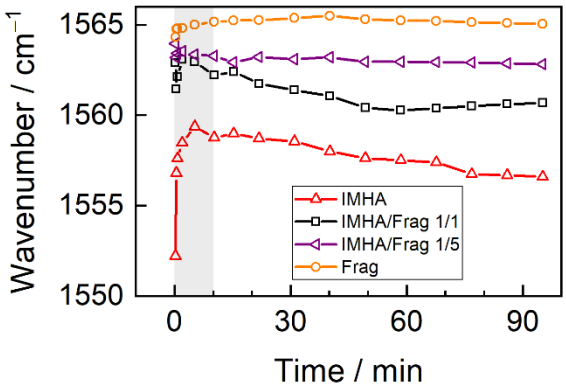


Figure 30. Adsorption time dependency of Am-II wavenumbers of varied composition SAMs.

The difference in ATR-FTIR and SEIRAS Am-II absorbance peak positions with a $\delta$ = 14–21 $cm^{-1}$ can only be explained by a reduction in hydrogen bonding strength. For Am-I, only a minor and steady frequency decrease is observed during the initial minutes, and virtually no changes for the remainder of the time. Figure 28B shows a reduction of the Am-I/Am-II ratio from 5.2 to 0.8 for the IMHA monolayer during the first 10 min of formation. This implies that the amide planes reorient into a more vertical alignment as the molecules adsorb onto the Au surface. The reorientation is

necessary for forming a robust lateral hydrogen bond network within molecules in the SAM.

As mentioned, several SAMs composed of various IMHA and fragment molecule ratios were tested. The synthesized fragment molecule retains all structural features of IMHA except for the imidazole head group. By increasing the concentration of the fragment molecule in the SAM, the steric confinement of the Im group should decrease, which should, in turn, alter adsorption properties observable through SEIRAS monitoring. Indeed, the changes in SAM formation dynamics are evident when comparing different SAM compositions. The amide group reorientation process is faster for monolayers with higher fragment molecule concentrations. These monolayers also exhibit lower Am-I/Am-II ratio values for fully formed SAMs. For instance, for the SAMs formed from 100, 50, 20, and 0 mol% of IMHA, this ratio decreased from 0.4 to 0.2, 0.2, and finally to 0.1. Furthermore, reducing the amount of IMHA in SAMs also led to a narrowing of the Am-II peak (Figure 28C), suggesting a more homogenous hydrogen bond strength distribution across the SAM at a longer formation time. It appears that the relatively large and bulky Im group in IMHA hinders the packing of molecules at the amide group and the formation of a uniform hydrogen bond network.

Recent studies in our laboratory, which involved temperature-controlled Raman measurements and theoretical modeling, demonstrated that the Im ring's ν(C2–N3) + β(C2H) mode at around 1490 $cm^{-1}$ is dependent on hydrogen bond strength at the N1/N3 atoms.[128] DFT predictions revealed that interaction with one water molecule results in a vibrational shift to higher energy by 2–6 $cm^{-1}$. The addition of a second $H_2O$ molecule leads to a total 9 $cm^{-1}$ shift. A clear connection was found between higher energy vibrations of ν(C2–N3) and stronger hydrogen bonding interaction of the Im ring.

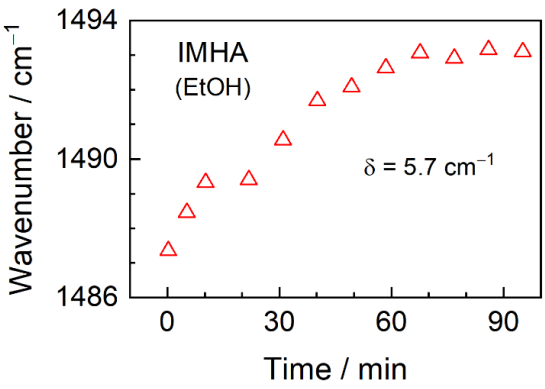


Figure 31. Dependency of the ν(C2–N3) + β(C2H) vibration frequency of the imidazole ring on the SAM formation time.

In the SEIRAS spectrum, a decrease in wavenumbers from 1494 $cm^{-1}$ for bulk IMHA (measured by ATR-FTIR) to 1487 $cm^{-1}$ for IMHA in the monolayer is observed at the beginning of adsorption. This can be explained by the reduction in hydrogen bond strength in 0.5 mM IMHA EtOH solutions. While adsorbed at the gold surface, molecules reorient into more orderly, solid-like SAM, and the peak position shifts upward (Figure 31). This suggests that the Im, initially more loosely bonded, starts to engage in stronger hydrogen bonding, and around the 60-minute mark, it reaches the maximum value, after which no changes in peak position are observed. This does not coincide with the Am-I/Am-II ratio reaching a plateau in approximately 30 minutes, indicating that the Im properties at the interface are directly dependent on the structure and packing of the interchain amides.

### 3.3.3. SEIRAS analysis of the structure of IMHA SAMs

Midrange and high-range spectra were compared to understand the influence of SAM composition on its structure. Midrange spectra were obtained from SAMs in ethanol, while high-range spectra were taken from SAMs in heavy water ($D_2O$) (Figure 32). A careful ethanol/$D_2O$ exchange was performed to (i) eliminate interference from ethanol in aliphatic and aromatic C–H stretching regions and (ii) shift N–H and O–H vibrational modes to the region of N–D and O–D stretching.

The analysis of the Am-I/Am-II ratio in the midrange revealed a trend towards SAM molecule orientation becoming more perpendicular to the surface as more fragment molecules were introduced into the SAM solution. This is likely due to decreased steric hindrance created by the bulky neighboring Im endings on IMHA molecules. This observation is indirectly supported by an 8.5 $cm^{-1}$ Am-II mode frequency shift to higher energy, which can be explained by stronger N–H group hydrogen bonding interaction. Furthermore, the decrease of bandwidths for Am-I from 48 to 35 $cm^{-1}$ and for Am-II from 44 to 41 $cm^{-1}$ suggests a more uniform hydrogen network. The weak mode at 1493 $cm^{-1}$, appearing more like a shoulder, is detected only in pure IMHA SAM and is assigned to the combined vibrations of $\nu$(C2–N3) + $\beta$(C2H). Other vibrations related to the Im are found in the high-frequency range as two strong peaks at 3115 and 3152 $cm^{-1}$, which are assigned to the stretching vibrations of C2H and C5H, respectively (Figure 32B). The absence of these bands in the pure fragment SAM spectra confirms their association with Im motions. While the intensity of these peaks was expected to decrease with a smaller proportion of IMHA in the SAM, the intensity remained at a similar level for all IMHA/Fragment ratio mixes used in the $D_2O$ environment.

This can only be explained by the reorientation of the Im to an increasingly perpendicular orientation to the surface as the IMHA concentration decreases in the SAM. Additionally, the alignment in the $D_2O$ environment was observed to be more perpendicular than in the deuterated ethanol-$d_6$ one (Figure 33). This can be evidenced by comparing the C–H stretching doublet intensity with the unchanged intensity of the lower energy C–H stretching vibrations originating from the aliphatic tail.

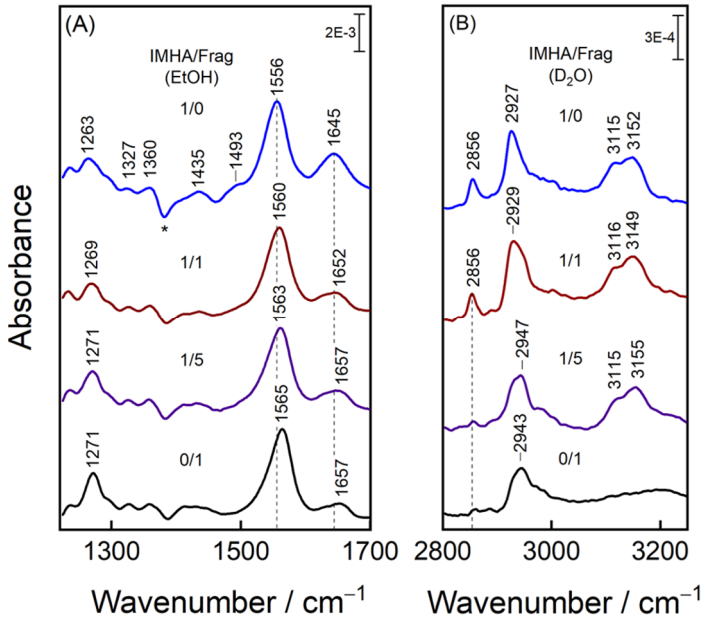


Figure 32. (A) SEIRAS spectra of IMHA, binary IMHA/Frag (1/1 and 1/5), and Frag SAMs at the 90$^{th}$ minute of adsorption in ethanol incubation solution within the 1220–1700 $cm^{-1}$ spectral range. The asterisk denotes the negative band that appears due to the withdrawal of ethanol molecules from the Au surface. (B) Spectra of SAMs with the same composition after carefully exchanging ethanol with $D_2O$ in the 2800–3250 $cm^{-1}$ spectral range.

The peak in the 2943–2947 $cm^{-1}$ frequency region (Figure 32B) is attributed to the symmetrical stretching of the $CH_3$ motion from the fragment molecule's end group. The nitrogen atom's induction effect is responsible for this mode's relatively high position.[162] Other aliphatic chain modes assigned to $\nu_s(CH_2)$ and $\nu_{as}(CH_2)$ can be observed at 2856 and 2927 $cm^{-1}$ frequencies, respectively. Due to the surface selection rule, their intensity depends on the alignment of the carbon chain relative to the surface plane. An acute decrease in intensity for symmetrical $CH_2$ stretching at 2856 $cm^{-1}$ is observed when comparing bicomponent 1/5 SAM to 1/1. This behavior can be explained by adopting a more vertical orientation for the carbon chain relative to the

surface, as the transition dipole moments (TDMs) for methylene groups become more parallel and less active in SEIRAS. Moreover, an increasing intensity of the symmetric $CH_3$ stretching vibrations from the fragment molecule is observed without detecting its asymmetric counterpart $\nu_{as}(CH_3)$. This suggests an orthogonal orientation of the methyl groups to the surface in SAMs.

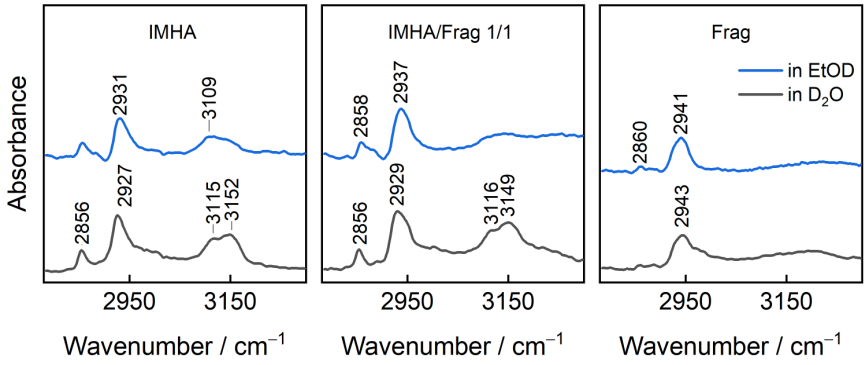


Figure 33. SERAS spectra of IMHA, Frag, and binary (IMHA/Frag 1/1) monolayers in ethanol-$d_6$ (EtOD) incubation solution (60 min) and $D_2O$.

For a densely packed, orderly SAM, symmetrical and asymmetrical $CH_2$ group vibrational modes are known to have frequencies near 2850 and 2917 $cm^{-1}$, respectively. Whereas less ordered structures exhibit upshifted high-range methylene vibrations. [98,170–172] In SEIRAS spectra, the observed bands are shifted by approximately 10 $cm^{-1}$ to higher frequencies than the ATR-FTIR. This suggests a less ordered or even a melted state structure of alkane chains in the SAM, despite the vertical alignment evidence discussed earlier. The amide and imidazole groups interfere with the orderly packing of carbon chains. For comparison, molecules measured in the bulk phase had almost the same frequencies as those in the SAM case: 2852 and 2926–2928 $cm^{-1}$.

Based on the observations from SEIRAS data of various composition SAMs, it can be concluded that decreasing the relative IMHA concentration (i) affects the imidazole ring, amide group, and alkane chain orientation, leading them to adopt a more perpendicular state to the surface, and (ii) strengthens hydrogen bonding interaction at the N–H group of the amide moiety. Therefore, it can be stated that mixed SAMs of IMHA and fragment molecules have stiffer head and tail segments and a more labile and accessible functional imidazole ring group for interactions.

### 3.3.4. Potential-dependent SEIRAS analysis of hydrogen bonding in IMHA SAMs

A series of potential-dependent measurements were performed with various SAM compositions to understand better the effects of changing potential environments on the monolayers and to further investigate hydrogen bonding interactions at the Im group of the IMHA molecule. Figure 34A and Figure 34B display spectra of the IMHA monolayer at different potentials set for the gold electrode (vs. Ag/AgCl), starting from 0.3V, –0.1V, –0.5V, and returning to positive 0.3V from negative polarization.

Interestingly, when the potential changes from 0.3 to –0.5 V, both Am-II and Am-I shift to lower wavenumbers by 5–6 $cm^{-1}$. This is associated with weakened hydrogen bonding at the N–H site and strengthened bonding at the C=O group. However, we are limited in interpreting the cause of this wavenumber shift irregularity. One possible explanation is that the enhanced contact between carbonyl and water molecules (C=OH···OH) at the negatively charged interface is connected to the lower hydrogen bonding interaction strength between interchain N–H···O=C groups.

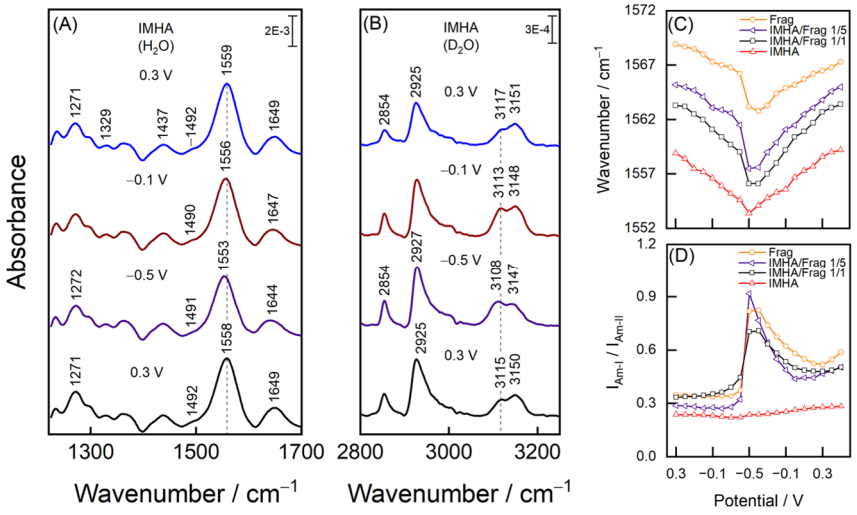


Figure 34. Potential-dependent SEIRAS spectra of the IMHA monolayer in (A) the midrange region in $H_2O$ and (B) the C–H stretching region in $D_2O$. (C) The relationship between Am-II wavenumbers and electrode polarization, and (D) the dependence of the Am-I/Am-II intensity ratio on electrode polarization.

The Am-II wavenumber dependence on potential is consistent for all investigated SAM compositions and correlates with progressively decreasing H-bonding strength towards negative electrode polarization (Figure 34C). This weakening is caused by the amide planes reorienting into a less

perpendicular arrangement with the surface (Figure 34D). This is accompanied by a significant increase in the Am-I/Am-II ratio at –0.5 V for all but the IMHA monolayer. Strong intermolecular interactions at the Im groups in the IMHA monolayer (Figure 34D, red line) cause rigidity in the molecular structure, reducing the flexibility of the amide group. Changes in Am-I band shape and significantly larger potential dependence on the Am-I/Am-II intensity ratio were observed in other SAM compositions (Figure 35). Each SAM containing fragment molecule exhibited an unexpected rise in the low-frequency component at 1628–1630 $cm^{-1}$ of the Am–I band at –0.5 V bias. Such low wavenumbers in proteins have previously been associated with a rigid and highly ordered β-sheet secondary structure element,[18]. Still, in this case, changes are attributed to the closer alignment of C=O dipoles with external field lines (resulting in increased Am-I intensity) and the development of hydrogen bonding interactions with $H_2O$ molecules from the solution phase.

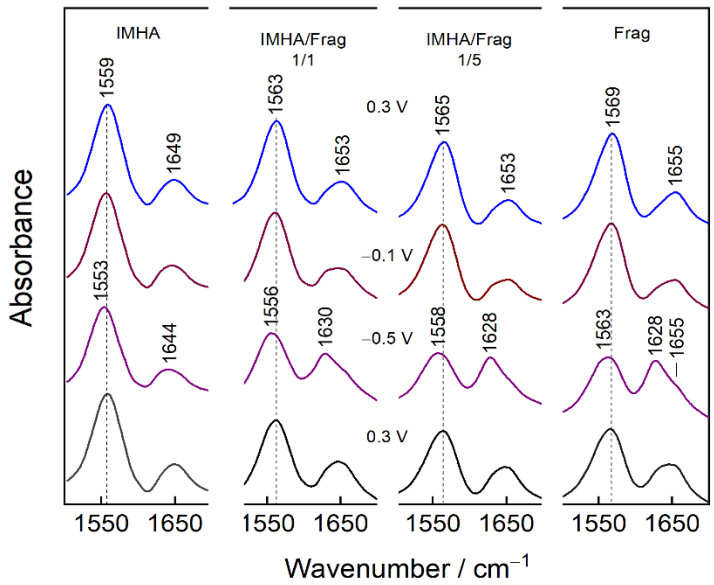


Figure 35. Potential dependent SEIRAS spectra of IMHA, IMHA/Frag 1/1, 1/5, and Frag monolayers in amide region in $H_2O$.

Information on the Im of the monolayer in SEIRAS spectra can be obtained from the 1492 $cm^{-1}$ mode in $H_2O$ and the doublet bands in $D_2O$ at 3117 and 3151 $cm^{-1}$. Although the former mode is not well-defined, the doublet intensity provides a clearer picture of changes in the Im group caused by electric potential. The lower frequency component at 3117 $cm^{-1}$ for the T-I form is attributed by DFT calculations and the literature to =C2–H stretching, while the 3151 $cm^{-1}$ mode is attributed to the =C5–H.[148,173] These vibrations

become coupled for the molecule in the T-II state and participate in out-of-phase and in-phase vibrational motion, respectively. Due to the adsorption-induced transition from T-I to T-II form, T-II (N1, N3–D) is considered the main Im tautomeric form in our system.[128,146] It has been identified that the position of the =C2–H mode is more sensitive to changing potential. When electrode polarization was changed from 0.3 to –0.5 V, the frequency tuning rate of –10.4 and –6.3 $cm^{-1}V^{-1}$ for the low and high-frequency modes was observed (Figure 36B). Similar tuning rates of –8.3 and –4.0 $cm^{-1}V^{-1}$ for 1/1 component ratio SAM and –14.1 and –8.5 $cm^{-1}V^{-1}$ for 1/5 ratio SAM were seen in bicomponent monolayers.

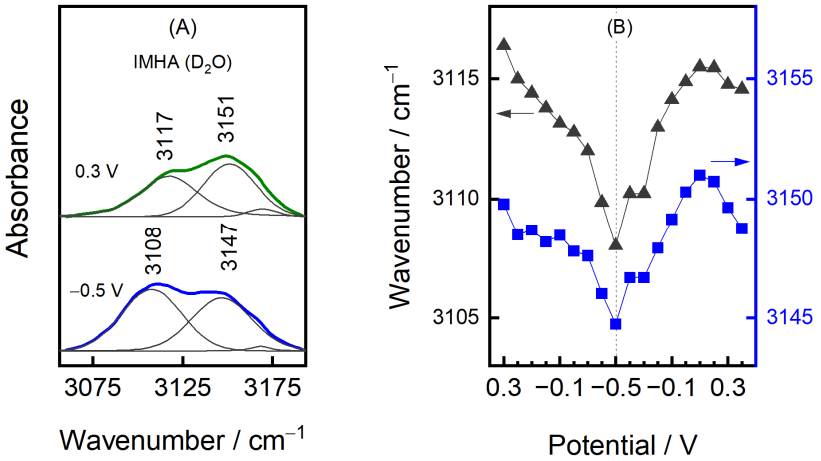


Figure 36. Analysis of the ring C–H stretching modes at 3117 and 3151 $cm^{-1}$. (A) SEIRAS spectra of IMHA SAM in $D_2O$ at 0.3 and –0.5 V potentials in the 3056–3193 $cm^{-1}$ range. (B) The relationship between 3117 and 3151 $cm^{-1}$ wavenumber and the electric potential.

To elucidate the influence of hydrogen bonding interactions on the vibrational frequency of ν(=C–H) modes, DFT simulations were conducted on 4-ethyl-1-imidazole in the Tautomer-II form (N1, N3-D) with zero, one, and two explicit $D_2O$ molecules (Figure 37). It was found that, compared to the N3–D deuteron, the N1 atom in T-II is more susceptible to hydrogen bonding. Furthermore, in contrast to the contact at the N1 atom, which increases the frequency by 8 $cm^{-1}$, the N3–D group (N3–D···$D_2O$) interaction only weakly affects the vibrational frequency of the modes ($\delta = -3$ $cm^{-1}$). A compound in the T-I form exhibited almost identical behavior. The N1 hydrogen bond is noticeably shorter than the N3–D hydrogen bond by 8.5 pm, suggesting greater stability than the ImN1···$D_2O$ complex. According to a supersonic jet FTIR spectroscopy study, Im prefers to accept a hydrogen bond N···H–O over donating it N–H···O.[174]

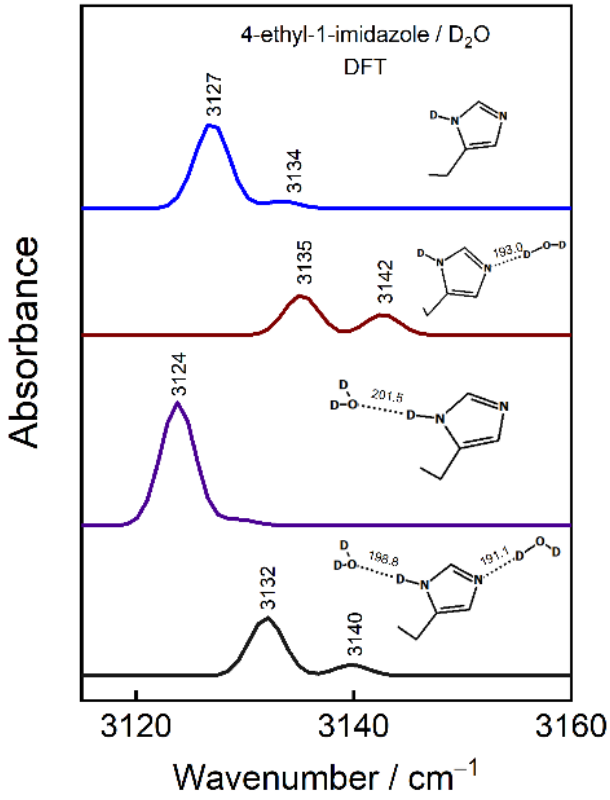


Figure 37. DFT spectra in Im ring =C–H stretching region of 4-ethyl-1-imidazole in T-II form without and with explicit $D_2O$ molecules at N1 and/or N3–D. The hydrogen bonding lengths are indicated in pm. Vibrational frequencies were scaled.

Adding a second heavy water molecule to the Im-$D_2O$ complex further stabilized Im. Hydrogen bonds for the N1 and N3-D sites were shortened by –1.89 and –2.69 pm, respectively, as a result of coordination with two $D_2O$ molecules. To experimentally confirm this, a model compound of imidazole-4-methanol (Im–$CH_2$–OH) was measured by FTIR in different polarity solvents, methanol-$d_4$ and $D_2O$ (Figure 38). The data reveal a noticeable decrease in the frequency of the ν(=C–H) modes in methanol-$d_4$, where weaker hydrogen interactions are expected compared to $D_2O$.

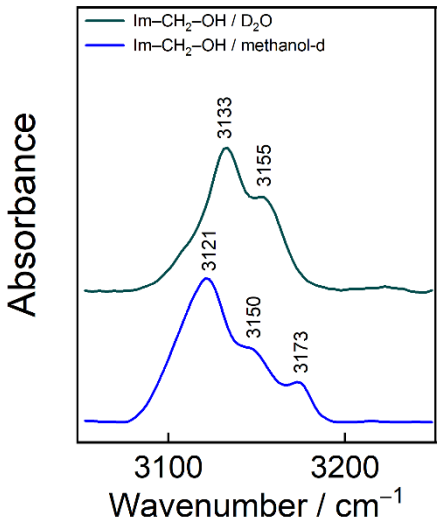


Figure 38. Infrared absorption spectra in the transmission mode of the imidazole-4-methanol (Im–$CH_2$–OH) dissolved in methanol-$d_4$ and $D_2O$.

Theoretical and experimental results suggest that a decrease in the hydrogen bond strength of imidazole corresponds to a shift in the =C–H frequency towards lower wavenumbers. Figure 36, which shows the potential dependency, clearly illustrates decreasing wavenumbers with negative electrode polarization, indicating a reversible reduction in the strength of the hydrogen bond between Im and its surroundings. The vibrational Stark effect could explain such a wavenumber change; however, as demonstrated in Figure 39, the frequency tuning rates for Im-SAMs were not substantially different in environments with varying ionic strengths.

A potential explanation for the decrease in hydrogen bonds could be the structural changes in interfacial water. The dielectric constant of water is reduced near surfaces or confined spaces due to the reorientation of water molecule dipoles.[175] The bias electric potential enhances overall polarization through field-dipole interactions, competing with the isotropic hydrogen bond network. With significantly negative polarization, O–D dipoles are oriented away from the bulk and toward the surface.[176] In summary, the configuration of water molecules at the electrified interface influences the strength of hydrogen interactions with exposed Im groups.

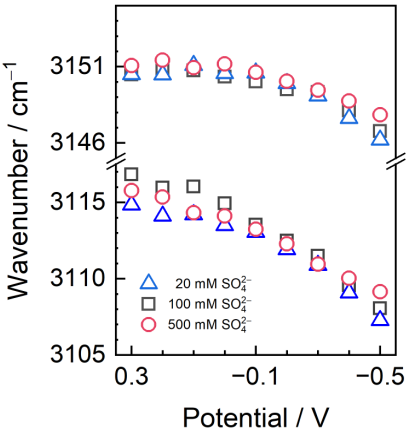


Figure 39. The dependence of ν(=C5–H) and ν(=C2–H) modes positions on the electric potential in the $D_2O$ solutions of different ionic strengths. SAM was IMHA/Frag 1/1.

Furthermore, an explanation is required for the relative intensities of the 3115 and 3150 cm$^{-1}$ mode. Calculations suggest that the displacement vectors of the T-II form Im ring, for the low and high-frequency modes, lie within the Im plane parallel to the C2–H bond direction and nearly parallel to the N3-D, respectively (Figure 40).

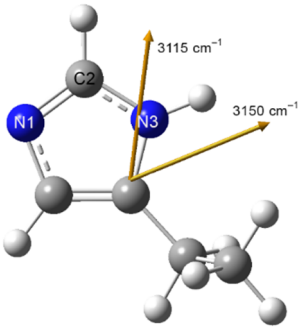


Figure 40. Displacement vectors calculated for 3115 and 3150 cm$^{-1}$ modes of the 4-ethyl-1-imidazole in Tautomer II form.

As a result, changes in the Im ring's surface orientation are reflected in the relative intensities of the 3150/3115 cm$^{-1}$ mode. When the shift to negative potentials decreases the $I_{3150}/I_{3115}$ intensity ratio, the imidazole tilts to a position where the C2–H bond is slightly more exposed to the solution. Moreover, it is observed that, compared to the two-component SAMs, the monolayer composed solely of IMHA exhibits somewhat reduced potential-induced intensity changes. This is likely because the Im groups appear to be more inclined to engage in intramolecular interactions with each other.

## 3.4. Interim conclusions

To gain a deeper understanding of the interactions between the Im and its local environment at the organic layer-water interface on electrically polarized electrodes, self-assembled monolayers (SAMs) composed of Im-terminated alkanethiol molecules and surface dilutor fragment molecules were studied. H/D substitution SEIRAS was employed to investigate the kinetics of SAM formation and the structure of the interfacial Im ring. It was found that during the initial 30 minutes of incubation, the amide groups within the alkane chains adopted an optimal surface orientation independent of SAM composition.

The frequency shift of the Im structure marker band around 1490 $cm^{-1}$ indicated that changes in the SAM terminal functional group continued until 60 minutes of incubation period. These alterations were associated with the gradual formation of stronger hydrogen bonds in the Im group. A structurally rigid organic layer with amide groups only partially engaged in an ideal hydrogen-bonding network is produced by the IMHA-based SAM.

Incorporating a surface dilutor fragment molecule altered the Im orientation to be more vertically aligned, enhancing the hydrogen bonding network between the amide groups. Im's stretching modes (=C–H) at 3115 and 3150 $cm^{-1}$ exhibited a reversible decrease in vibrational frequencies under negative electric bias, with frequency tuning rates of –10.4 and –6.3 $cm^{-1}V^{-1}$. This frequency reduction has been attributed to the weakening of the hydrogen bond between the Im and the adjacent water at the negatively charged interface.

# 4. FORMATION OF TETHERED BILAYER LIPID MEMBRANES ON GOLD SURFACE PROBED BY IN SITU SEIRAS

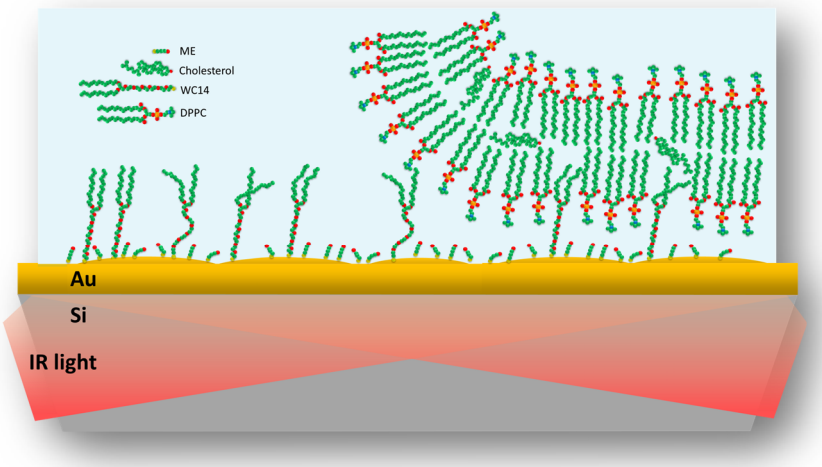

## 4.1. Introduction

Tethered bilayer lipid membranes (tBLM) are a versatile platform for mimicking biological processes and are helpful in biosensor and biomedical screening applications.[10,97,177–180] One of their key advantages is the presence of an exchangeable solution reservoir between the solid substrate (gold electrode) and the bilayer, which enables the incorporation and stability of transmembrane proteins.[181,182] This separation also allows for the mobility of inserted proteins required for their function.

The tBLM structure is typically formed in two steps. First, the anchoring layer is formed from polar peptides, carbohydrates, polymers, or self-assembled monolayers of thiol molecules on the gold substrate.[70,180,183–185] Second, lipid vesicles are fused onto the anchoring layer to form a planar lipid bilayer. The SAM approach is simple, reproducible, yields low defect density, and enables control of bilayer fluidity. Gold is a favorable solid substrate for tBLMs because of its strong chemical bond with sulfur atoms of alkanethiol molecules. A mixed SAM is formed using a short thiol with a hydroxyl functional group and a long-chain lipid anchoring thiol on the gold substrate to create a water reservoir between the electrode and bilayer. This method ensures that an exchangeable solution reservoir is present, enabling the transmembrane proteins to remain stable and mobile.[70,186]

The composition and structure of the anchoring SAM strongly influence the stability and functional properties of tBLMs. And there is still a limited understanding of the molecular-level structure and formation of mixed monolayers in solution.[98,132,182,187–189] This knowledge gap is due to the scarcity of techniques available for providing molecular information from the electrode/solution interface. However, SEIRAS is a promising tool for probing the structure, adsorption peculiarities, and orientation of adsorbed molecules at the electrochemical interface with sub-monolayer sensitivity and molecular specificity.[190,191] Previous studies have successfully employed the in situ SEIRAS approach to analyze adsorbed peptide's secondary structure, self-assembled monolayer's conformation, and surface attached biosensor's function.[190–193] The present study aims to use in situ SEIRAS to investigate the development of an anchoring monolayer and the formation of a bilayer at a gold electrode.

## 4.2. Results and discussion

### 4.2.1. Mixed anchoring SAM formation

A mixed self-assembled monolayer was formed on a gold substrate using a combination of long-chain (WC14) and short-chain (βME) thiols (see Figure 21). This approach enabled the construction of a bilayer anchoring mixed SAM, which had previously been used for studying the structure and function of pore-forming toxins[94,194] and the interaction of proteins with a membrane.[186] The optimal adsorption solution for the self-assembly of the anchoring monolayer was a mixture of WC14 and βME thiols in a 30/70 mol% ratio.[189]

Figure 41 shows the evolution of SEIRAS spectra during the formation of a mixed monolayer on gold using WC14/ME (30/70 mol%) thiol molecules from a methanol-$d_4$ ($CD_3$–OD) solution. The introduction of thiol molecules resulted in the appearance of strong bands at 1464, 1350, and 1157 $cm^{-1}$ in the fingerprint spectral region after 60 minutes of incubation (Figure 41A). The band at 1464 $cm^{-1}$ corresponds to the predominant $CH_2$ scissoring deformation vibration of the alkyl chains, which is broadened due to the presence of polyethylene group units (PEG) in the gauche conformation and PEG in an amorphous structure, with vibrational bands expected at 1463–1465 and 1460 $cm^{-1}$, respectively.[195] The intense band near 1350 $cm^{-1}$ is identified as the wagging vibration of the PEG units $CH_2$ groups in the gauche conformation.[195] The broad and intense absorption band at 1157 $cm^{-1}$ is attributed to the C–O–C group's characteristic asymmetric stretching vibrational mode, $\nu_{as}$(C–O–C).[98,189,195–202] It is important to mention that the strong IR absorption of the Si prism below 1000 $cm^{-1}$ can alter the shape of this peak.[203] According to previous studies,[98,196–202] the position of the band associated with this mode provides information on the structure of the PEG component of the molecule. The relatively high frequency value observed in this work suggests the presence of a predominantly amorphous structure.[195,202]

Comparing the width of this band in SEIRAS (Figure 41A) with the corresponding band of WC14 in solid state IR spectrum near 1114/1147 $cm^{-1}$ (Figure 41C), it can be inferred that there is a prevalence of one relatively uniform conformational form of PEG chains in the monolayer. This finding is consistent with previous reports[195] suggesting the amorphous structure of the PEG chain in oligoethylene-glycol-terminated SAMs is highly solvated by water and able to prevent adsorption of proteins, unlike the ‘all-trans’ conformation.

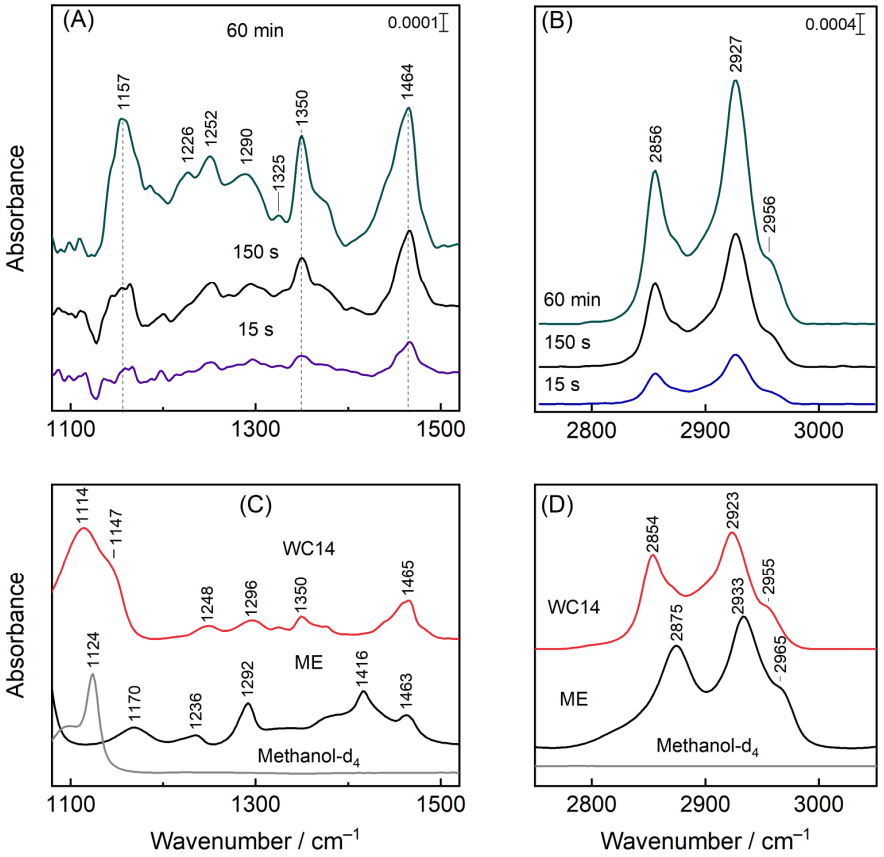


Figure 41. SEIRAS spectra measured at various times during the formation of a mixed SAM (WC14/βME, 30/70 mol%) from a methanol-$d_4$ solution. The spectra are presented (A) in the fingerprint spectral region (1080–1520 $cm^{-1}$) and (B) in the C–H stretching frequency region (2750–3050 $cm^{-1}$). The reference spectrum was obtained from pure methanol-$d_4$ before introducing thiol molecules into the working solution. (C, D) IR spectrum of solid-state WC14, βME, and methanol-$d_4$ in the corresponding spectral regions.

Mixed SAM was formed in a methanol-$d_4$ solution, and only one intense band near 1124 $cm^{-1}$ belongs to the solvent molecules in the investigated spectral region (Figure 41C). This explains some spectral perturbations in the vicinity of the C–O–C stretching band due to the adsorption/desorption of solvent molecules during the self-assembly process. In the high-frequency region (Figure 41B), absorption bands attributed to the symmetric $\nu_s(CH_2)$ and asymmetric $\nu_{as}(CH_2)$ stretching vibrations of methylene chains are observed at 2856 and 2927 $cm^{-1}$, respectively.[98,189] The frequency of asymmetric vibration band $\nu_{as}(CH_2)$ is indicative of the ordering of alkyl chains, with highly ordered SAMs displaying values in the range of 2917–2919 $cm^{-1}$,[204–206] while disordering results in an upshift of the frequency. Notably, both peaks

in SEIRAS spectrum are upshifted by several wavenumbers compared to the IR spectrum of solid-state WC14 (Figure 41D), suggesting a relatively disordered structure of the alkyl chains in the mixed SAM. All spectral bands in SEIRAS spectra were linked to the WC14 compound, and no spectral characteristics for the βME were detected. The βME bands located at 1416 and 2875 $cm^{-1}$ (as shown in Figure 41C, D) were not observable in SEIRAS spectra (Figure 41A, B). An increase in the relative intensity of the $\nu_{as}$(C–O–C) band at 1157 $cm^{-1}$ of the PEG segment is observed over time when compared to the scissoring deformation band of $CH_2$ at 1464 $cm^{-1}$ (Figure 41A). It has been demonstrated in other studies[98,189] that relative intensification of asymmetric stretching of C–O–C mode is connected with more vertical alignment of WC14 molecule, which suggests that reorientation of molecules into a more upright position occurs during the self-assembly process.

### 4.2.2. Formation of a tethered bilayer lipid membrane

The formation of tBLM from a DPPC-$d_{62}$/cholesterol-$d_7$ mixture in the phosphate buffer solution was monitored in situ by SEIRAS. Figure 42 shows three distinct spectra representing the initial, intermediate, and final stages of formation in the range of 2000 to 3700 $cm^{-1}$. The upward peaks represent newly adsorbed molecules, while negative peaks indicate the withdrawal of previously absorbed molecules from the surface. Please note, that reference spectrum was fully formed SAM spectrum, therefore any appearance of modes related to SAM indicate its structural alterations. Interaction with the vesicles and planar bilayer formation may disturb the order of the monolayer and cause spectral changes. After 15 seconds of bilayer formation, a low-intensity positive peak near 2979 $cm^{-1}$ becomes visible in the SEIRAS spectrum. It corresponds to the asymmetric stretching vibration of the $CH_3$ group and may be related to the changes in the orientation of the terminal methyl group of adsorbed WC14. At the same time, a broad negative peak near 3546 $cm^{-1}$ appears in the SEIRAS spectrum, which is assigned to the O–H stretching vibration.

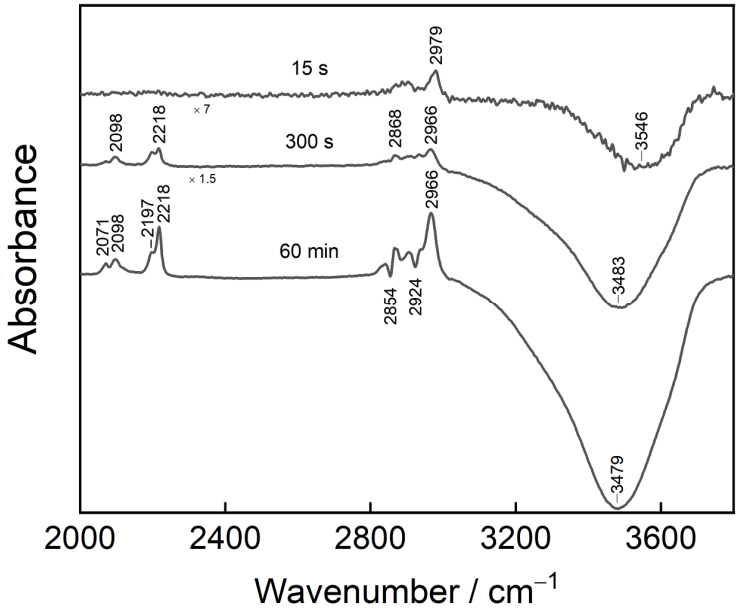


Figure 42. SEIRAS-difference spectra representing initial, intermediate, and final stages of tBLM formation (DPPC-$d_{62}$/cholesterol-$d_7$, 60/40 mol%) on a mixed SAM (WC14/ME, 30/70 mol%) in an aqueous solution.

After 300 seconds of incubation, four positive-going bands appear in the SEIRAS spectrum at 2071, 2098, 2197, and 2218 $cm^{-1}$ due to the stretching vibrations of the $CD_2$ and $CD_3$ groups of DPPC-$d_{62}$. Specifically, the bands at 2071 and 2218 $cm^{-1}$ correspond to the symmetric and asymmetric $CD_3$ stretching vibrations $\nu_s(CD_3)$ and $\nu_{as}(CD_3)$, respectively, while the bands at 2098 and 2197 $cm^{-1}$ are assigned to the symmetric and asymmetric stretching modes of the $CD_2$ group $\nu_s(CD_2)$ and $\nu_{as}(CD_2)$.[207–210] To better understand SEIRAS spectral features, IR spectra of bulk cholesterol-$d_7$ and DPPC-$d_{62}$ were measured (see Figure 43). The $CD_3$ vibrational modes are more intense in the surface spectrum than in the bulk infrared spectrum. Additionally, some contribution from cholesterol-$d_7$ may be present in the 2218 $cm^{-1}$ absorption band of the SEIRAS spectrum (see Figure 42).

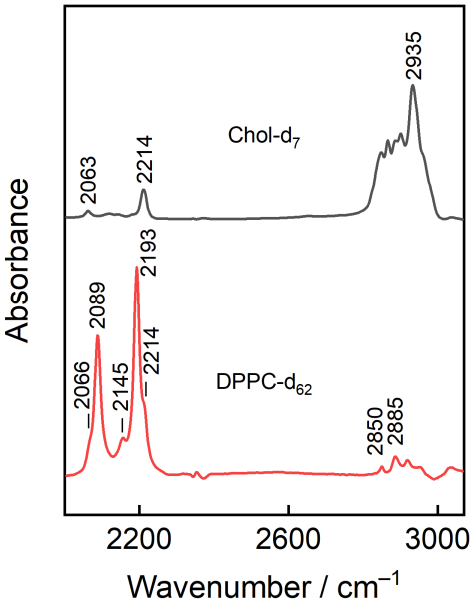

Figure 43. IR spectra of bulk cholesterol-$d_7$ and DPPC-$d_{62}$.

The intensity of 2071, 2218, and 2966 $cm^{-1}$ band and the negative water absorption feature near 3479 $cm^{-1}$ increase with an incubation time of 60 minutes. Notably, the latter band shifts towards lower wavenumbers, indicating fewer hydrogen-bonded water molecules leave the interface during the bilayer formation. The relative intensification of the $CD_3$ stretching bands may be related to approaching closer to the surface and changes in orientation of the DPPC-$d_{62}$ alkyl chains. Furthermore, negative-going features at 2854 and 2924 $cm^{-1}$ of $\nu_s(CH_2)$ and $\nu_{as}(CH_2)$, respectively, are visible after 60 minutes of bilayer formation, which are linked with changes in the alignment of the alkyl chains of adsorbed WC14 molecules. Overall, the decrease in relative intensity and redshift of the stretching $CH_2$ bands indicate a more perpendicular and orderly orientation of the WC14 alkyl chains with respect to the surface.[204–206]

Figure 44 shows the temporal evolution of SEIRAS bands during the bilayer formation process. In the first 20 minutes, changes in the DPPC-$d_{62}$ $\nu_{as}(CD_3)$ band and the anchoring monolayer $\nu_{as}(CH_2)$ band exhibit different temporal behaviors, while water withdrawal from the surface behaves similarly to the changes in DPPC-$d_{62}$. To quantitatively analyze the data, a Boltzmann model was applied to fit the experimental results:

$$y(x) = \frac{A_1 - A_2}{1 + e^{\frac{x - x_0}{dx}}} + A_2, \quad (10)$$

where $A_1$ and $A_2$ are the initial and final values of the measured parameter, and $x_0$ is the time of the process midpoint. The midpoint of the process, $x_0$, was

found to be 6.0 ± 0.35 min and 4.5 ± 0.11 min for $I\nu_{as}(CD_3)$ and $A\nu(OH)$ alterations, respectively, and 9.9 ± 0.31 min for $I\nu_{as}(CH_2)$ changes.

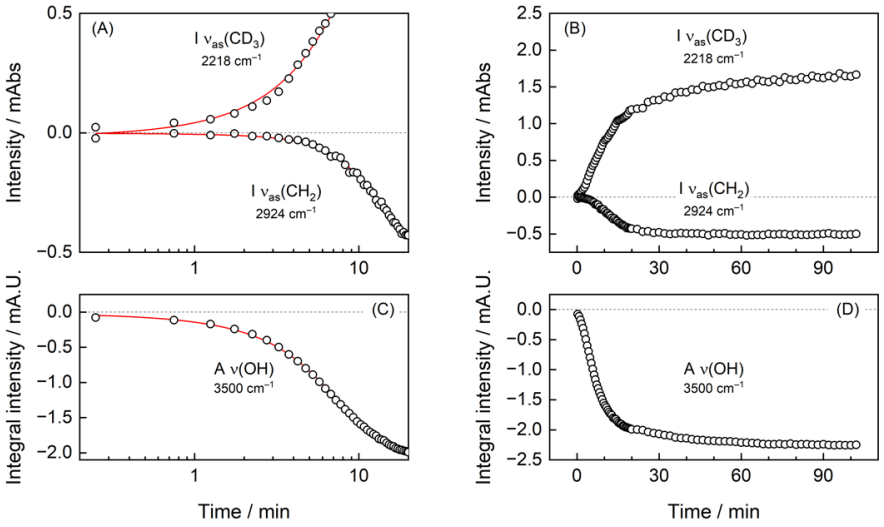


Figure 44. The temporal evolution of spectral mode intensities during tBLM formation for the first 20 minutes (A) and the full 105-minute period (B). Specifically, it shows the intensities of modes related to DPPC-$d_{62}$ adsorption and reorientation on a surface [$I\nu_{as}(CD_3)$], as well as the reorientation of anchoring molecules [$I\nu_{as}(CH_2)$]. The temporal evolution of the integral intensity of ν(OH) is related to the removal of water molecules from the surface during tBLM formation for the first 20 minutes (C) and the full 105-minute period (D). The experimental results were fitted with a Boltzmann model, represented by the red lines in the figures. The model yields a 50% process threshold at 6.0 ± 0.35 minutes [$I\nu_{as}(CD_3)$], 9.9 ± 0.31 min [$I\nu_{as}(CH_2)$], and 4.5 ± 0.11 min [$A\nu(OH)$].

The fitting of SEIRAS data revealed a two-step mechanism for the formation of the bilayer. The first step involves the adsorption of the DPPC-$d_{62}$/cholesterol-$d_7$ lipid bilayer onto the mixed anchoring monolayer with simultaneous water withdrawal from the interface. The second step consists of transforming the alkyl chains of the WC14 monolayer due to the insertion and interaction of the bilayer. After approximately 60 minutes, the spectral changes due to the bilayer formation process are essentially complete, as shown in Figure 44B and Figure 44D.

## 4.3. Interim conclusions

Surface-enhanced infrared absorption spectroscopy was used to investigate the two-step process of constructing tethered bilayer lipid membranes (tBLMs) on gold substrates. The first step involved the formation of the mixed self-assembled monolayer, and the second step involved the development of the lipid bilayer at the mixed SAM. Obtained results revealed that the ethylene

glycol chains of long-chain thiol in SAM are primarily in the amorphous state, while the alkyl chains are in the disordered state, providing the necessary flexibility for the formation of the bilayer.

The SEIRAS data showed that the formation of the bilayer lipid proceeds through two stages. The first stage involves the adsorption of lipids onto the surface and the simultaneous desorption of water from the interface. The second stage consists of the insertion and interaction of the lipids with the monolayer, leading to structural changes in the alkyl chains of the SAM. The lipid bilayer formation process was completed after approximately 60 minutes following the introduction of vesicles composed of a mixture of partially deuterated compounds DPPC-$d_{62}$/cholesterol-$d_7$.

# 5. SEIRAS STUDY OF SUBMEMBRANE WATER CONFINEMENT IN DOPC/CHOLESTEROL TBLM AT ELECTRIFIED SURFACES

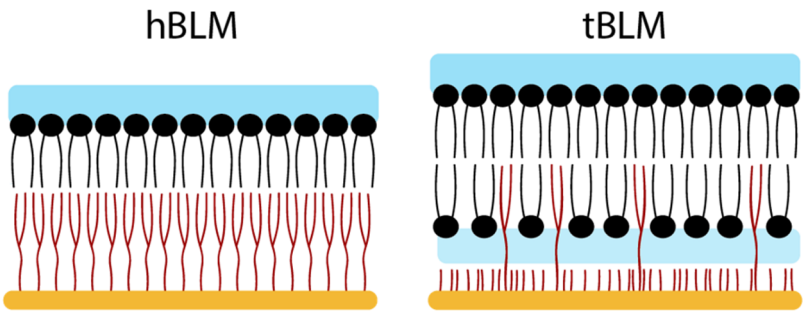

## 5.1. Introduction

Water is an essential and ubiquitous molecule in various natural and engineered systems, playing a critical role in determining their properties and performance. Its unique physicochemical properties, including a high dielectric constant, hydrogen bonding capacity, and polarity, make it vital in numerous interfacial phenomena.[211,212] The behavior of water molecules at interfaces and submembrane layers is critical in the design, function, and analysis of SAMs, tBLMs, and other biomimetic systems.[9,10]

Dielectric properties of interfacial water are smaller than those of bulk water, attributed to the reduced rotational freedom of water dipoles. Studies have shown a significant decrease in polarizability so that the ε value is approximately 2 for the first two to three water molecules within the interfacial layer.[213] However, directly measuring water dielectric properties at thin interface layers can be challenging. As infrared absorption spectroscopy is inherently sensitive to water due to its large extinction coefficient, SEIRAS adds surface specificity due to rapid electric field decay, effectively avoiding interference from bulk solutions.[140] Moreover, the metal surface selection rule makes it selective and thus a valuable tool for detecting molecular structural changes.

The O–H stretching mode, ν(O–H), absorbs infrared in a broad spectral range divided into three regions related to the motion of more loosely hydrogen-bonded multimer water at ~3600 $cm^{-1}$ and network water centered at ~3400 and ~3250 $cm^{-1}$.[214–219] The latter is sometimes considered as ice-like water mode and is attributed to coupling between collective in-phase O–H stretching and overtone of deformation vibration, $\delta(OH_2)$.[220]

Water molecules can form ordered structures, with hydrogen bonding networks oriented towards or away from the surface, depending on surface properties.[221] The behavior of water at the interface can significantly impact the adsorption, organization, and stability of SAM and tBLM, as well as their interactions with other biomolecules. Water forms stronger hydrogen bonds with polar groups of lipids than with other water molecules.[216] Studies have shown that metal surface adsorbed sBLM and water cushion supported floating bilayer lipid membranes (fBLM) become slightly lifted from the support as water molecules move towards the metal electrode at increasingly negative electric potentials.[222–224] The water structure in the submembrane is minimally affected by external potential, with positive potentials causing minor disordering effects.[214] However, potentials more negative than –0.4 V vs. Ag/AgCl electrode can cause membrane electroporation, increasing

membrane defectiveness and leading to a surge of water in the submembrane and increased capacitance.

SEIRAS studies of lipid membranes have revealed that water forms a more ordered hydrogen bonding network in the submembrane of fBLM than in the submembrane of sBLM.[214] In this work, the behavior of water in the tBLM submembrane layer was investigated using the electrochemical SEIRAS technique. One of the most critical parameters of tBLMs is the specific resistance of the submembrane reservoir.[225] The dielectric constant of water confined within the submembrane reservoir is believed to decrease, which effectively increases the Gibbs free energy of solution ions and redistributes them on both sides of the membrane, affecting the electric properties of the model membrane.

### 5.2. Spectroscopic characterization of the tBLM and hBLM membranes

To understand water sublayer formation, tBLM and hBLM membranes were created by differentiating the composition of SAM. By adjusting the SAM composition using WC14 and βME, mixed SAMs were made, leading to the formation of tBLM with DOPC and cholesterol. Conversely, when the SAM consisted solely of WC14 molecules, hBLM formation occurred. Therefore, one system has an artificially made 1–2 nm water sublayer, and the other does not. In Figure 45, mixed WC14/ME and pure WC14 formed SAM SEIRAS spectra are presented (upper spectra in A and B, respectively). All positive spectral lines are attributed to the WC14 compound as βME spectral features are weak. Negative peaks are attributed to ethanol removed from the surface as SAM was formed. Peaks at 2854 and 2925 $cm^{-1}$ in mixed SAM spectra attributed to $\nu_s(CH_2)$ and $\nu_{as}(CH_2)$ stretching vibrations show relatively orderly stacked alkane groups. Peculiarly, in 100% WC14 SAM, both ethanol and SAM spectral modes are positive. This behavior has been repeatedly observed in SAMs formed from pure WC14 and may be related to the reorientation of ethanol molecules, although the exact reason is unclear. Further studies are needed for clarification.

Other vibrational modes in the fingerprint region of mixed SAM, such as 1277, 1348, and 1466 $cm^{-1}$, are attributed to the twisting, waging, and scissoring vibrations of the WC14 methyl group, respectively. As discussed in part 4, the absorption band at 1140–1150 $cm^{-1}$ is attributed to the C–O–C group's characteristic asymmetric stretching vibrational mode, $\nu_{as}$(C–O–C).[98,189,195–202] Higher frequency and intensity of this peak in the WC14 spectrum shows more distinguished all-trans and amorphous structure than in mixed SAM and is usually observed in a non-hydrated environment.[226,227]

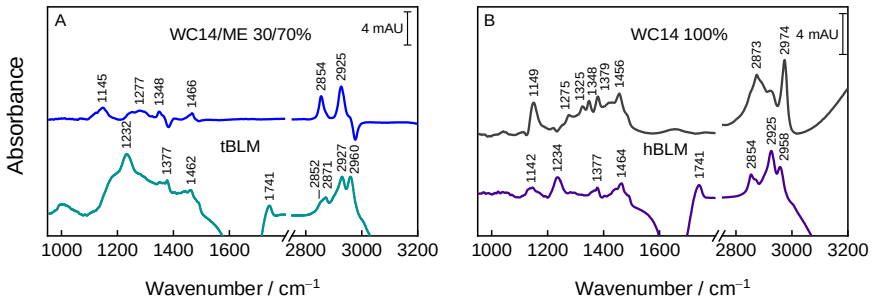


Figure 45. SEIRAS spectra of SAMs and bilayer lipid membranes on Au electrode. SAMs were formed from (A) WC14 and βME (30 and 70%) and (B) WC14 (100%). Lipid layers in tBLM and hBLM were formed from DOPC and cholesterol (60 and 40%).

Differences in tBLM and hBLM membrane structure can be noticed from the Figure 45 SEIRAS spectra (lower spectra in A and B, respectively). Asymmetrical $\nu_{as}(CH_2)$ vibrations of 2925 $cm^{-1}$ in hBLM show higher order than those in tBLM of 2927 $cm^{-1}$. Additionally, less defined bands in the fingerprint region of the tBLM spectral range also confirm more fluid membrane structure. Only $\nu_s(CH_2)$ spectral band at 2852 $cm^{-1}$ does not "comply", but it can be explained by poorly resolved low intensity shoulder near the symmetrical methyl group band.

Interestingly, C–O–C vibrations from SAM can be seen redshifted in hBLM to 1142 $cm^{-1}$ position. Two effects can explain it. Firstly, SAM is stretched even more due to interaction with DOPC, resulting in a higher PEG part order of the WC14 molecules, which agrees well with the higher relative intensity of $\nu_s(CH_2)$ and $\nu_{as}(CH_2)$ bands in comparison to $\nu_s(CH_3)$ and $\nu_{as}(CH_3)$. Secondly, the dismissal of water by the membrane reduces the solvation of EG chains.

Spectral bands at 1232–1234 $cm^{-1}$ are attributed to asymmetric stretching of a phosphate group, $\nu_{as}(PO^{2-})$.[96] Lower frequency at tBLM may indicate phosphate group interaction with water forming hydrogen bonds but is a somewhat speculative guess due to the small difference value. Carbonyl stretching is found at 1738–1741 $cm^{-1}$. It is affected by negative water bending vibrations at ~1645 $cm^{-1}$ in both systems. Additionally, broad feature related to O–H stretching in the 3000–3600 $cm^{-1}$ range are related to the water molecules removed from the interface during MLV fusion and subsequent tBLM formation.

## 5.3. SEIRAS probed water response to potential changes at gold interface

To evaluate water interaction in submembrane space, fully formed tBLM and hBLM systems on gold were introduced to potential changes ranging from 0.4 V to –0.8 V (vs. Ag/AgCl). The first spectrum obtained at 0.4 V was used as a reference (Figure 46). Only some minor changes are observed in both systems while potential decreases from 0.4 V to –0.4 V. Lowering potential further up to –0.8 V leads to a rapid increase of O–H stretching in 3000–3600 $cm^{-1}$ range for the tBLM system, indicating increase of water in submembrane space. On the contrary, C–H stretching vibrations in the 2850–3000 $cm^{-1}$ region decreases. This could be explained by the reduction of IR enhancement due to tBLM distancing caused by water induced submembrane layer thickening. Reversing potential to –0.4 V spectrum shows that the system returns to its previous state observed in the potential range from 0.4 to –0.4 V. Water O–H and alkane C–H negative bands almost disappear. Further shift to the positive potential up to the initial 0.4 V shows a decrease in water bands, indicating that more water leaves submembrane space compared to the initial tBLM system state.

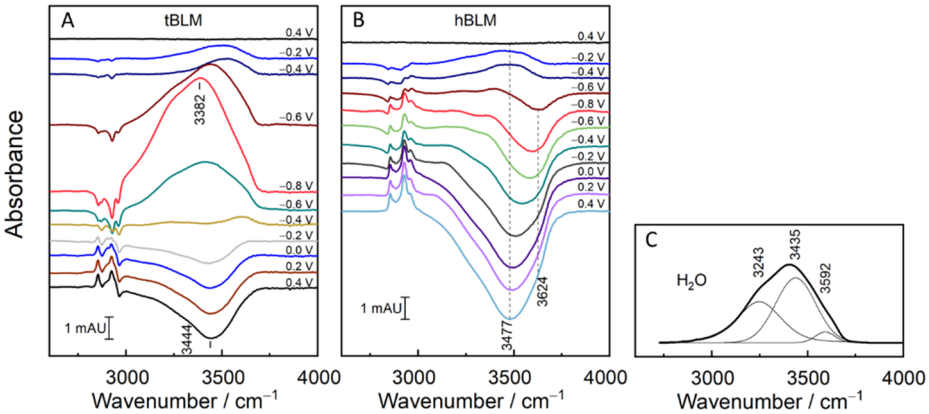


Figure 46. Potential dependent SEIRAS spectra of (A) tBLM and (B) hBLM in 0.1 M $Na_2SO_4$ and 0.05 M $NaH_2PO_4$ solution (pH 4.6). The potential window was from 0.4 to –0.8 V. (C) SEIRAS spectrum of $H_2O$.

Such an observation indicates that the membrane approaches the surface. The shift of the water band should be mentioned as well. The highest water band intensity was found at –0.8 V with the peak position at 3382 $cm^{-1}$, considerably redshifted compared to the spectrum at 0.4 V potential (3444 $cm^{-1}$). It can be concluded that from –0.4 V negative potential, more damages start appearing due to the membrane electroporation effect, and water is sequestrated inside the submembrane space, where it is involved in the internal hydrogen bonding network. By returning potential back to positive values,

excess of weaker bound water leaves the submembrane space. Thus, we observe a decrease in higher average energy (3444 $cm^{-1}$) peak intensity.

The effect of potential change is somewhat opposite for hBLM system. Its behavior is similar to the tBLM in the first stage until the –0.4 V potential is reached. A negative peak at 3624 $cm^{-1}$ starts appearing with a further decreasing potential, showing the loss of free water from the vicinity of the interface. Further potential decrease and reverse seem to influence even more water loss. Peak minimum at 3624 $cm^{-1}$ redshift to the 3477 $cm^{-1}$ showing that at first free water is lost and then followed by more H-bonded water. At the same time, intensity of stretching C–H vibrations of $CH_2$ and $CH_3$ groups in alkane chains increase. Overall, water loss during the potential expedition is higher for the hBLM system. At the same time, the tBLM system demonstrated water absorption capacity of a similar level (total water band intensity travel distance). It shows that submembrane space water is visible by the SEIRAS method.

## 5.4. SEIRAS probing of the dielectric constant

The importance of dielectric properties and the challenges associated with measuring them at the interface have already been established at the beginning of this chapter. As a result, the N-(6-mercapto)hexylpyridinium (MHP) compound (see in Figure 21) was incorporated into a self-assembled monolayer (SAM) composition at a ratio of 4:3:3 (MHP:WC14:βME). Previous work in our group demonstrated that this molecule is sensitive to changes in the dielectric environment and can be used as a vibrational marker.[228] It has been reported that the dielectric constant change is linear with regard to ratio of isopropanol and water solutions.[229] This feature can be linked/calibrated to a vibrational response, providing information for dielectric MHP surrounding the environment.

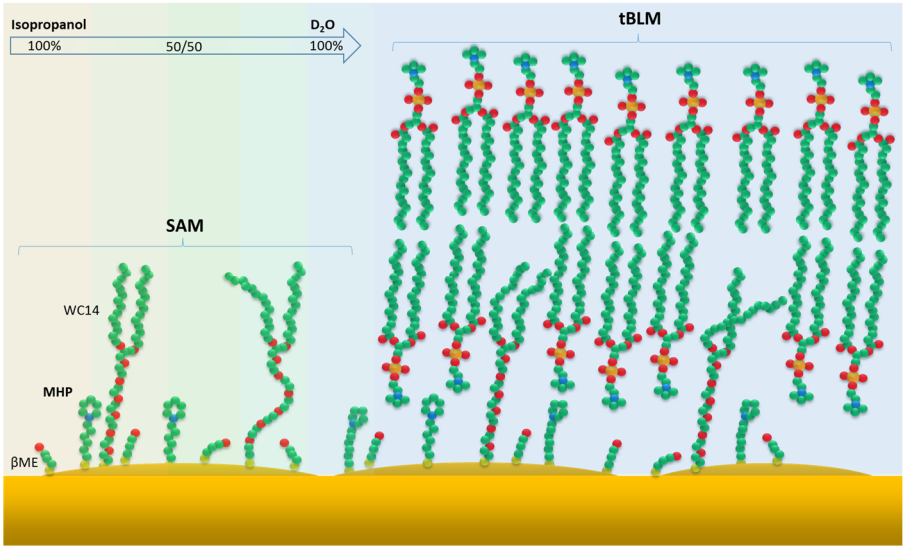


Figure 47. Schematics of MHP/WC14/βME SAM formed from Isopropanol (left side) interchanging into the tBLM system (right side).

The preparation of the SAM and tBLM is described in the methods section. A simple schematic of the experiment can be found in Figure 47. Firstly, mixed SAM was formed on the gold surface for over 60 minutes in an isopropanol-$d_6$ solution. Secondly, isopropanol-$d_6$ was gradually exchanged for $D_2O$. Finally, tBLM layer in $D_2O$ was formed. SEIRAS spectra were collected during all the steps.

The ATR-FTIR spectrum of solid MHP is shown in Figure 48A. Only a few available solid MHP spectral bands could be used for our initial purpose due to band overlapping, especially since MHP is mixed with WC14. This limitation primarily excludes the stretching and bending $CH_2$ vibrational bands of the aliphatic MHP chain, leaving only the vibrations from the pyridinium ring.

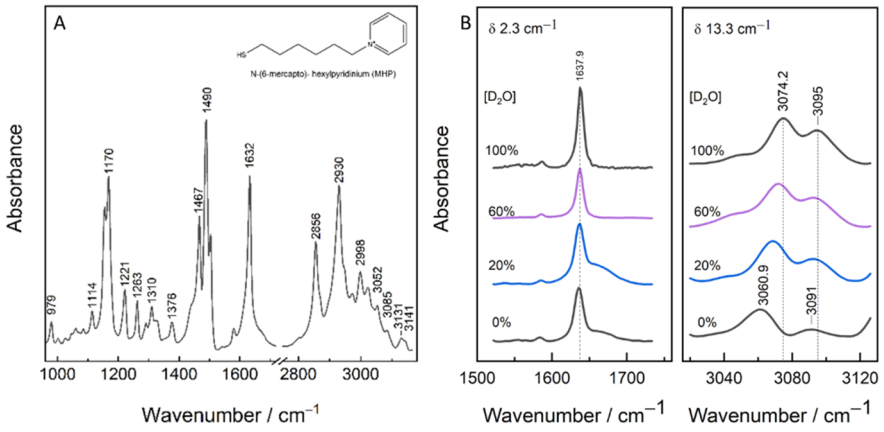


Figure 48. (A) ATR-FTIR spectrum of solid MHP. Transmission FTIR spectral regions of MHP in different ratio $D_2O$/Isopropanol-$d_6$ solutions.

To determine which spectral bands are most sensitive to dielectric environment changes, FTIR spectra of the MHP molecule were measured in solutions with varying isopropanol-$d_6$/$D_2O$ compositions. Three spectral bands were identified as responsive to changes in the solvent mixture by exhibiting frequency shifts (Figure 48B): the band at 1638 $cm^{-1}$ assigned to combination vibrations of ν(C2=C3) + ν(C6=C5) and the 3074 and 3095 $cm^{-1}$ band assigned to the stretching =C–H vibrations of the pyridinium ring.[228,230]

Unfortunately, the strong absorbance at 1638 $cm^{-1}$ demonstrated a relatively small band shift ($\delta = 2.3$ $cm^{-1}$) over the full solvent exchange range. However, one of the stretching =C–H vibrations exhibited a $\delta = 13.3$ $cm^{-1}$ increase as the solvent gradually changed from isopropanol-$d_6$ to $D_2O$. A similar SEIRAS experiment with MHP in the SAM revealed that the solution's impact shifted this band by $\delta = 7.1$ $cm^{-1}$ towards higher wavenumbers (Figure 49A).

Figure 49B compares the MHP stretching =C–H vibrational mode in the solution and the SAM, indicating a lower dielectric constant in the SAM layer's environment, with an estimated value of 30. This is likely due to a less hydrophilic environment, as MHP is surrounded by WC14 and βME-$d_4$. No changes in the MHP mode were detected upon the addition of a tBLM to the preformed SAM, suggesting that the additional membrane layer does not affect the MHP environment, as lipids are located further from the surface and do not interact with the deeper layer of the mixed SAM.

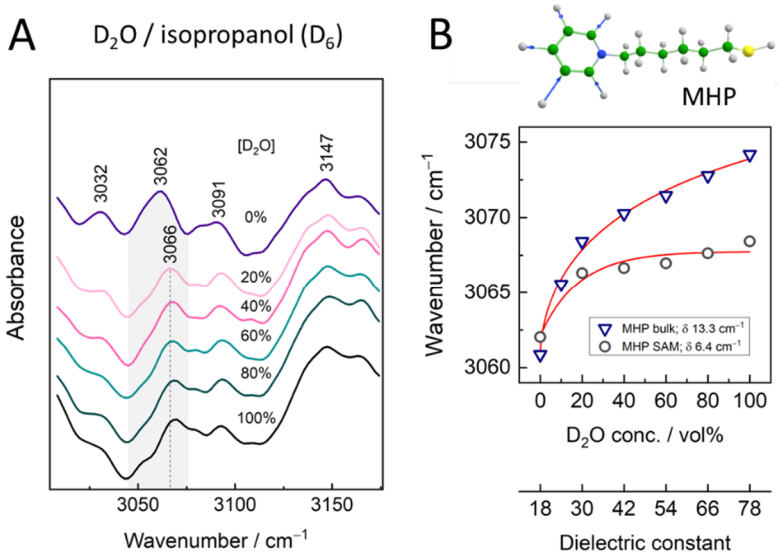


Figure 49. (A) SEIRAS spectra of SAM composed from WC14/ME/MHP (3/3/4) in solvent mixtures of $D_2O$ and isopropanol-$d_6$; (B) The dependency of MHP stretching =C–H mode's wavenumbers of the bulk molecule and incorporated in SAM on the solvent composition and its dielectric constant.

## 5.5. SEIRAS analysis of pH influence on tBLM

Tethered bilayer lipid membranes have gained significant traction in biosensor applications, especially when paired with electrochemical impedance spectroscopy (EIS). EIS is instrumental in monitoring membrane damage levels. However, its interpretations can sometimes be misleading due to its dependence on consistent dielectric conditions in the submembrane. In collaborative research, SEIRAS was employed to investigate the behavior of submembrane tBLM water. Our joined findings indicate that EIS signal reductions can be attributed to pH-mediated alterations in submembrane water properties rather than actual membrane damage.[231]

Figure 50 shows the SEIRAS spectra for tBLM in the 2830–3800 $cm^{-1}$ range. Within this range, specific modes of symmetric and asymmetric methylene stretching (located at 2856 and 2927 $cm^{-1}$) and asymmetric methyl stretching (2959 $cm^{-1}$) of the alkyl chain are observed. The pronounced negative peak near 3500 $cm^{-1}$ is attributed to the O–H stretching mode of water, which is displaced from the Au interface upon the formation of tBLM. When the tBLM is submerged in solutions with pH values of 4.5 and 7.3, consistent alterations in the volume of submembrane water are observed in the SEIRAS spectra. For a control measurement, the freshly formed tBLM was

extensively rinsed with a phosphate solution at pH 4.5, matching the pH of the multilayer vesicle solution. The rinsing displayed negligible influence on the SEIRAS spectra, as shown in Figure 50. However, altering the pH to 7.3 subsequently led to an increase in interfacial water, as indicated by a decrease in the intensity of the negative (O–H) mode. The consistency of this process is highlighted by the observed alterations in pH values between 4.5 and 7.3. Specifically, the absolute integral intensity drops to 81–84% at pH 7.3 and ascends to 91–93% when the pH is readjusted to 4.5. Thus, it can be inferred that transitioning the pH from 4.5 to 7.3 induces a significant rise in the sub-membrane water content.

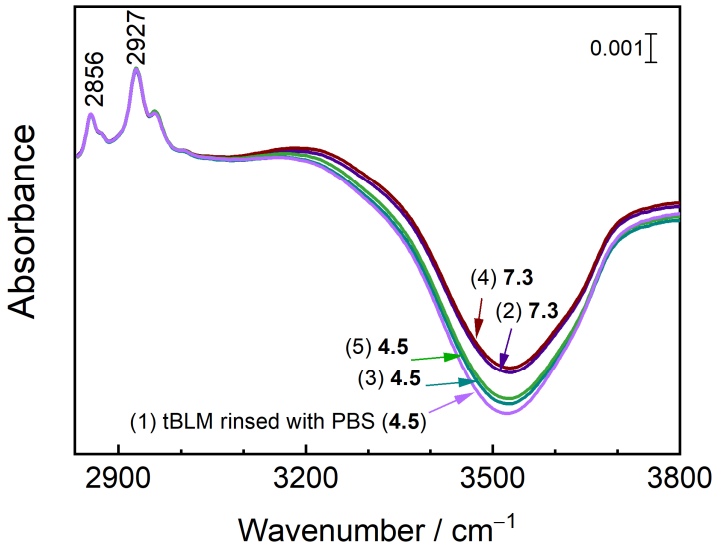


Figure 50. SEIRAS spectra of tBLM in the range of 2830–3800 $cm^{-1}$. Sequential pH exchange between 4.5 and 7.3 are marked (1–5). Spectrum of water on gold is used as a reference. Intensities were normalized according to the asymmetric stretching mode of methylene at 2927 $cm^{-1}$.

A more in-depth examination of the processes can be observed in Figure 51. Here, SEIRAS spectra at different pH levels are presented using the fully formed tBLM spectra as the reference baseline. Apparent changes can be observed when transitioning from pH 7.3 back to pH 4.5.

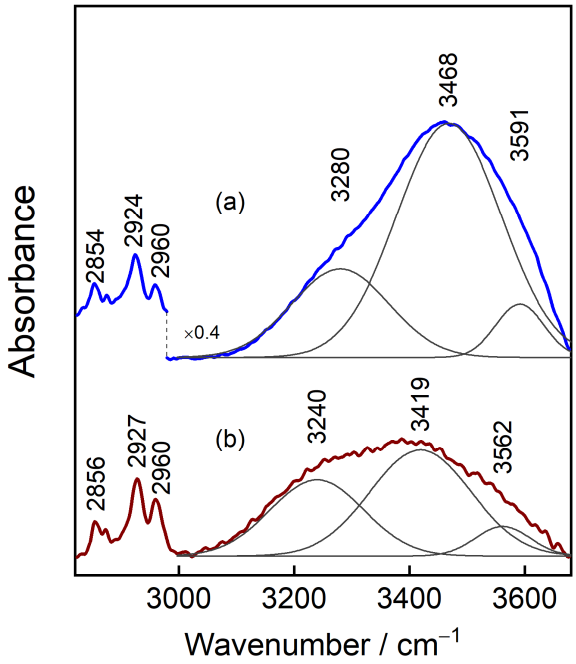


Figure 51. SEIRAS spectra of tBLM exposed to pH 7.3 (a) and then to 4.5 solutions (b). The reference spectrum was as-formed tBLM membrane in pH 4.5 phosphate solution.

Following the immediate shift to pH 7.3, disturbances are evident in the C–H and O–H stretching regions. These changes signal an increase in sub-membrane water volume and a reorientation of molecules within the organic layer. The upward trends in methylene stretching vibrational modes suggest a tilting of carbohydrate chains relative to the surface normal. However, attributing these changes to specific components, whether anchoring or lipid layer, is indeterminate. When exposed to the pH 7.3 solution, both methylene stretching modes experienced a redshift of 2–3 $cm^{-1}$, moving to 2854 and 2924 $cm^{-1}$ compared to the initial tBLM as shown in Figure 50.

In Figure 51a, an upward-facing O–H stretching mode suggests an increased water presence within the tBLM structure at pH 7.3, contrasting with tBLMs in a more acidic environment of pH 4.5, as shown in Figure 51b. The O–H spectral mode shape can be deconvoluted into three components characterized by a Gaussian-Lorentzian. Two components at the lower frequencies, specifically at 3250 and 3400 $cm^{-1}$, were identified as "network water". The 3250 $cm^{-1}$ component corresponds to a structured network of strongly hydrogen-bonded water molecules, while the more pronounced 3400 $cm^{-1}$ component aligns with a liquid water state. The "multimer water", which

refers to water molecules that form a disrupted hydrogen-bond network, may be associated with the spectral component apparent at 3600 $cm^{-1}$.[214,215,218,219] The positive intensity and shape of the OH mode at pH 4.5 suggest incomplete recovery from structural modifications after the tBLM's exposure to pH 7.3.

For quantitative analysis, integral intensity ratios $R_{network}$ and $R_{multimer}$ were calculated (Table 5). While $R_{network}$ represents a concentration of tightly interconnected water molecules, $R_{multimer}$ is related to a water network with weakened hydrogen bonds.[95] For comparison, bulk water was measured on pristine silicon ATR crystal (Table 5). The SEIRAS findings at pH 7.3 highlight an influx of water to the submembrane, characterized by an enlarged proportion of multimer water and a relatively reduced amount of network water compared to the ATR spectrum of bulk water. Furthermore, a close examination of peak positions revealed a significant upshift up to 64 $cm^{-1}$, indicating a reduction in hydrogen bonding interactions among water molecules adjacent to the lipid membrane. A return to pH 4.5 drastically reduced the water content within the tBLM, yet an excess remained compared to the originally formulated tBLM. One might attribute the positive bulk-like water mode to the thinning of the lipid bilayer. However, past research has shown a minimal correlation between pH levels and variations in lipid layer thickness.[232,233]

Table 5. Frequencies of the O–H stretching modes and proportional network and multimer water distributions.

| No | pH | Wavenumber / $cm^{-1}$ | | | $R_{network} = \frac{A_{3250}}{A_{3400}}$ | $R_{multimer} = \frac{A_{3600}}{A_{3250} + A_{3400}}$ |
|---|---|---|---|---|---|---|
| 1 | 7.3 | 3280 | 3468 | 3591 | 0.35 | 0.08 |
| 2 | 4.5 | 3240 | 3419 | 3562 | 0.66 | 0.09 |
| 3 | 7.3 | 3276 | 3467 | 3593 | 0.43 | 0.08 |
| 4 | 4.5 | 3242 | 3414 | 3553 | 0.85 | 0.16 |
| Si \| $H_2O$ | | 3224 | 3404 | 3585 | 0.74 | 0.03 |

The SEIRAS findings indicate a significant augmentation in water content within the sub-membrane and/or bilayer regions when transitioning the solution pH from 4.5 to 7.3. This additional water predominantly displays an elevated proportion of the multimer fraction compared to the network fraction. Such a pattern could be attributed to the prevailing influence of solvated ions. Moving the pH from 4.5 to 7.3 could result in a heightened concentration of solvated ions in the sub-membrane region. This would, in turn, reduce the specific resistance of the sub-membrane, manifesting as an

upward shift in the admittance phase minimum, as documented by the EIS measurements in the collaboratively published work.[231]

In conclusion, the SEIRA spectroscopy data indicate that ion content is the primary physical factor behind the variation in submembrane resistivity. As the pH shifts from acidic to neutral, there's a surge in ion concentration in the submembrane. This results in an increase in specific conductance and a corresponding decrease in specific resistance within that region. The exact mechanism driving this change remains somewhat ambiguous. Still, the protonation of lipid head groups and the subsequent alteration in the charge equilibrium of the constrained area could be the key contributors.

## 5.6. Interim conclusions

In conclusion, the experiments in this study provided valuable insight into the formation and behavior of tBLM and hBLM systems formed on mixed and a single component WC14 SAMs. The SEIRAS spectra revealed key molecular arrangement and fluidity differences between the two systems. Specifically, asymmetrical $\nu_{as}(CH_2)$ vibrations at 2925 $cm^{-1}$ in hBLM demonstrated higher order than those in tBLM at 2927 $cm^{-1}$. Moreover, the fingerprint region of the tBLM spectral range confirmed its more fluid membrane structure. Deuterated phospholipids and cholesterol provided clearer differentiation between the SAM and membrane signals, facilitating a more accurate analysis of the lipid bilayer's formation and behavior.

The potential-dependent behavior of interfacial water for both tBLM and hBLM systems was explored, showing that water content could be modulated by applying different potentials. Starting from –0.4 V and going to the more negative potentials, the tBLM system exhibited increased sub-membrane water content, while the hBLM system experienced decreased interfacial water. The return to positive potentials resulted in weaker hydrogen-bound water removal from the tBLM submembrane and further water removal in the hBLM system. Interestingly, both systems showed similar capacity of water involved in potential range experiments.

Furthermore, the incorporation of MHP into the SAM composition allowed for the investigation of the dielectric environment in the SAM layer through SEIRAS measurements. It was demonstrated that stretching =C–H vibrations from the pyridinium ring exhibit the biggest frequency changes in different dielectric constant environments in bulk solutions ($\delta$ = 13.3 $cm^{-1}$) as well as at the interface ($\delta$ = 7.1 $cm^{-1}$). It was measured that the environment within the SAM layer was less hydrophilic compared to the solvent mixture, with an approximate dielectric constant value of 30. It was also observed that

a tBLM did not significantly alter the MHP environment, as lipids were situated further away from the surface and did not interact with the deeper layer of the mixed SAM. Therefore, effective use of MHP is somehow limited to its immediate surroundings.

Finally, it was shown that SEIRAS indicates a substantial rise in water content within the sub-membrane space and/or bilayer region when the pH shifts from acidic to basic. It was proposed that this heightened water content in the confined area between the electrode and the bilayer indicates a surge in the concentration of hydrated charge carriers. This phenomenon may correspond to an enhanced dielectric constant of the submembrane at increased pH levels.

Overall, these findings contribute to a deeper understanding of the behavior and interactions of tBLM and hBLM systems and the influence of submembrane water and applied potential on membrane properties. Additionally, the use of SEIRAS as a powerful tool for investigating the submembrane environment and its response to potential changes was demonstrated, which can aid future studies in this field.

# 6. IN SITU MONITORING OF MELITTIN INCORPORATION INTO THE PHOSPHOLIPID BILAYER MEMBRANE

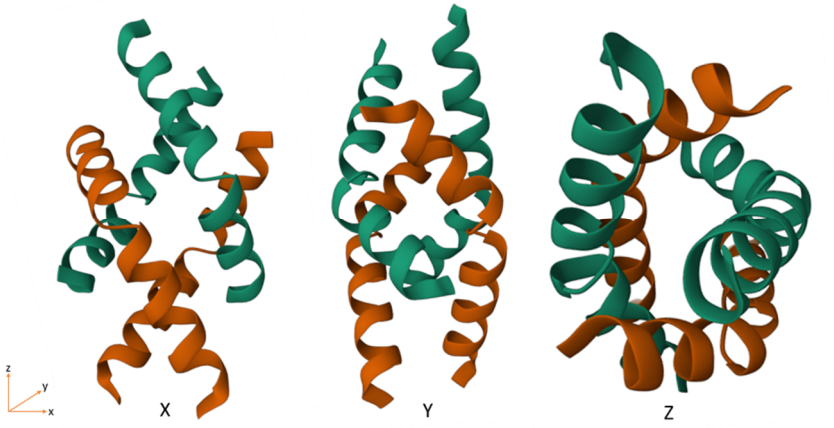


PDB: 2MLT

https://doi.org/10.2210/pdb2MLT/pdb

## 6.1. Introduction

Melittin (Figure 52) is a small antimicrobial peptide (AMP) that is the main component of bee venom. AMPs are known to create toroidal pores in lipid membranes and act as a defense mechanism for many organisms.[119,234,235] AMPs are defined as small peptides in the range of 12 to 60 amino acids that can take on various structural conformations such as helical, β-sheet, cyclic, globular, and others. Despite the structural variations, they are all described as cationic, amphipathic peptides with a broad spectrum of microbicidal activity linked to membrane permeabilization.[115] Although a large body of research has been devoted to studying AMPs, the mechanism of action of how they work remains poorly understood, and the interpretation of experimental results is a topic of ongoing discussion.[115,236,237]

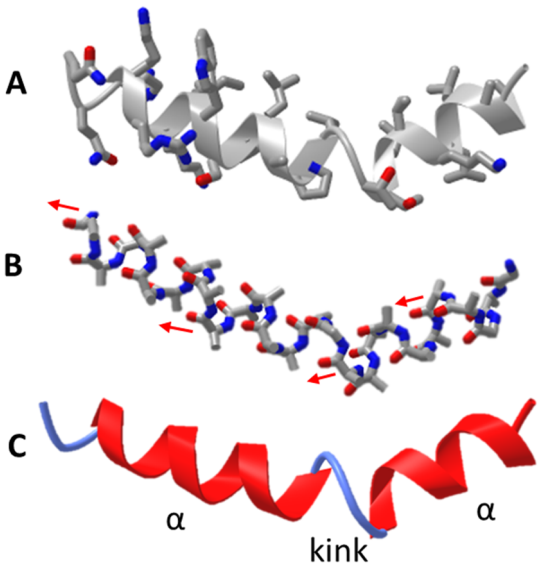


Figure 52. Melittin structure view as a ribbon with side chains (A), the backbone of a peptide chain (B), and only ribbon structure (C). Nitrogen and oxygen atoms are colored blue and red, respectively. Red arrows in B show the direction of TDM for stretching C=O vibrations (Am-I) (PDB: 2MLT).

Melittin provides a good example of an AMP class peptide to study membrane permeation processes and factors affecting them. A two-phase process explains its mechanism of action.[238] Firstly, it assumes a kink-separated two α-helix conformation structure[234] (Figure 52C) from a rather disordered one[239] by binding to the membrane, with its helical axis parallel to the membrane surface and entering the so-called S (surface) state. As more peptides adsorb to the surface, the peptide-to-lipid ratio changes and melittin

reorients by entering the membrane and forming toroidal pores - T state. This reorientation drastically changes the TDM vector direction of amide bonds (Am-I and Am-II) (Figure 52B), which can be informative in studying such transformations by infrared techniques, such as IRRAS, PM-IRRAS, or SEIRAS.

To monitor and compare melittin insertion into the membrane, a system from DOPC and cholesterol was constructed to assemble into hBLM and tBLM to monitor the process in situ by the ATR-SEIRAS method. Schematic representations of both hBLM and tBLM are presented in Figure 16. The main idea was to survey and compare melittin's interaction with more biological membrane mimicking systems in tBLM's case with a more restricted hBLM construct, having a more stable and ordered structure and, therefore, more rigid and difficult to penetrate. The main distinction between both systems is the presence of a water layer between SAM and BLM. In a collaborative project to study melittin insertion into the membrane, SEIRAS method was employed as complementary alongside other techniques, such as spectroscopic ellipsometry (SE) in total internal reflection configuration and electrochemical impedance spectroscopy (EIS).

### 6.1.1. Melittin-membrane interaction probed by SEIRAS

To investigate how melittin interacts with the hydrophobic core of a membrane, SEIRAS experiments were performed using tBLM and hBLM systems. The SEIRAS spectra were recorded at different time intervals from the injection of melittin (final concentration being 1.75 μM) to the 120-minute limit. The summarized spectral results for melittin interaction with tBLM and hBLM are presented in Figure 53a,b.

Information on alterations in the submembrane space during the interaction between melittin and lipid membranes can be obtained from the O–H stretching vibrations region at 3000–3700 $cm^{-1}$, which can be separated into different water states. The band at 3600 $cm^{-1}$ is attributed to the "multimer water" network of disrupted hydrogen bonds. In this state, water molecules are not strongly bonded to one another, and the network of hydrogen bonds is disrupted. The mode at 3400 $cm^{-1}$ is assigned to liquid water, where water molecules are more closely packed, and hydrogen bonds are stronger. Finally, the band at 3250 $cm^{-1}$ is assigned to an ice-like water state, where the hydrogen bonds are even stronger than in liquid water, leading to a slightly lower frequency and sharper absorption band in the IR spectrum.[214,215,218,219]

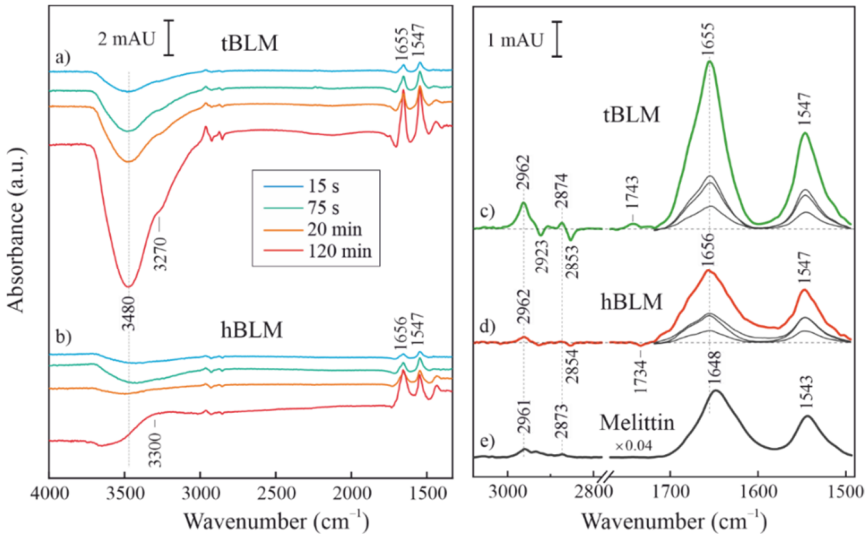


Figure 53. SEIRAS difference spectra of melittin after 15 s, 75 s, 20 min, and 120 min incubation time with tBLM and hBLM membranes. Difference spectra were constructed by taking membrane spectrum (either tBLM or hBLM) as a reference. Left: a) tBLM and b) hBLM membranes without correcting $H_2O$ contribution; right: c) tBLM and d) hBLM membranes with subtracted $H_2O$ spectral contribution. ATR-FTIR spectrum in e) shows the spectral features of the melittin in $H_2O$ solution.

The alterations observed in water structure are attributed to the various lipid membrane topologies and melittin activities. Within 15 seconds of melittin injection, a reduction in the water band centered at 3480 $cm^{-1}$ is seen for both membranes, indicating disruption of the water structure. With longer incubation durations, this disruption is more apparent in tBLM. The removal of water molecules from the vicinity of the gold surface and subsequent shortening of WC14 PEG segment chains suggest an increase of melittin molecules in the submembrane space. Notably, the reduction of the ice-like water band in tBLM indicates that the confined or strongly hydrogen-bonded water is disturbed by the presence of melittin in the submembrane space.

In the 1800–1500 $cm^{-1}$ region, melittin introduction reveals Amide I (Am I) and Amide II (Am II) bands centered at 1655 $cm^{-1}$ and 1547 $cm^{-1}$, respectively, for both tBLM (Figure 53c) and hBLM (Figure 53d) systems. The concentrated melittin aqueous solution ATR-FTIR spectrum (Figure 53e) indicates absorption bands for the relevant amide moieties at 1648 $cm^{-1}$ and 1543 $cm^{-1}$. Protein secondary structure information can be inferred using the Am I mode. It is known that melittin mainly adopts a disordered form in diluted aqueous solutions, with predicted absorption at somewhat lower wavenumbers, about 1648 $cm^{-1}$, than that of the α-helix close to 1656 $cm^{-1}$.[239–242] When comparing the SEIRAS spectra in Figure 53c to the melittin solution

ATR-FTIR spectrum (Figure 53d), a change can be seen in the Am I position. The interaction with the lipid-membrane causes the α-helical secondary structure of melittin, which is demonstrated by the frequency increase of 7–8 $cm^{-1}$.

In the region of 3000–2800 $cm^{-1}$, it is easy to observe melittin-induced structural alterations for tBLM and hBLM membranes (Figure 53c and d). The positive bands at 2962 $cm^{-1}$ and 2874 $cm^{-1}$ are associated with the asymmetric and symmetric methyl vibrations, $\nu_{as}(CH_3)$ and $\nu_{s}(CH_3)$, respectively, while the negative bands at 2923 $cm^{-1}$ and 2853 $cm^{-1}$ are associated with the asymmetric and symmetric methylene vibrations, $\nu_{as}(CH_2)$ and $\nu_{s}(CH_2)$ respectively.[172,204] These spectrum variations are caused by the changes in molecule orientation at the surface due to the surface selection rule.[39] The negative bands at 2923 $cm^{-1}$ and 2853 $cm^{-1}$ indicate that the transition dipole moments of the methylene groups of SAM molecules acquire an orientation somewhat more vertical to the surface. The bands are assigned to the SAM alkane chains, ignoring lipids due to exponential SEIRAS signal damping with the increasing distance from the surface.[243] Melittin is the source of the positive $\nu_{as}(CH_3)$ mode, as evident from the ATR-FTIR spectrum of the melittin solution. Furthermore, the tBLM spectrum shows higher intensity $\nu_{as}(CH_3)$ stretching modes relative to amide I than in bulk melittin ATR-FTIR data, demonstrating melittin's preference for the horizontal orientation.

Am I and Am II transition dipole moments are perpendicular[244], and changes in their relative intensities, given as the intensity ratio Am-I/Am-II, readily reflect the orientation of peptides with respect to the surface. The ATR-FTIR spectra of melittin in solution show an intensity ratio of 1.3 for the disordered structure (Figure 53e). In Figure 54a, the progression of the Am-I/Am-II ratio over time reveals different melittin interactions with hBLM and tBLM. For hBLM, the ratio of around 1.0 remains constant over the course of 100 min, indicating that melittin is mainly adsorbed lying horizontally on the lipid bilayer. On the other hand, the initial ratio of 1.3 for tBLM suggests a higher proportion of melittin molecules have their α-helices aligned with the surface normal due to tBLM's naturally occurring defects. Earlier research has shown that melittin's interaction with dimyristoylphosphatidylcholine (DMPC) vesicles in water for one hour resulted in an Am-I/Am-II ratio of 1.3.[245] While the ratio of around 1.3 indicates the existence of random melittin orientation, the same ratio in tBLM suggests the presence of transmembrane melittin orientation.

Even though the overall intensity of the amide bands gets stronger over time, a prolonged unvarying ratio lasting for about 90 minutes may signal a

gradual buildup of melittin in the submembrane space, resulting in a greater signal for the Am II bands. The last step, beginning at 90 minutes, points to the formation of lipid-peptide aggregates. Similar behavior is observed for the hBLM, with the amide I band showing a slight increase in intensity with respect to Am II.

Figure 54b shows an initial interaction of melittin with the membrane in the form of the integral ratio $A_{\nu(OH)}/A_{Am\text{-}II}$, indicating the expulsion of water molecules from the lipid-solvent interface by melittin (increase in Am II intensity) since the absolute intensity of ν(OH) has been used in the ratio. The water loss effect is evident for both membrane types.

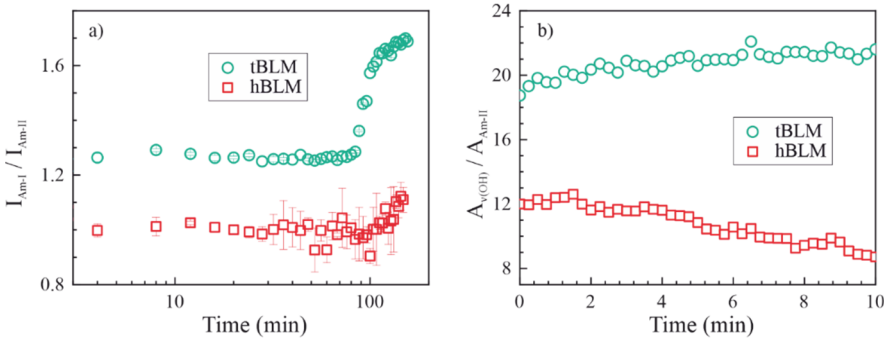


Figure 54. a) Melittin's Am-I/Am-II intensity ratio changes over time as it interacts with tBLM and hBLM. Water's spectral contribution has been subtracted. The image displays error bars with a 90% reliability correlation. b) Time-dependent evolution of the ν(OH)/Am-II ratio calculated from absolute integral intensities.

## 6.2. Interim conclusions

SEIRAS data provide clear evidence of membrane disturbance following the introduction of melittin. Both the hBLM and tBLM systems exhibited a decrease in water content within the first 15 seconds, with the tBLM system showing greater water expulsion and accumulation of melittin molecules in the submembrane space over longer incubation times. The shortening of the ethylene oxide chain segment of WC14 supports this. The strongly hydrogen-bonded water band in tBLM also decreased, indicating water network disturbances after melittin introduction into the submembrane space. The negative bands at 2923 $cm^{-1}$ and 2853 $cm^{-1}$ are associated chiefly with alkane chains of WC14. They indicate orientation changes in the hydrophobic part of SAM molecules into a more vertical alignment due to TDMs of methylene lining up with the surface normal, resulting in a thinner layer. The methylene bands are assigned to SAM because SEIRAS prioritizes proximal alkane chains of SAM rather than the distal lipid layer.[243]

In the hBLM system, thinning can be attributed only to the WC14 chain segment shortening and outer leaflet but not the inner leaflet. The initial SEIRAS spectra show water expulsion from the vicinity of the gold surface, but it is less effective than in the tBLM case, as the ratio of ν(OH)/Am-II is almost twice lower in hBLM (Figure 54b). Water removal in tBLM increases with time as melittin accumulates in natural membrane defects and the submembrane region. For hBLM, melittin initially interacts with the outer layer of the lipid membrane, followed by a decrease in the ratio after a couple of minutes, suggesting that water removal from the surface is caused by the aggregation of peptides at the membrane's surface. This behavior is very similar to what has been described by Juhaniewicz and Sek in the supported membrane system, showing that melittin primarily acts in the submembrane space.[246] In the longer incubation times above 90 minutes, for both hBLM and tBLM systems, aggregation of melittin with lipids occurs, leading to membrane destruction. These findings support a detailed characterization of melittin interaction with the bilayer membrane using other synergetic techniques.

# CONCLUSIONS

1. ATR-SEIRAS measurements revealed that SAM formed from 100% IMHA molecules forms a less ordered organic layer than the bimolecular IMHA/fragment SAMs due to geometric constrictions from the bulky imidazole ring. This leads to engagement of amide groups in suboptimal hydrogen-bonding network.
2. Measurements under controlled potential conditions from 0.3 to –0.5 V vs. Ag/AgCl electrode have shown that imidazole ring's stretching vibrations (=C–H) at 3115 and 3150 $cm^{-1}$ reversibly downshift with frequency tuning rates of –10.4 and –6.3 $cm^{-1}V^{-1}$ towards more negative potentials. A decrease in frequency has been linked to the weakening hydrogen bonding strength of Im and the adjacent water.
3. ATR-SEIRAS revealed that anchoring SAM formed from WC14 and βME molecules is amorphous at ethylene glycol chains and disordered at the alkyl chains, providing the necessary flexibility required for the tBLM formation. tBLM forms in two stages. Firstly, lipid vesicles adsorb onto anchoring SAM and replace interfacial water molecules. Secondly, vesicles cast on a surface plane and form planar lipid bilayer, which interacts with the WC14 alkyl chains to form stable tBLM in approximately 60 minutes.
4. For the first time water structure in the inner layer of the tBLM was probed by the SEIRAS technique, showing submembrane water increase at the negative polarization below –0.4 V (vs. Ag/AgCl) and release of less hydrogen-bound water by returning potential to the positive value.
5. By using N-(6-mercapto)hexylpyridinium molecule as SEIRAS probe, we were able to determined dielectric constants withing the anchoring SAM layer and the tBLM submembrane reservoir, which were approximately 30.
6. The SEIRA spectroscopy data showed that ion content is the primary physical factor behind the variation in submembrane resistivity. As the pH shifts from acidic to neutral, there's a surge in water and ions in the submembrane.
7. SEIRAS experimental data of melittin interaction with model membranes confirmed transition in melittin structure from unordered to α-helix at the timescale less than 15 s. At longer incubation, melittin accumulation in submembrane space follows, exchanging the interfacial water. SEIRAS comparison data from hBLM and tBLM experiments have shown almost two times higher total water expulsion from the vicinity of the gold surface at the interaction of membranes with melittin.

# SANTRAUKA

## Įvadas

Paviršius ir fazių riba labai svarbūs visiems gyvybę palaikantiems procesams, pradedant vandens kondensacija ir baigiant sudėtingomis biomolekulių sąveikomis katalizėje, energijos transformavime arba elektronų perdavime per lipidų membraną. Pagrįsta manyti, jog vienas iš pagrindinių veiksnių, padėjusių "pagreitinti" pirmųjų savireplikuojančių molekulių atsiradimą buvo būtent fazių riba. Ko pasekoje, kompleksiniai molekuliniai dariniai evoliucionavo į šiandien žinomas gyvybės formas.[2] Šia tema atliekama daug tyrimų. Dauguma jų, viena ar kita forma, susiję su reiškiniais fazių riboje, ir jų spektras yra labai platus: pradedant nuo paviršiaus įtampos poveikio[3] iki ląstelių membranos tyrimų.[4] Sąveikos struktūriškai tvarkinguose molekuliniuose sluoksniuose, pavyzdžiui, savitvarkiuose monosluoksniuose (SAM) arba fosfolipidų membranose yra gerai žinomos ir dokumentuotos. Visgi, svarbu suprasti, kad molekulių savybės fazių riboje yra kitokios nei tirpaluose ar kietame būvyje, todėl turimos žinios apie molekulių savybes tūryje negali gali būti tiesiogiai pritaikomos paviršiuje adsorbuotoms molekulėms. Dėl poreikio tirti fazių riboje vykstančius procesus buvo sukurta daug modernių eksperimentinių metodų. Tarp jų verta paminėti atominės jėgos ir elektronų mikroskopiją, masių spektrometriją, neutronų bei rentgeno spindulių technikas, mikrofluidiką ir optinę spektrometriją.[5] Optiniai metodai, ypač veikiantys matomojo ir infraraudonųjų spindulių srityse, dažnai naudojami biomolekulėms tirti. Pritaikytos paviršiaus tyrimams, šiuolaikinės optinės spektroskopijos technikos suteikia galimybę labai jautriai stebėti biomolekulių sąveiką fazių riboje. Vienas tokių metodų yra **paviršiaus stiprinta infraraudonųjų spindulių sugerties spektroskopija** - SEIRAS. Metodas žinomas jau daugiau nei dvidešimt metų, tačiau pradėtas taikyti biologinių membranų ir baltymų tyrimuose tik pastarąjį dešimtmetį.[6] Be to, SEIRAS yra vienas iš nedaugelio metodų, leidžiančių tiesiogiai stebėti vandens molekulių pokyčius. Kartu su in situ SAM ir lipidinių membranų tyrimais, SEIRAS tampa itin vertingu įrankiu tokiems moksliniams tyrimams.

Šiame darbe buvo taikyti įvairūs metodai. ATR-SEIRAS metodas buvo naudojamas kaip pagrindinis optinės spektrometrijos įrankis, naudojamas kartu su potenciometrija bei pagrindiniu aukso dangos ant silicio elektrodu. Įprastinė infraraudonųjų spindulių (IR) spektrometrija, pralaidumo ar ATR konfiguracijoje, naudota grynų medžiagų spektrų gavimui. Be to, izotopų pakeitimo technika, skenuojančioji elektronų mikroskopija ir kvantinio

modeliavimo (DFT) metodai buvo taikyti kaip papildomos technikos, svarbios vibracinės spektroskopijos duomenų išaiškinimui.

Šiuo darbu buvo siekiama ištirti savitvarkių monosluoksnių bei modelinių lipidinių membranų formavimąsi, struktūrą ir sąveikas fazių riboje. Tyrinėjome jų sąveiką su poras formuojančiu baltymu, jų tarpusavio ir aplinkos sąlygotas reakcijas. Ar SEIRAS matavimais in situ galime stebėti šiuos procesus? Ar elektrinio potencialo pokyčiai aukso paviršiuje veikia susidariusių sluoksnius ir ar galima juos kontroliuoti? Tai tik keletas keliamų klausimų, siekiant geriau suprasti biologiškai aktualių modelinių membranų susidarymą ir jų sąveiką su supančia aplinka.

**Darbo tikslas.** Šiuo darbu buvo siekiama ištirti SAM struktūrinius pokyčius, modelines dvisluoksnio lipidų membranas (BLM) ir jų sąveiką su poras membranoje formuojančiu toksino baltymu melitinu in situ, panaudojant SEIRAS metodą.

**Darbo uždaviniai:**

1. Suformuoti ir charakterizuoti savitvarkius monosluoknius, sudarytus iš imidazolio žiedo galinę funkcinę grupę turinčių IMHA ir/arba fragmento molekulių, panaudojant ATR-SEIRAS.
2. Ištirti, kaip vandeniliniai ryšiai bei potencialo pokyčiai fazių riboje įtakoja savitvarkius monosluoksnius formuojančias molekules turinčias imidazolo galinę grupę.
3. Ištirti inkarinių savitvarkių monosluoksnių bei jų mišinių formavimąsi aukso paviršiuje bei pakabinamų dvisluoksnių lipidinių membranų susidarymą.
4. Ištirti vandens struktūros pokyčius fazių riboje prie pakabinamos ir hibridinės lipidinių membranų (tBLM ir hBLM) dėl potencialo poveikio.
5. Nustatyti dielektrinę konstantą pomembraniniame tBLM rezervuare panaudojant molekulinį žymenį.
6. Ištirti pH pokyčių įtaką tBLM.
7. ATR-SEIRAS metodu in situ palyginti poras formuojančio baltymo melitino sąveiką su tBLM ir hBLM membranomis.

**Darbo naujumas:**

Esminis histidino vaidmuo baltymų struktūroje ir jų katalizinėje funkcijoje priskiriamas jo šoninei grupei, imidazolo žiedui (Im).[7] Im dalyvauja aromatinėje ir vandenilinių ryšių sąveikoje bei gali koordinuoti metalų (II) katijonus per laisvą azoto atomo elektronų porą.[8] Vandeniliniai ryšiai labai dažnai stebimi ties poliniais paviršiais. Nepaisant šių ryšių didelės

biologinės svarbos, eksperimentinis vandenilinių ryšių pokyčių stebėjimas elektrocheminiame paviršiuje yra labai sudėtingas dėl riboto metodų pasirinkimo. Pasinaudojus elektrocheminiu ATR-SEIRAS, pirmą kartą tirtas imidazolo žiedo (Im) vandenilio ryšio sąveikos stiprumas su aplinka fazių riboje Au-vanduo. Be to, buvo tiriama Im turinčių molekulių adsorbcija ir savaiminis išsidėstymas ant Au paviršiaus. Parodytas ryšys tarp Im turinčių alkantiolių molekulių koncentracijos paviršiuje ir Im orientacijos. Pademonstruota, kad monosluosniui sudarytam iš Im turinčių molekulių, didelis žiedas trukdo formuoti optimalų išsidėstymą, taip pat lėtinamas monosluoksnio formavimasis. Nustatyta, kad Im grupės =C–H virpesiai yra jautrūs vandenilio ryšio stiprumui, o tarp Im ir vandens vandenilio ryšio sąveikos stiprumas grįžtamai priklauso nuo išorinio elektrinio lauko. Elektrinio potencialo pasikeitimas į neigiamą susietas su grįžtamais Im orientacijos pokyčiais, matomais dviejų Im =C–H virpesinių juostų 3150/3115 $cm^{-1}$ santykinio intensyvumo pokyčiu.

Vandens molekulės paviršiuose ir pomembraniniame sluoksnyje gali paveikti SAM ir BLM adsorbciją, jų tvarkingumą ir stabilumą bei jų sąveiką su kitomis biomolekulėmis.[9,10] Tačiau, net panaudojant moderniausius šiuolaikinius metodus, tiesioginis vandens dielektrinių savybių stebėjimas plonuose paviršių sluoksniuose išlieka labai sudėtingas. Šiame darbe ATR-SEIRAS metodu buvo tiriama pomembraninio tBLM vandens struktūra bei potencialo sąlygojamas jos kitimas. Taip pat buvo tiriamas vandens dalyvavimas modelinių membranų formavime bei potencialo pokyčių poveikis jau suformuotoms BLM. Spektrometrinis žymuo buvo panaudotas paviršinio bei pomembraninio vandens dielektrinės skvarbos išmatavimui. Be to, buvo parodyta, jog pH pasikeitimų įtakoti pomembraninės savitosios varžos pokyčiai tBLM sistemoje yra susijęs su jonų koncentracijos pokyčiais, o ne su membranos vientisumo pakeitimais.

ATR-SEIRAS metodas panaudotas modelinės pakabinamos dvisluoksnės fosfolipidinės membranos formavimuisi tirti ant SAM sudaryto iš WC14 bei βME junginių mišinio. Nustatyta, jog membrana formuojasi dviem etapais, pirmiausia adsorbuojantis fosfolipidams nustumiamas vanduo. Po ko seka membranos formavimasis jai sąveikaujant su SAM. Duomenys panaudoti poras formuojančio toksino melitino ir dviejų skirtingos architektūros biomimetinių lipidų membranų (tBLM ir hBLM) sąveikai tirti in situ. Identifikuotos dvi skirtingos baltymo-lipido sąveikos elgsenos priklausomos nuo dvisluoksnės lipidinės membranos struktūros. Parodyta, kad toksino kaupimasis prie membranos pradiniame etape veikia jos struktūrą bei yra atsakingas už vandens išstūmimą abejose sistemos (hBLM ir tBLM). Tai sukelia struktūrinius pokyčius SAM sluoksniuose, dėl ko jie tampa

plonesni. Melitino sąveikos su skirtingomis membranų sistemomis eksperimentais patvirtintas peptidų kaupimasis pomembraninėje erdvėje vėlesnėje stadijoje. Po 90 min inkubacijos membrana suardoma dėl melitino agregacijos su lipidais.

**Ginamieji teiginiai:**

1. Imidazolio žiedo grupė trukdo susiformuoti IMHA monosluoksniams bei veikia monosluoksnio formavimosi dinamiką.
2. Elektros potencialo pokytis nuo 0,3 iki –0,5 V mažina vandenilio ryšio stiprumą su imidazolo žiedu IMHA molekulėje.
3. tBLM pomembraniniame rezervuare randama surišto vandens savybių turinčio vandens, bei rezervuaro dielektrinė konstanta yra žymiai sumažėjusi.
4. Jonų koncentracija pomembraniniame rezervuare didėja pH kintant iš rūgštinės į neutralią.
5. Sąveikaudamas su tBLM melitinas persitvarko iš netvarkingos į α-spiralės antrinę struktūrą per mažiau nei 15 s; vėliau melitinas pradeda kauptis pomembraniniame rezervuare.

## Metodai:

### Izotopų pakeitimas:

Stabiliųjų izotopų keitimas molekulėse leidžia identifikuoti vibracines juostas ir padeda atskirti jas nuo kitų persiklojančių juostų. Vibracijos dažnis tiesiogiai proporcingas jėgos konstantai (K) ir yra atvirkščiai proporcingas redukuotai atomų masei (μ). Redukuota masė skaičiuojama $\frac{1}{\mu} = \frac{1}{m_1} + \frac{1}{m_2}$, kur $m_1$ ir $m_2$ atitinka abiejų branduolių mases. Kadangi ryšio jėga K priklauso tik nuo branduolio ir elektronų krūvio, vibracijos dažnis $(\omega_e)$ yra veikiamas masės skirtumo. Todėl lengvesnio izotopo keitimas į sunkesnį lemia dažnio sumažėjimą.[129]

Eksperimentuose persiklojančių juostų atskyrimui buvo naudojami arba deuterinti junginiai, arba deuterinti tirpikliai, tokie kaip $D_2O$ ir $CD_3–CD_2–OD$. Buvo pasinaudojama tuo, jog vandenilio esančio prie N, O ir S atomų mainai su tirpiklio deuterio atomu įvyksta akimirksniu dėl jų didelio judrumo.[130]

### FTIR spektroskopijos sistemos:

ATR-FTIR spektrai buvo gauti naudojant Alpha spektrometrą (Bruker, Vokietija) su deimanto kristalo ATR priedu ir DTGS (angl. *deuterated triglycine sulfate*) detektoriumi. Spektrometro parametrai buvo nustatyti ties 7,5 kHz skenavimo greičiu, o spektrinė rezoliucija ties 4 $cm^{-1}$. Fonui ir mėginiui buvo kaupiama po 200 skenavimų, nebent nurodyta kitaip.

ATR-SEIRAS matavimai buvo atliekami naudojant Vertex 80v spektrometrą (Bruker, Vokietija) su skysto azoto aušinimu MCT (angl. *mercury cadmium telluride*) detektoriumi. Spektrometras veikė 40 kHz skenavimo greičiu ir 4 $cm^{-1}$ skiriamąja geba naudojant 2 mm apertūrą. Pavyzdžio ir fono skenavimams buvo kaupiama atitinkamai po 50 ir 100 iteracijų, nebent nurodyta kitaip. Eksperimentai buvo atliekami naudojant šviežiai paruoštą azoto dujų srove džiovintą Au dangos Si kristalą. Kristalas buvo komplektuojamas į kintamo kampo priedą VeeMax III su Jackfish matavimo cele J1F (Pike Technologies, JAV, 1 pav.). ATR priedas buvo naudojamas su 63 laipsnių kampu. Prieš atliekant eksperimentą, spektrometras buvo džiovinamas prapučiant sausu oru per naktį, siekiant pašalinti vandens garų sugerties juostas.

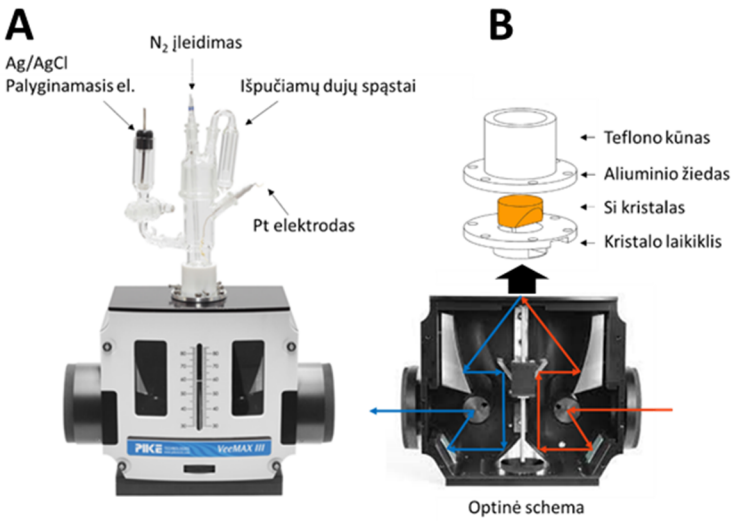


1 paveikslas. (A) VeeMax® kintamo kampo ATR priedas IR spektrometrui (Pike Technologies, JAV) su elektrochemine cele (Jackfish SEC Manufacturing). (B) Priedo optinė schema bei kristalo fiksavimo dalys.

## Elektrocheminiai matavimai

Elektrocheminiai matavimai buvo atliekami naudojant trijų elektrodų sistemą, kurioje pagrindiniu elektrodu buvo naudojamas auksas, palyginamasis Ag/AgCl ir pagalbinis Pt elektrodai. Prieš kiekvieną SEIRAS eksperimentą ant Si kristalo esančio aukso sluoksnis buvo aktyvuojamas pH 5.8 natrio acetato tirpale (0.1 M), naudojant ciklinę voltametriją (CV) valdomą PGSTAT101 potenciostato (Methrom, JAV). Prieš aktyvaciją celė buvo pripildoma natrio acetato tirpalu (0.1 M) ir 30 minučių deaeruojama azoto dujomis. CV ciklai buvo atliekami pradedant nuo ±200 mV nuo atviros grandinės potencialo (OCP) 20 mV/s skenavimo greičiu. Po 3 ciklų potencialo diapazonas buvo didinamas 100 mV anodo potencialo kryptimi ir procedūra buvo kartojama kol pasiekiama aukso oksidacija ties maždaug 1.0 V (2 pav., A). Paviršiaus švarumo bei aktyvumo patvirtinimui buvo atliekami SEIRAS matavimai ties nurodytomis potencialo vertėmis (2 pav. B). Palyginamieji (mėginio) spektrai buvo renkami prie –100 mV (600 mV), siekiant identifikuoti aukso paviršiuje adsorbuoto acetato juostą $\nu(COO^-)$ ties 1400 $cm^{-1}$. Juostos intensyvumas su kiekvienu tolimesniu CV ciklu augo. Atsižvelgiant į tai, jog pernelyg ilgas CV veikimas didina aukso sluoksnio suardymo riziką, procedūra buvo stabdoma pasiekus kelių tūkstantųjų absorbcijos vienetų ribą. Tokio stiprumo signalas buvo pakankamas tolimesniems SEIRAS eksperimentams atlikti.

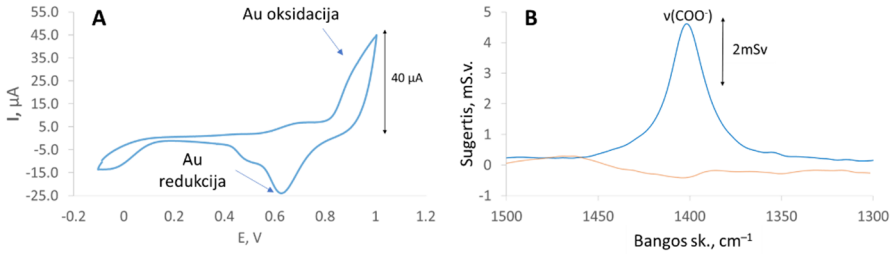


2 paveikslas. (A) CV atlikta 20 mV/s greičiu 5.8 pH 0.1 M Acetato tirpale. (B) ν($COO^-$) acetato juosta išmatuota prie 0.6 V palaikomo potencialo Au paviršiuje (mėlyna) ir nuplauto dejonizuotu vandeniu Au paviršiaus spektras (palyginamasis spektras išmatuotas palaikant –0.1 V potencialą).

### Skenuojanti elektroninė mikroskopija (SEM)

SEM mikrografijos gautos JSM-IT200 InTouchScope™ (Jeol, Japonija) mikroskopu naudojant 20–25 kV greitinimo įtampą, kaip nurodyta paveikslėliuose. Detekcijai naudotas antrinių elektronų detektorius (angl. *secondary electron detector*). Mėginiai buvo plaunami distiliuotu vandeniu ir džiovinti azoto dujų sraute prieš klijuojant juos prie stalo su lipnia anglies pluošto juostele stabilumui padidinti.

### DFT modeliavimas

Teorinis modeliavimas buvo atliekamas naudojant Gaussian 09W.[131] Geometrijos optimizacija ir dažnių skaičiavimai buvo atlikti naudojant B3LYP funkciją ir 6-311++G(2d,p) bazinį rinkinį. Apskaičiuoti dažniai ir intensyvumai buvo koreguojami pagal procedūrą, aprašytą kitur.[132] Apskaičiuotuose spektruose įsivaizduojamų juostų nebuvo gauta.

### Aukso sluoksnio formavimas

Aukso sluoksnis formavimui panaudotas beelektrodis nusodinimas, taip pat žinomas cheminio nusodinimo pavadinimu. Šis metodas buvo adaptuotas iš M. Osawa publikuotų duomenų.[58] Galutinis aukso paruošimo protokolas buvo sudarytas atsižvelgiant į keliuose literatūros šaltiniuose publikuotas sąlygas.[52,55,58,133–137]

**Kristalo paviršiaus paruošimas.** Si kristalo atspindinčioji plokštuma buvo poliruojama ranka naudojant poliravimo pagrindą (QATM, Vokietija) ir vandeninę deimantų suspensiją. Suspensijos dalelių skersmuo buvo mažinamas poliravimo eigoje nuo 3 µm (5 min), 1 µm (5 min) iki 0.25 µm (20 min). Poliravimas buvo atliekamas piešiant „∞“ simbolį bei pasukant kristalą 90 laipsnių kas 15 sekundžių. Po kiekvieno poliravimo etapo kristalas

kruopščiai plautas dejonizuotu vandeniu. Iki veidrodžio atspindžio nupoliruotas Si kristalas buvo plaunamas ultragarsinėje vonelėje du kartus po 10 minučių acetone ir vandenyje. Kristalas džiovintas azoto dujų srautu po kiekvieno plovimo. Nuplauto Si kristalo korpusas prieš aukso dengimą buvo apsaugomas 0.1 mm teflono juostele, kad būtų išvengta pažeidimų.

**Vieno etapo Au dengimas** buvo atliekamas su šviežiai paruoštu Au mišiniu. Mišinys ruošiamas teflono indelyje jį nuolat maišant. Lygūs tūriai (1) druskos tirpalo (0,15 M $Na_2SO_3$, 0,05 M $Na_2S_2O_3$, 0,05 M $NH_4Cl$), (2) $NH_4F$ (20 sv%), (3) HF (2 sv%) ir (4) $NaAuCl_4$ (0,03 M) sumaišyti iki 2 ml galutinio tūrio. (4) tirpalas buvo ruošiamas šviežiai kiekvienam dengimui. Prieš pat dengimą poliruotas Si kristalo paviršius 4 minutes buvo veikiamas 1 ml HF (2%) tirpalu. Po 4 minučių HF tirpalas keičiamas 1 ml Au mišiniu prieš tai nuplaunant kristalo paviršių dejonizuotu vandeniu. Au mišinys inkubuotas 3–4 min kambario temperatūroje, kol dangos spalva pakito į ryškiai geltoną. Dengimo reakcija buvo stabdoma perkeliant kristalą į dejonizuoto vandens vonią 5–10 minučių intervalui. SEM vaizdai rodo maždaug 50 nm skersmens nanostruktūrų susidarymą (3A paveikslas).

**Dviejų etapų Au dengimas** buvo atliekamas, kad pagerėtų aukso sluoksnio stabilumas pagal Yaguchi ir Uchida publikuotus duomenis. Po pirmojo aukso sluoksnio susidarymo paviršius buvo nuplaunamas distiliuotu vandeniu ir greitai išdžiovintas azoto sraute. Keletas lašų (~ 0,6 iki 0,8 ml) koncentruotos *aqua regia* rūgšties tirpalo (4:1 $HCl/HNO_3$) buvo pridėti ant paviršiaus, kad ištirpintų susidariusį aukso sluoksnį, kuris tuomet buvo nedelsiant nuplaunamas distiliuotu vandeniu, o paskui džiovinamas azotu. Silicio paviršius tapo pilkas ir matinis. Antrasis aukso nusodinimas buvo atliekamas pridedant Au mišinį tokiam pačiam laikui, kaip ir pirmojo aukso sluoksnio formavimo metu. Dengimas buvo sustabdytas įmerkiant Si kristalą į vandens vonią 5 min, o paskui kristalas buvo džiovinamas oro srove ir montuojamas į SEIRAS priedą. Kiekvieno kristalo paruošimas vyko prieš eksperimentą, kad būtų išvengta ilgalaikio saugojimo ir galimo užsiteršimo.

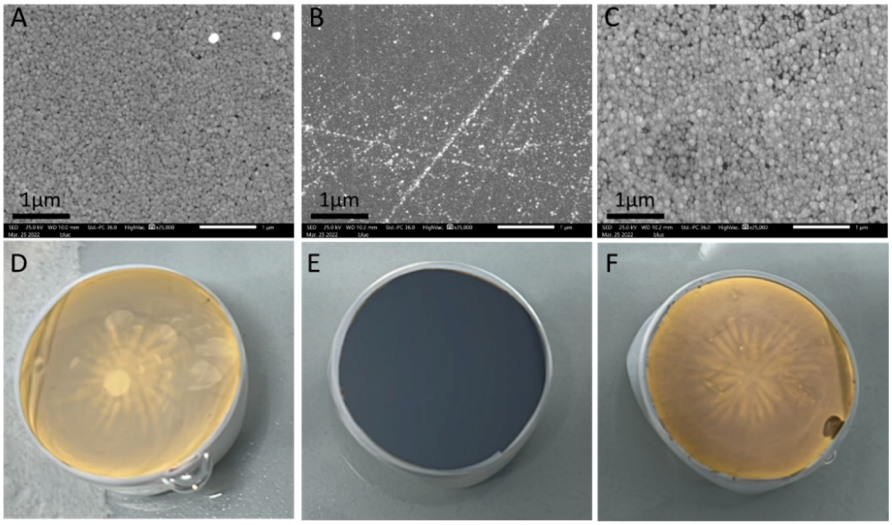


3 paveikslas. Si kristalo paviršiaus SEM mikrografijos (A–C) po vieno etapo Au dengimo (A), aukso pašalinimo *aqua regia* tirpalu (B) ir dviejų etapų aukso dengimo (C). SEM tyrimuose naudotų kristalų nuotraukos (D–E).

### SAM ir membranos formavimas

Savitvarkiai monosluoksniai buvo formuojami inkubuojant tiolio molekulių etanolinį tirpalą ant šviežiai paruoštos aukso dangos. Šiame darbe buvo panaudoti keli skirtingi SAM mišiniai: (i) WC14, (ii) WC14/βME 3:7, (iii) WC14/βME/MHP 3:3:4, (iv) IMHA, (v) IMHA/Frag 1:1, (vi) IMHA/Frag 1:5 ir (vii) Frag. Prieš SAM formavimą, aukso paviršius buvo keletą kartų nuplautas dejonizuotu vandeniu bei išmatuotas palyginamasis SEIRAS spektras, naudotas vandens spektrinių juostų atimčiai. Celė praplauta grynu etanoliu, kuris buvo skiedžiamas įpilant SAM inkubacijos tirpalo iki bendros 0,5 mM tiolių koncentracijos. SAM formuotas mišinį inkubuojant ilgiau nei 1 valandą. Po inkubacijos paviršius keletą kartų nuplautas etanolu, perteklinių tiolių pašalinimui nuo suformuoto monosluoksnio.

### Membranos formavimas

Dvisluoksnių lipidinių membranų formavimas susideda iš keletos procesų:

- inkarinio SAM suformavimo;
- daugiasluoksnių pūslelių (MLV) paruošimo;
- MLV išliejimo ant SAM paviršiaus, taip suformuojant dvisluoksnę lipidinę membraną (BLM).

SAM, tinkamas tBLM formavimui, buvo ruošiamas ant aukso inkubuojant 0,5 mM etanolio tirpalą su WC14 ir β-merkaptoetanolio (βME) junginiais, atitinkamų 3:7 moliniu santykiu. hBLM formavimui SAM buvo

ruošiamas tik iš WC14 tiolių. Per 1 valandą suformuotas SAM buvo atsargiai plaunamas pirmiausia etanoliu ir po to fosfato buferiniu (0,1 M NaCl, 0,01 M $NaH_2PO_4$, pH 4,4) tirpalu.

MLV suspensijoms paruošti, buvo naudojamas 4:6 santykio cholesterolio ir 1,2-dioleoil-sn-glicerolio-3-fosfocholino (DOPC) mišinys. Lipidai ištirpinti 99% chloroforme iki galutinės 10 mM koncentracijos ir prieš naudojimą chloroformas išgarintas azoto srautu, taip suformuojant ploną, akimi matomą, lipidų plėvelę. Plėvelė suspenduota į homogenišką drumstą tirpalą fosfato buferio tirpalu, lėtai traukiant-švirkščiant automatine pipete (~1 ciklas/s).[93]

Membrana ruošta įpilant daugiasluoksnių pūslelių suspensijos ant SAM esančio fosfatiniame tirpale. Viskas inkubuojama kambario temperatūroje 1 val. ar kaip nurodytą prie eksperimento duomenų. Visų eksperimentų metu reakcijos celė uždengiama siekiant sumažinti tirpiklių nugaravimą. Po membranos suformavimo, celė plaunama fosfatinio buferio tirpalu siekiant pašalinti perteklinius lipidus, galimai trukdančius sekantiems eksperimento etapams.

### Duomenų tvarkymas

Visi neapdoroti spektriniai duomenys buvo tvarkomi naudojant OPUS 7.5 programinę įrangą (Bruker, Vokietija). Apdoroti spektrai buvo eksportuojami į tinkamą formatą tolimesnei analizei ir vaizdinimui naudojant Origin 9.5 (OriginLab, JAV) arba Excel 2019 (Microsoft, JAV). Spektrinių juostų išskirstymui (dekonvoliucijai) buvo naudojama GRAMS/AI 8.0 programinė įranga (Thermo Scientific Inc., JAV).

**Imidazolo žiedą turinčių savitvarkių monosluoksnių elektrocheminė SEIRAS analizė**

### Histidino svarba ir savybės

Histidinas yra esminė aminorūgštis, išsiskirianti savo savybėmis lyginant su kitomis aminorūgštimis. Jo pKa vertė 5,9, kas yra artima fiziologinei pH vertei. Histidino šalutinė imidazolo (Im) grandinė gali dalyvauti svarbiose sąveikose, kurios yra esminės baltymų struktūrai ir kataliziniam aktyvumui.[7,144] Im gali formuoti vandenilinius ryšius, veikti kaip aromatinė sistema ir koordinuoti metalo (II) katijonus per nepriklausomą elektronų porą.[8] Im pKa vertė siekia 6,9, todėl fiziologinėmis sąlygomis protonuojamas tik vienas azoto atomas, dėl ko yra stebimi du tautomerai (4 pav.). Tautomeras-I (T-I) protonuotas ties N1 atomu (N1-H, N3), o Tautomeras-II (T-II) ties N3 atomu (N1, N3-H). Kambario temperatūroje, neutralaus pH tirpaluose nedidelio energetinio pranašumo vyrauja T-I forma.[145] Tautomerinę pusiausvyrą gali paveikti temperatūros, tarpmolekulinių sąveikų, cheminės aplinkos ir kiti veiksniai. Pavyzdžiui, žinoma, jog Im grupę turinčių molekulių adsorbcija ant metalo paviršiaus sąlygoja aiškų T-I perėjimą į T-II.[146]

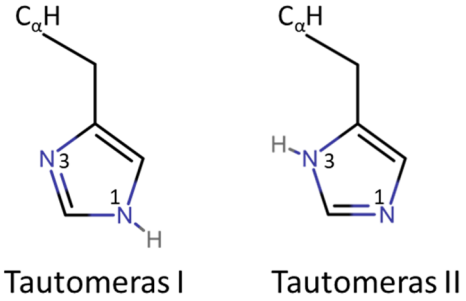


4 paveikslas. Histidino šoninės grandinės I ir II tautomerų struktūra fiziologinėmis pH sąlygomis.

Vandenilis ryšys yra viena iš svarbiausių sąveikų, reguliuojanti baltymų konformaciją ir susipakavimą. Neutralioje būsenoje Im žiedas gali veikti kaip vandenilio donoras ir kaip akceptorius. Tačiau tokių sąveikų tyrimas įelektrintuose paviršiuose yra sudėtingas dėl metodų trūkumo. Vibracinė spektroskopija leidžia analizuoti molekulių aplinką, tarpmolekulinę sąveiką ir elektros lauko sukeltus molekulinius pokyčius. Pavyzdžiui, Raman spektroskopija gaunama informaciją apie Im struktūrą ir sąveikas su dvivalenčiais metalo katijonais tiek natūraliose biomolekulėse, tiek modeliniuose junginiuose.[145–154] Kita vertus, Furjė transformacijos infraraudonųjų spindulių absorbcijos spektroskopijos (FTIR) absorbcijos

skerspjūvis daug didesnis, todėl ji ypač naudinga dinaminiams procesams tirti ypač tada, kai tiriamų molekulių skaičius yra ribotas.

Siekiant geriau suprasti Im sąveiką su jį supančia aplinka organinio sluoksnio-vandens fazių riboje, buvo panaudotas ATR-SEIRAS metodas. Tikslui pasiekti, ant aukso paviršiaus buvo formuojami monosluoksniai iš mūsų laboratorijoje susintetinto N-(2-(1H-imidazol-4-yl)etil)-6-merkaptoheksanamido (IMHA) junginio (5 pav.). Funkcinės Im grupės pokyčių stebėsena SEIRAS metodu suteikė naujų duomenų apie savitvarkių molekulių adsorbciją ir persiorientavimo dinamiką. Stebint potencialo sukeltus SAM pokyčius, nustatyti vandenilinių ryšių sąveikos su Im grupe spektroskopiniai žymenys. Šiuo tyrimu buvo geriau suprasta Im grupės elgsena fazių riboje, kas labai svarbu baltymų struktūrai ir jų funkcijoms. Surinkta informacija taip pat naudinga paviršiaus chemijos taikymams.

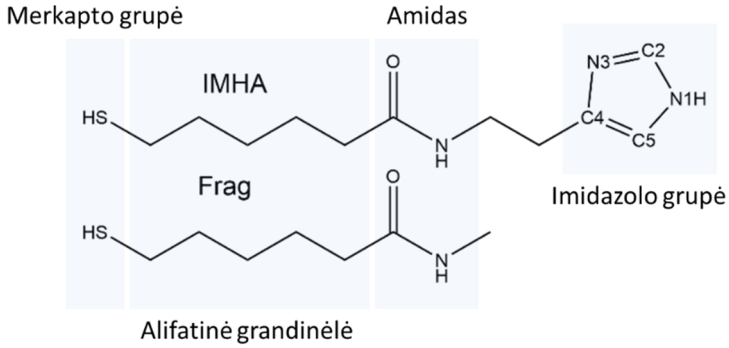


| | |
|---|---|
| **IMHA** | N-(2-(1H-imidazol-4-il)etil)-6-merkaptoheksanamidas |
| **Fragmentas** | 6-merkapto-N-metilheksanamidas |

5 paveikslas. IMHA ir fragmento junginių struktūra.

Norint geriau suprasti Im sąveiką su aplinka ant aukso paviršiaus tirti skirtingos sudėties savitvarkiai monosluoksniai, sudaryti iš Im žiedą turinčių alkanotiolių molekulių ir paviršiaus skiediklio fragmento molekulių (5 pav.). Taikant H/D pakeitimą, SEIRAS metodu buvo tirta SAM susidarymo kinetika bei žiedo įtaka monosluoksnio struktūrai. Išmatuoti amidinių ryšių intensyvumo pokyčiai laike (6A pav.) leido nustatyti SAM mišinių formavimosi aukso paviršiuje tendencijas. Pademonstruota, jog didėjant IMHA junginio santykiniai koncenracijai mišriame monosluoksnyje, jis formuojasi lėčiau. Visgi, amidų grupės alkanų grandinėse orientuojasi optimaliai paviršiui per 30 inkubacijos minučių, nepriklausomai nuo SAM sudėties (6B pav.).

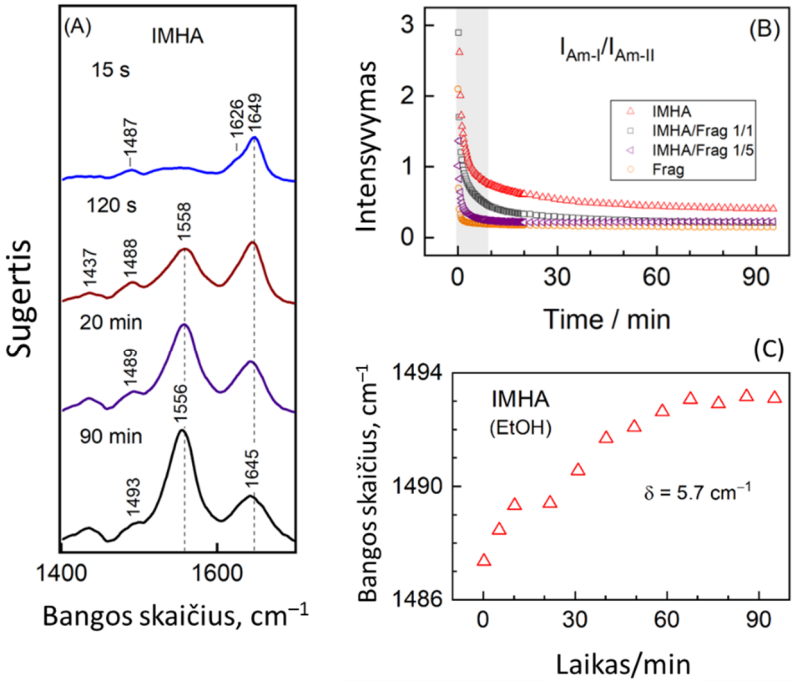


6 paveikslas. (A) IMHA SAM junginio SEIRAS spektrai skirtingais adsorbcijos laikais. (B) Skirtingų SAM mišinių Am-I/Am-II santykio kitimo laike kreivės. (C) Im žiedo kombinacinio virpesio ν(C2–N3) + β(C2H) kitimo kreivė.

Stebint Im spektroskopinio žymens, esančio ties 1490 $cm^{-1}$, poslinkį, buvo nustatyta, kad galinių funkcinių grupių pokyčiai yra lėtesni nei SAM amidinių grupių orientavimasis ir tęsiasi iki 60 minučių (6C pav.). Šie pokyčiai susiję su stipresnių vandenilio ryšių prie Im grupės formavimusi. IMHA SAM sudaro struktūriškai standžius organinis sluoksnis su amido grupėmis, kurios tik dalinai dalyvauja vandenilio ryšių tinkle.

Suformuoti IMHA/Fragmento monosluoksniai taip pat buvo analizuojami keičiant potencialą. Buvo parodyta grįžtama įtaka monosluoksniams potencialui neigiamėjant nuo 0,3 V iki −0,5 V (7 pav.). Am-II smailės dažnio mažėjimu potencialui neigiamėjant (7A pav.) grindžiamas tarpmolekulinių vandenilinių ryšių silpnėjimas monosluoksniuose. Tą patį rodo ir alkilo grupės $\nu_{as}(CH_2)$ dažnio didėjimas, siejamas su monosluoksnio tvarkos sumažėjimu (7B pav.). Šis monosluoksnio vandenilinių ryšių silpnėjimas potencialui neigiamėjant buvo fiksuotas visiems tirtiems IMHA/Fragmento SAM mišiniams (7C pav.). Taip pat buvo nustatyta, jog SAM padėtis paviršiaus atžvilgiu yra labiau vertikali prie teigiamo potencialo ir labiau palinkusi potencialui mažėjant. Tik gryno IMHA SAM atveju nebuvo stebima jokių Am-I/Am-II santykio pasikeitimų prie skirtingų potencialų (7D

pav.), kas parodė, jog tankiai išsidėsčiusios Im grupės trukdo viena kitai ir tai įtakoja viso monosluoksnio savybes.

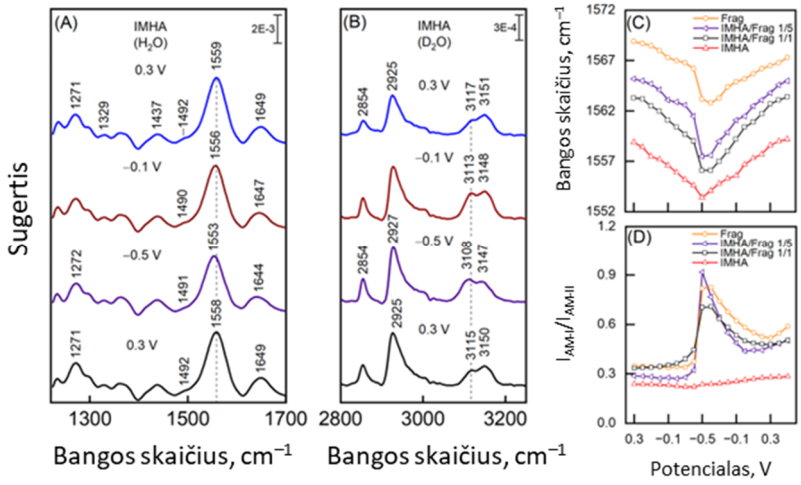


7 paveikslas. IMHA monosluoksnio SEIRAS spektrai prie skirtingų įtampos verčių (A) pirštų antspaudų zonoje vandenėje terpėje ir (B) C–H regione $D_2O$ terpėje. (C) Am-II bangos skaičiaus priklausomybės nuo potencialo kreivės skirtingiems SAM mišiniams. (D) Skirtingų SAM Am-I/Am-II santykio kitimo priklausomybės nuo potencialo kreivės.

Buvo nustatyta, jog suformuotame SAM Im virpesių (=C–H) 3115 ir 3150 $cm^{-1}$ dažnis mažėja neigiamo potencialo sąlygomis, su dažnio pokyčiais –10,4 ir –6,3 $cm^{-1}V^{-1}$ (8 pav.). Šis dažnio sumažėjimas buvo priskirtas vandenilio ryšio tarp žiedo ir šalia esančio vandens silpnėjimui neigiamai įkrautoje fazių riboje. Atitinkamai, juostų intensyvumo kitimas parodė, jog Im žiedo pozicija kinta, orientuojant C2–H ryšį statmeniau paviršiui neigiamo potencialo aplinkoje.

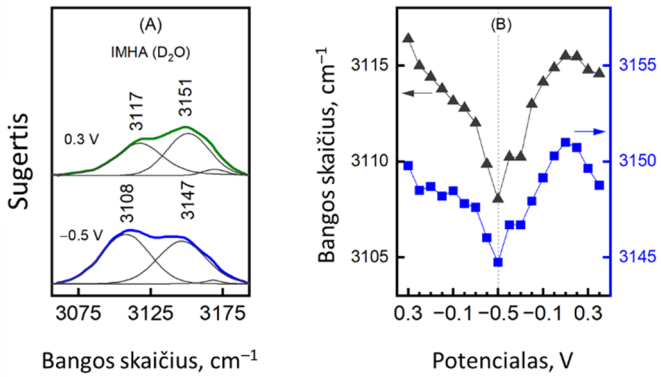


8 paveikslas. Im žiedo valentinių C–H virpesių ties 3117 ir 3151 $cm^{-1}$ SEIRAS duomenys. (A) IMHA SAM SEIRAS spektrai $D_2O$ tirpale prie 0,3 ir –0,5 V potencialo. (B) 3117 ir 3151 $cm^{-1}$ dažnių priklausomybės nuo potencialo kreivės.

**Pakabinamų dvisluoksnių lipidinių membranų formavimosi ant aukso paviršiaus tyrimas SEIRAS metodu**

Pakabinamos dvisluoksnės lipidinės membranos veikia kaip universalios platformos skirtos nagrinėti biologinius procesus ir naudingos biosensorių bei biomedicininiuose tyrimuose.[10,97,177–180] Vienas iš jų esminių privalumų – pomembraninis vandens rezervuaras, kuris susidaro tarp kietojo substrato (pvz., aukso elektrodo) ir lipidų dvisluoksnio ir užtikrina transmembraninių baltymų integraciją ir stabilumą.[181,182] Be to, rezervuaras padeda išlaikyti baltymų judrumą membranoje reikalingą jų funkcijų atlikimui.

Pakabinamos dvisluoksnės modelinės membranos paprastai paruošiamos dviem etapais, pirmiausia suformuojant inkarinį monosluoksnį iš poliarinių peptidų, angliavandenių, polimerų ar tiolio molekulių ant aukso substrato.[70,180,183–185] Po ko seka lipidų vezikulių išliejimas ant inkarinio sluoksnio taip suformuojant pakabinamą dvisluoksnę lipidinę membraną (tBLM). Tokių membranų konstravimas panaudojant SAM yra pranašus dėl jo paprastumo, pakartojamumo, mažo defektų tankio ir galimybės kontroliuoti dvisluoksnio klampą. Aukso pagrindas yra palankus substratas tBLM dėl stiprios sąveikos su SAM molekulių merkapto grupe. Norint sukurti vandens rezervuarą tarp elektrodo ir dvisluoksnio, ant aukso suformuojamas mišrus SAM, susidedantis iš trumpų ir ilgų grandinių molekulių. Šis metodas užtikrina pomembraninio rezervuaro suformavimą.[70,186]

Inkarinių SAM struktūra ir sudėtis lemia tBLM stabilumą bei funkcionalumą. Tačiau vis dar trūksta informacijos apie detalų šių molekulinių sluoksnių formavimąsi tirpale.[98,132,182,187–189] Daugiausia tai susiję su metodikos trūkumu, kuris leistų detaliai analizuoti elektrodo ir tirpalo fazių ribos pasikeitimus. SEIRAS metodu galima detaliai tirti molekulinių sluoksnių struktūrą, jų adsorbciją ir orientaciją fazių riboje.[190,191] Ankstesni tyrimai rodo, kad in situ SEIRAS metodika yra efektyvi analizuojant adsorbuotų peptidų struktūrą, monosluoksnių konformaciją bei paviršiuje prikabintų biosensorių funkcionalumą.[190–193] Šiuo tyrimu buvo siekiama detaliau ištirti inkarinio monosluoksnio bei lipidinio dvisluoksnio formavimąsį ant aukso elektrodo panaudojant in situ SEIRAS metodą.

Paviršiaus sustiprinta infraraudonųjų spindulių absorbcijos spektroskopija buvo naudojama tiriant dviejų etapų procesą, susijusį su pakabinamų dvisluoksnių lipidų membranų (tBLM) konstravimu ant aukso. Pirmasis etapas susijęs su mišraus savitvarkio monosluoksnio formavimu, o antrasis etapas - su pakabinamos dvisluoksnės lipidinės membranos formavimusi ant mišraus monosluoksnio (WC14/βME, 30/70 mol%). ATR-SEIRAS metodu buvo parodyta, jog suformuoto SAM WC14 junginio

etilenglikolio grandinės yra daugiausia amorfinės būsenos, o alkilo grandinės išsidėsto netvarkingai. Taip suteikiant reikiamą monosluoksnio lankstumą tBLM formavimui. In situ SEIRAS duomenys leido detaliau charakterizuoti modelinės pakabinamos membranos, sudarytos iš DPPC-$d_{62}$/cholesterolio-$d_7$ 60/40 mol% santykio junginių, susidarymą bei su tuo susijusius procesus. Eksperimentiniais duomenimis parodyta, jog lipidai sąveikauja su inkariniu monosluoksniu nuo pat pradžių (9 pav.). Kintantis WC14 junginių valentinių $\nu_{as}(CH_3)$ virpersių intensyvumas rodo alkilo grandinių orientacijos kitimą paviršiaus atžvilgiu į vertikalesnę.

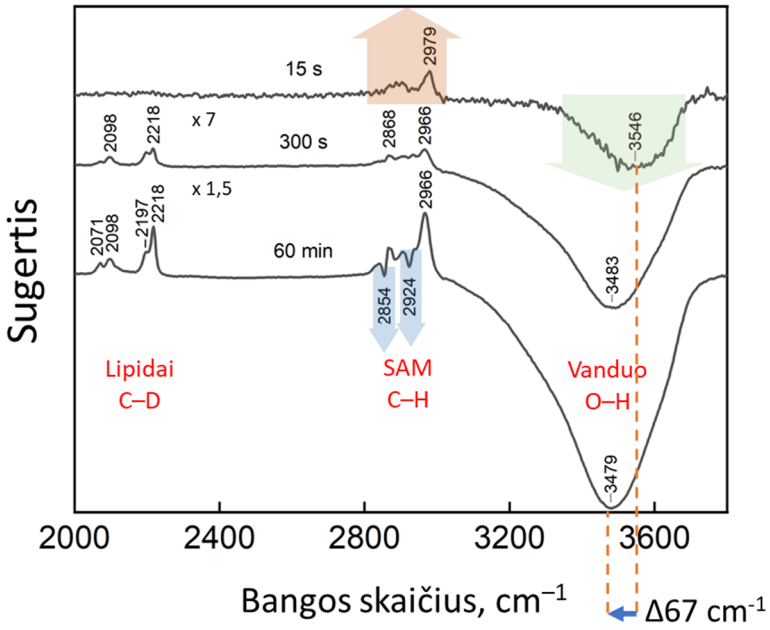


9 paveikslas. SEIRAS skirtuminiai spektrai reprezentuojantys pradinę, tarpinę ir galutinę tBLM formavimosi fazę (DPPC-$d_{62}$/cholesterolis-$d_7$, 60/40 mol%) ant mišraus SAM (WC14/βME, 30/70 mol%) vandenyje.

Surinkti SEIRAS kinetiniai duomenys leido identifikuoti dviejų etapų pakabinamos dvisluoksnės lipidų membranos formavimąsi (10 pav.). Visų pirma lipidai adsorbuojasi ant SAM padengto aukso paviršiaus tuo pačiu metu išstumdami vandens molekules. Po to seka, membranos formavimasis jai sąveikaujant su monosluoksniu. Išstumiamo vandens valentinių O–H virpesių smailės poslinkis laike į mažesnės energijos pusę ($\Delta 67$ $cm^{-1}$) parodė, jog pirmiausia išstumiamos iš pomembraninio sluoksnio vandens molekulės pasižyminčios silpniausiais vandeniliniais ryšiais, galimai esančios toliau nuo paviršiaus. Vėliau išstumiamos labiau vandenilių ryšių susaistytos molekulės. Iš kinetinių kreivių (10 pav.) nustatyti lipidinio sluoksnio formavimosi ir

vandens išstūmimo procesų puslaikiai ($x_0$), kurie lygūs 6,0 ± 0,35 min ir 4,5 ± 0,11 min (I $\nu_{as}(CD_3)$; A $\nu(OH)$), kai tuo tarpu išmatuotas SAM monosluoksnio kitimo puslaikis ilgesnis – 9,9 ± 0,31 min (pagal I $\nu_{as}(CH_2)$). Pokyčiai visame modelinio tBLM formavimo procese nusistovi ties 60 minučių laiko žyma.

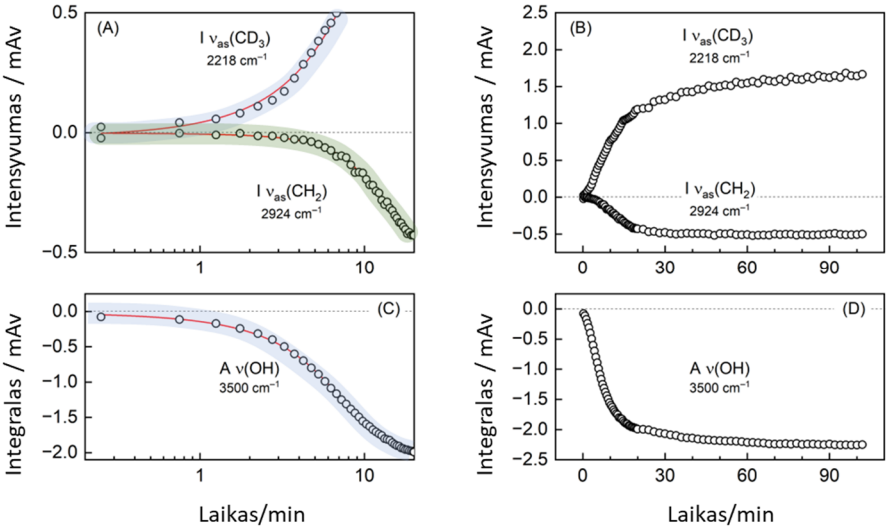


10 paveikslas. Spektrinių smailių intensyvumo kitimo laike kreivės tBLM formavimosi pirmosiomis 20 minučių (A ir C) ir visame 105 minučių periode (B ir D).

**Potencialo įtakos pomembraniniam vandeniui DOPC/cholesterolio tBLM sistemoje tyrimas SEIRAS metodu**

Vanduo - esminė įvairių natūralių ir modelinių sistemų molekulė, svarbi jų savybėms ir veikimui. Unikalios fizikocheminės savybės, tokios kaip aukšta dielektrinė skvarba, vandenilinių ryšių formavimas, poliškumas, padaro vandenį gyvybiškai svarbiu komponentu daugelyje reiškinių.[211,212] Vandens molekulių elgesys fazių riboje ir pomembraniniuose sluoksniuose yra ypač svarbus formuojant SAM, tBLM ir kitas biomimetines sistemas.[9,10] Yra žinoma, jog vandens dielektrinės savybės fazių riboje yra mažesnės nei skystyje ir gali nukristi iki ε ~2 pirmiesiems dviem ar trims vandens molekulių sluoksniams.[213] Visgi tiesioginiai dielektrinės konstantos matavimai fazių riboje yra sudėtingi, ypač sudėtingose sistemose. SEIRAS metodas yra vienas iš nedaugelio šiai užduočiai tinkamų metodų dėl jo trumpo veikimo nuotolio bei didelio absorbcijos koeficiento vandeniui.[140]

Žinoma, jog vanduo gali formuoti tvarkingas vandenilinių ryšių tinklo struktūras nukreiptais link paviršiaus arba nuo jo, priklausomai nuo paviršiaus savybių.[221] Be to, vandens elgesys fazių riboje gali paveikti SAM ir tBLM adsorbciją, tvarką, stabilumą bei jų sąveiką su kitomis biomolekulėmis.[216] Pademonstruota, kad metalo paviršiuje adsorbuotas sBLM ir vandens pagalvėle paremtos pakabinamos dvisluoksnės lipidų membranos (fBLM) yra „pakeliamos“, kai vandens molekulės juda link metalo elektrodo, prie neigiamo potencialo.[222–224]

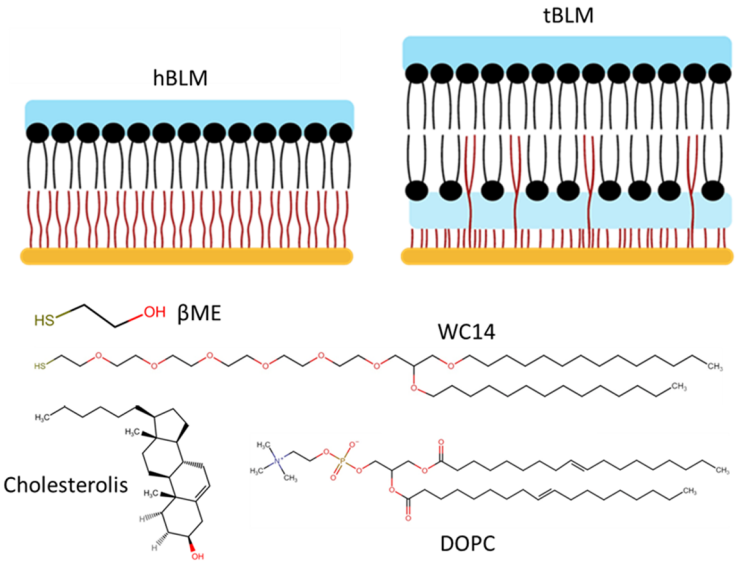


11 paveikslas. hBLM ir tBLM struktūros grafinė reprezentacija (viršuje). SAM ir BLM modelinėms struktūroms panaudoti junginiai (apačioje).

Šiame darbe vandens elgesys pomembraniniame sluoksnyje buvo tiriamas palyginant potencialio bei pH pasikeitimo sukeliamus skirtumus tBLM ir hBLM sistemoms (11 pav.). ATR SEIRAS metodu buvo palyginti suformuoti SAM ir BLM, bei identifikuoti pagrindiniai jų skirtumai (12 pav.). hBLM sistemai paruoštas monosluoksnis iš 100% WC14 junginių formuoja labiau išreikštą trans etilenglikolio amorfinę struktūrą, ką parodė glikolio segmento $\nu_{as}$(C–O–C) didesnis virpesių dažnis ties 1149 $cm^{-1}$. Smailės šioje padėtyje dažniausiai stebimos nehidratuotose sistemose.[226,227] Kaip ir buvo tikimasi, hBLM membrana formuojama tvarkingiau, ką išduoda mažesnio dažnio asimetriniai $\nu_{as}(CH_2)$ virpesiai 2925 $cm^{-1}$ lyginant su 2927 $cm^{-1}$ dažnio smailėmis tBLM sistmoje. Takesnę tBLM membranos struktūrą taip pat patvirtina labiau išplitęs pirštų antspaudų 1100–1500 $cm^{-1}$ regionas.

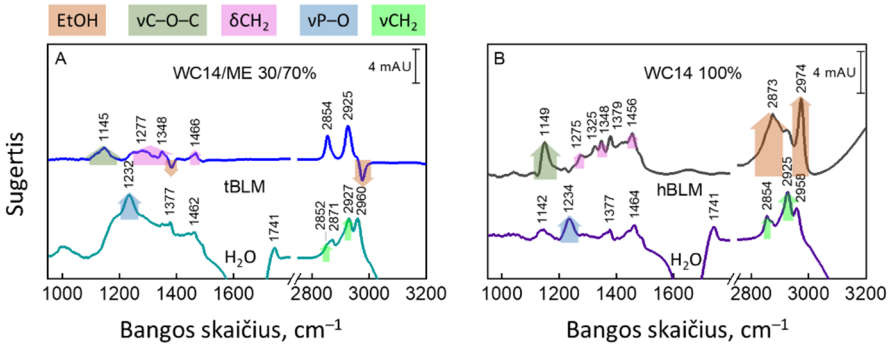


12 paveikslas. SAM ir BLM SEIRAS spektrai ant aukso. SAM suformuoti iš (A) WC14 ir βME (30:70 mol%) bei (B) WC14 (100 mol%). Lipidinės membranos formuotos iš DOPC ir cholesterolio (60:40 mol%).

Nustatyta, kad keičiant potencialą vandens kiekis gali būti moduliojamas tBLM ir hBLM sistemoms. SEIRAS eksperimentu parodyta, jog potencialui mažėjant nuo –0,4 V iki –0,8 V, tBLM sistemoje vanduo ima kauptis pobmembraninėje erdvėje, o hBLM sistema praranda vandenį (13 pav.). Parodyta, jog potencialui keičiantis hBLM sistemoje pirmiausiai paveikiamas laisvas vanduo, matomas ties 3624 $cm^{-1}$. Palaipsniui seka surišto vandens mažėjimas, O–H smailei slenkantis 3477 $cm^{-1}$ link. tBLM sistemoje ties neigiamu potencialu pritraukto vandens O–H smailės padėtis ties 3382 $cm^{-1}$ rodo vandenilinių ryšių tinklo stiprėjimą pomembraninėje erdvėje.

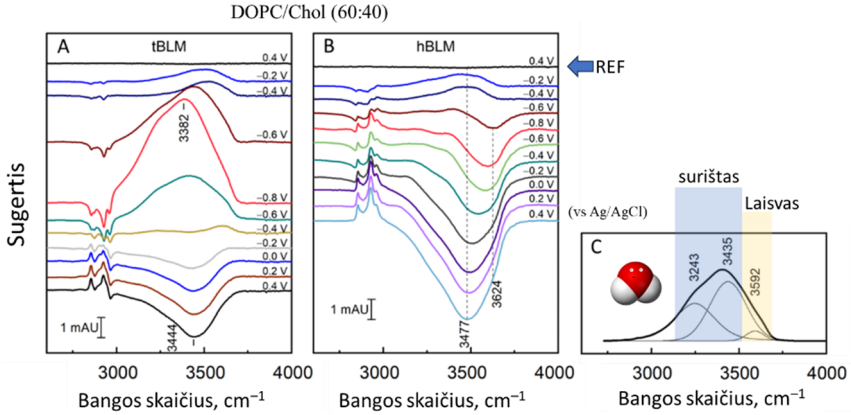


13 paveikslas. SEIRAS spektrai prie skirtingų potencialų. (A) tBLM ir (B) hBLM sistemos testuotos 0,1 M $Na_2SO_4$ ir 0,05 M $NaH_2PO_4$ pH 4,6 tirpale. (C) Vandens SEIRAS spektras.

Potencialui grįžtant į teigiamą, buvo stebimas tBLM pomembraninio vandens būsenos grįžimas į artimą pradinei. Matomas vandens sumažėjimas galimai dėl sistemos pertvarkos ir membranos priartėjimo prie paviršiaus (pomembranės erdvės suplonėjimo). hBLM sistemoje vandens juostų intensyvumo mažėjimas buvo stebimas ir toliau. Išmatuota, jog abejose sistemose buvo matomas panašus nuo potencialio kintantis bendras vandens kiekis.

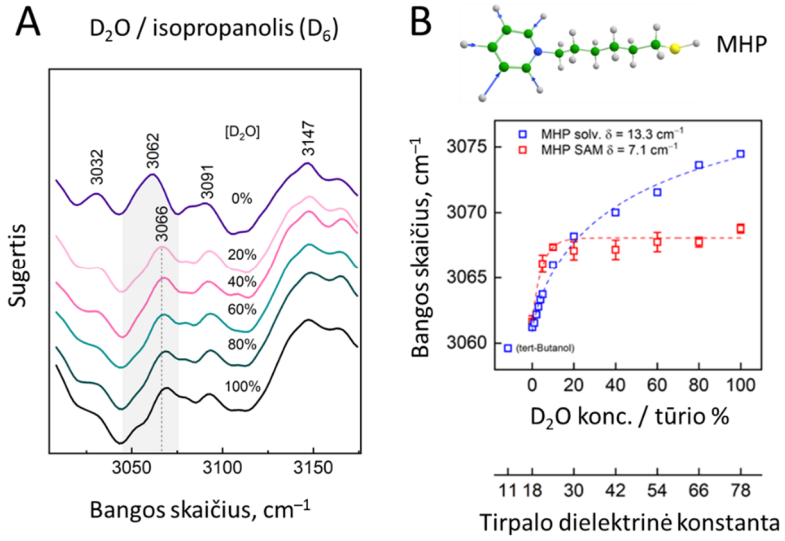


14 paveikslas. (A) WC14/ME/MHP (3/3/4 mol%) junginių monosluoksio SEIRAS spektrai skirtingo santykio $D_2O$:izopropanolis-$d_6$ tirpaluose. (B) Laisvos ir adsorbuotos formos MHP junginio =C–H valentinių virpesių dielektrinės konstantos kalibracinės kreivės.

Gana svarbus tBLM parametas yra pomembraninio rezervuaro dielektrinė skvarba. Manoma, kad vandens dielektrinė konstanta pomembraniniame rezervuare sumažėja, dėl ko didėja tirpalo jonų laisvoji Gibbs‘o energija veikianti membranos elektrines savybes.[213]

Mūsų laboratorijoje susintetinto, N-(6-merkapto)hexilpiridino (MHP) įterpimas į SAM sudėtį buvo panaudotas dielektrinės aplinkos SAM sluoksnyje tirti (14 pav.). Siekta, patikrinti, ar šis junginys gali būti naudojamas spektroskopiniu dielektrinės konstantos žymeniu SEIRAS matavimuose. Išmatavus suformuoto WC14/ME/MHP (3/3/4 mol%) junginių monosluoksnio SEIRAS $D_2O$:izopropanolio-$d_6$ tirpalų gradiente, sudaryta piridino žiedo =C–H virpesių poslinkio kreivė (17B pav.). Atitinkami MHP junginio matavimai tirpale parodė $\delta$ = 13,3 $cm^{-1}$ =C–H smailės poslinkį 0–100% $D_2O$:izopropanolio-$d_6$ gradiente, lyginant su $\delta$ = 7,1 $cm^{-1}$ išmatuotu fazių riboje ant aukso paviršiaus. Nustatyta, jog SAM sluoksnio aplinka yra mažiau hidrofilinė su dielektrinės konstantos verte lygia 30. Papildomas tBLM sluoksnis neturėjo įtakos MHP aplinkai, išlaikant piridino žiedo =C–H dažnį nepakitusiu. Kas rodo, jog tBLM formavimas šioje sistemoje neįtakoja SAM dielektrinės aplinkos.

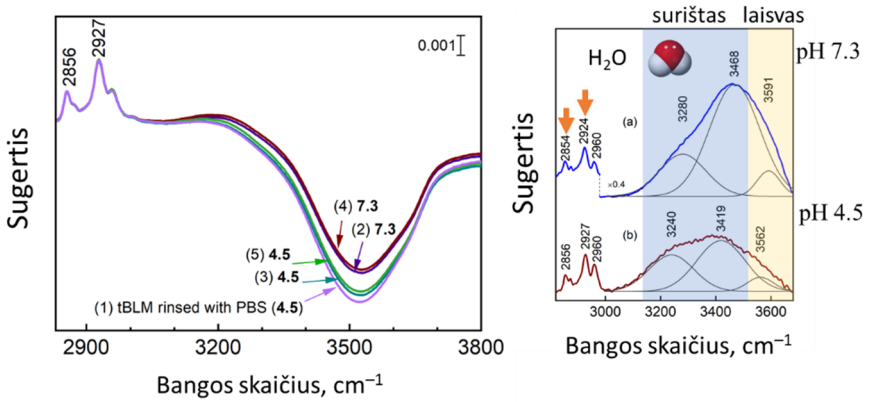


15 paveikslas. tBLM SEIRAS spektrai 2830–3800 $cm^{-1}$ intervale. Kairė: nuoseklus pH keitimas iš 4,5 į 7,3 ir atgal pažymėtas skaičiais nuo 1 iki 5. Intensyvumai normalizuoti pagal metileno asimetrinių virpesių 2927 $cm^{-1}$ smailę, fonui naudotas vandens ant aukso SEIRAS spektras. Dešinė: tBLM SEIRAS (2) ir (3) spektrai su išskleistomis vandens juostomis. Spektrai perskaičiuoti fonui pritaikant (1) spektrą. Rodyklėmis pažymėti $\nu_s(CH_2)$ ir $\nu_{as}(CH_2)$ virpesiai.

Galiausiai, SEIRAS matavimais buvo parodyta, jog pakabinamos dvisluoksnės lipidinės membranos yra jautrios pH pokyčiams. pH kintant iš rūgštinio į neutralų vanduo pritraukiamas arčiau paviršiaus į pomembranį rezervuarą (15 pav., kairė). Procesas yra grįžtamas aplinkai vėl rūgštėjant. Detalesnė SEIRAS vandens juostų analizė parodė, jog neutralioje aplinkoje

pritraukiamas surištas vanduo, kurio juostos pasislinkusios į didesnių dažnių pusę, silpnesnės vandenilinės sąveikos žymuo. Taip pat pastebėta, jog prie neutralaus pH fosfolipidų alkilo grandinės suartėja, dėl ko $\nu_s(CH_2)$ ir $\nu_{as}(CH_2)$ juostų padėtis pasislenką į mažesnės energijos pusę (18 pav. dešinė). Įvertinus SEIRAS bei kitos laboratorijos bendros veiklos rezultatus, buvo pasiūlyta, kad padidėjęs vandens kiekis pomembraniniame rezervuare rodo hidratuotų krūvio nešėjų koncentracijos padidėjimą, dėl ko sumažėja savitoji pomembraninė varža.[231]

**Melitino sąveikos su fosfolipidine dvisluoksne membrana in situ tyrimas**

Melitinas, pagrindinis bičių nuodų komponentas, yra mažas antimikrobinis peptidas (AMP). Žinoma, kad APM lipidų membranose formuoja toroidines poras ir veikia kaip organizmų gynybos mechanizmo dalis.[119,234,235] AMP apibrėžiami kaip maži peptidai, sudaryti iš 12–60 amino rūgščių bei aptinkami įvarios struktūrinės konformacijos, pavyzdžiui, α-spiralės (16 pav.), β-lakšto, ciklinės, globulinės ir kitokių junginių. Nepaisant šių struktūrinių AMP variacijų, jie apibūdinami kaip katijoniniai, amfipatiniai peptidai su turintys platų mikrobicidinį poveikį, veikiantį per membranos pralaidumo funkcijos trikdymą.[115] Daug mokslinių tyrimų skiriama AMP, visgi, jų veikimo mechanizmas išlieka nevisiškai suprastas, o dėl eksperimentinių rezultatų interpretacijų teisingumo nuolat diskutuojama.[115,236,237]

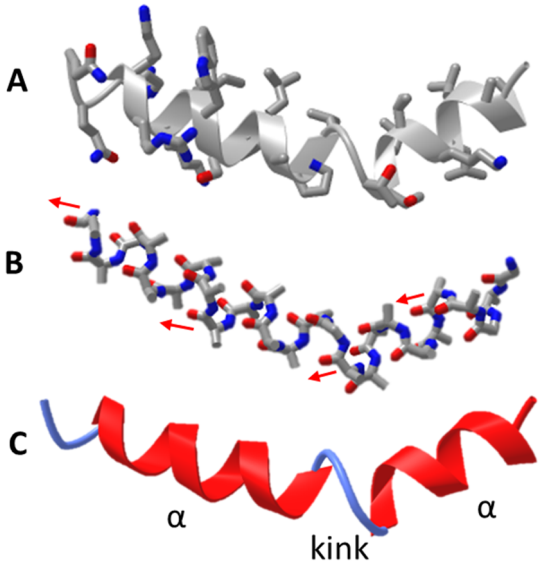


16 paveikslas. Melitino struktūra pavaizduota (A) su šoninėmis aminorūgščių grupėmis, (B) peptidinės grandinės bei (C) α-spiralės formose. Rodyklėmis parodyta valentinių C=O virpesių kryptis (PDB: 2MLT).

Melitinas, kaip nespecifinės lizės peptidas, yra geras AMP klasės peptido pavyzdys leidžiantis tirti prasiskverbimo per membraną procesus ir su tuo susijusius veiksnius. Jo veikimo mechanizmas yra aiškinamas dvejų fazių procesu.[238] Pirma, sąveikaudamas su membrana jis orientuojasi iš netvarkingos[239] į α-spiralės konformaciją (16C pav.),[234] lygiagrečiai membranos paviršiui ir pereina į vadinamąją S (angl. *surface*) būseną. Padidėjus peptido koncentracijai paviršiuje bei jų santykiui su lipidais, melitinas persiorientuoja įsiterpdamas į membraną ir formuodamas toroidines poras - T būseną. Šis persiorientavimas keičia amidinių virpesių (Am-I ir Am-

II) dipolio momento (TDM) vektorių kryptis (16B pav.), todėl gali būti panaudojama tyrimuose IRRAS, PM-IRRAS ar SEIRAS metodais, kaip peptido orientacijos žymuo.

Yra žinoma, jog melitino veikimui yra svarbus pomembraninis rezervuaras.[246] Todėl melitino sąveikai su membrana stebėti in situ ATR-SEIRAS metodu, buvo panaudojamos hBLM ir tBLM modelinių membranų sistemos, kurių duomenys palyginti tarpusavyje. Šios sistemos skiriasi tuo, jog pomembraninis rezervuaras susiformuoja tik tBLM atveju.

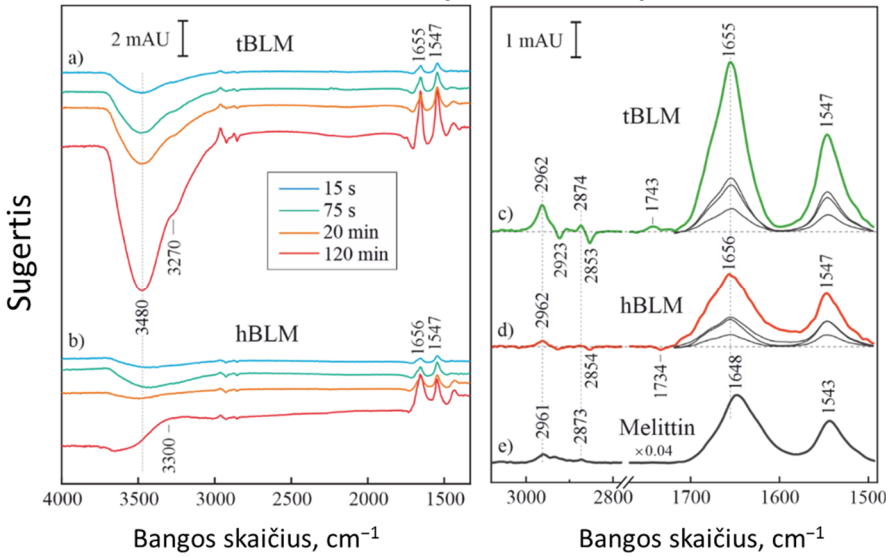


17 paveikslas. Melitino SEIRAS spektrai po 15 s, 75 s, 20 min ir 120 min inkubacijos tBLM ir hBLM sistemose. Skirtuminių spektrų gavimui naudoti suformuotos membranos (tBLM arba hBLM) spektrai. Kairė: a) tBLM ir b) hBLM spektrai skirtingais inkubavimo su melitinu laikais be vandens korekcijos. Dešinė: c) tBLM ir d) hBLM spektrai su vandens korekcija; e) melitino vandenyje ATR-FTIR spektras.

Iš palygintų SEIRAS duomenų buvo nustatyta, jog melitinas jau pirmosiomis sekundėmis sąveikauja su abiejų tipų membrana išstumdamas vandenį. Ilgiau inkubuojant, melitinui priskiriamų juostų intensyvumas didėja hBLM bei tBLM sistemose, tačiau vanduo toliau išstumiamas tik prie pakabinamos lipidinės membranos (17 pav. karė). Tuo grindžiamas tolimesnis melitino kaupimasis pomembraniniame rezervuare išstumiant vandeniline sąveika surištas vandens molekules (ν(OH), 3480 $cm^{-1}$) ir taip suardant pomembranio vandens struktūrą.

Neigiamos smailės ties 2923 $cm^{-1}$ ir 2853 $cm^{-1}$, priskiriamos $\nu_{as}(CH_2)$ ir $\nu_s(CH_2)$ WC14 junginiui, rodo SAM molekulių orientacijos pokyčius į vertikalesnę padėtį. Šie pokyčiai didesni melitinui sąveikaujant su tBLM (17 pav., dešinė). Amidinių virpesių regiono analizė parodė, jog melitinas

sąveikaudamas su tBLM ir hBLM sistemomis yra α-spiralės būsenoje nuo pat sąveikos pradžios. Išmatuota Am-I smailės padėtis 1655 $cm^{-1}$ yra pasislinkusi lyginant su Am-I 1648 $cm^{-1}$ smailės dažniu, išmatuotu tirpale esančio laisvu melitinu (17c,d,e pav.). Pastarasis dažnis būdingas išsivyniojusios antrinės struktūros baltymams.[239–242]

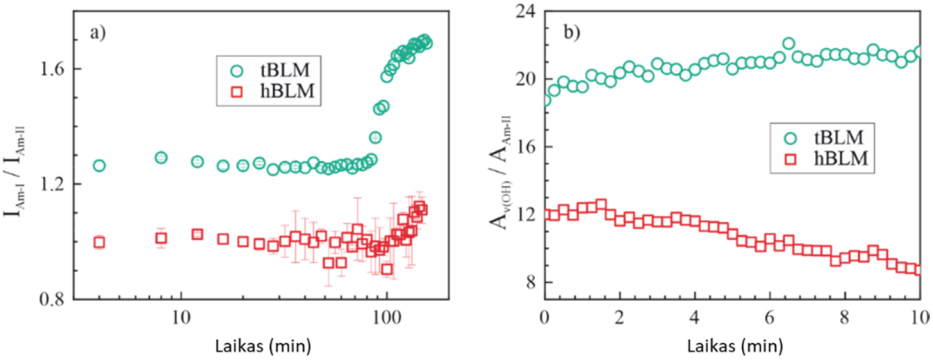


18 paveikslas. a) Melitino sąveikos su tBLM ir hBLM Am-I/Am-II santykio kitimo laike kreivės. b) ν(OH)/Am-II kitimas laike suskaičiuotas absoliučioms integralinėms vertėms.

Įvertinus melitino amidinių ryšių santykio kitimą laike, buvo parodyta, jog pirmosiomis melitino sąveikos su membrana minutėmis išstumiamo vandens kiekis yra beveik du kartus didesnis tBLM nei hBLM sistemoje (18b pav.). Be to, tBLM vandens atstūmimas toliau didėja, melitinui kaupiantis membranos defektuose ir pomembraninėje erdvėje, kai tuo tarpu hBLM atveju vandens atstūmimas mažėja. Galimai dėl to, jog vandens pašalinimas yra sukeltas peptidų agregacijos ant membranos paviršiaus. Didesnis Am-I/Am-II santykis tBLM atveju, patvirtina labiau vertikalią melitino orientaciją paviršiaus atveju. Inkubuojant ilgiau 90 minučių, melitinas ima agreguotis su lipidais, ir membrana yra suardoma.

## Išvados

1. Naudojant IMHA/fragmento mišinį formuojami tvarkingesni monosluoksniai su stipresne amidinių grupių vandenilinio ryšio sąveika nei 100% IMHA.
2. Im žiedo valentiniai (=C–H) 3115 ir 3150 $cm^{-1}$ virpesiai grįžtamai slenkasi veikiami potencialo. Nustatytas potencialo priklausomybės dažniui poslinkio vertės lygios atitinkamai –10.4 ir –6.3 $cm^{-1}V^{-1}$. Dažnių kitimas priskiriamas susilpnėjusiai Im žiedo ir gretimų vandens molekulių vandenilinių ryšių sąveikai.
3. Nustatyta, jog iš WC14 ir βME formuojamas amorfinės būsenos monosluoksnis su netvarkingai išsidėsčiusiomis alkilo grandinėmis. tBLM formuojamas dviem etapais, pirmiausia lipidų pūslelės adsorbuojasi SAM paviršiuje išstumdamos paviršinį vandenį, po to, dėl sąveikos su WC14 alkilo grandinėmis, jos išsilieja ir suformuoja plokščią membraną. Proceso trukmė ~60 minučių.
4. Pirmą kartą SEIRAS metodu tirtas potencialo poveikis pomembraninei vandens struktūrai. Nustatyta, jog ties –0.4 V (Ag/AgCl) potencialu pomembraninio vandens padaugėja. Potencialui grįžtant į teigiamą pomembraninio vandens mažėja pradedant mažiausiai vandeniliniai ryšiais surištomis molekulėmis.
5. Panaudojus spektroskopinį žymenį (MHP), nustatyta SAM ir vidinio tBLM vandens rezervuaro dielektrinės konstantos vertė ~30.
6. SEIRA spektroskopijos tyrimu parodyta, jog pagrindinis membranos savitosios varžos kitimo faktorius yra jonų koncentracijos pasikeitimas. Jonų pomembraniniame rezervuare daugėja pH kintant iš rūgštinės į neutralią.
7. SEIRAS metodu patvirtinta melitino netvarkingos struktūros transformacija į alfa spiralę per mažiau nei 15 s sąveikaujant su modelinėmis membranomis. Ilgiau sąveikaujant, melitinas ima kauptis pomembraniniame rezervuare išstumdamas vandenį. Melitinas sąveikaudamas su tBLM išstumia dvigubai daugiau vandens nei hBLM atveju.

## THESIS SUPPORTING PUBLICATIONS

1. **Pudžaitis, V.**; Talaikis, M.; Sadzevičienė, R.; Labanauskas, L.; Niaura, G. Electrochemical SEIRAS Analysis of Imidazole Ring Functionalized Self-Assembled Monolayers. *Materials 2022, 15(20), 7221;* https://doi.org/10.3390/ma15207221.
2. **Pudžaitis, V.**; Talaikis, M.; Valinčius, G.; Niaura, G. Formation of tethered bilayer lipid membranes on gold surface probed by in situ SEIRAS. Chemija 2023, Vol 34 No 1; https://doi.org/10.6001/chemija.2023.34.1.1.
3. Shivabalan, A. P.; Ambrulevicius, F.; Talaikis, M.; **Pudžaitis, V.**; Niaura, G.; Valincius. G. Effect of pH on Electrochemical Impedance Response of Tethered Bilayer Lipid Membranes: Implications for Quantitative Biosensing. *Chemosensors 2023, 11(8), 450;* https://doi.org/10.3390/chemosensors11080450.

## PUBLICATIONS IN PREPARATION

1. Tumenas, S.; Tadas Ragaliauskas, T.; Ambrulevicius, F.; **Pudzaitis, V.**; Talaikis, M.; Niaura, N.; Su, Z.; Lipkowski, L.; and Valincius, G. In situ monitoring of melittin adsorption and incorporation into the phospholipid bilayer membrane. *Biochimica et Biophysica Acta* (2023). *In preparation.*
2. **Pudžaitis, V.**; Talaikis, M.; Niaura, G. Surface-Enhanced Infrared Absorption Spectroscopy (SEIRAS) of Submembrane Water Confinement in DOPC/Cholesterol tBLM at Electrified Surfaces. *In preparation.*

## OTHER PUBLICATIONS

1. Bagdzevičienė, J.; **Pudžaitis, V.**; Bliujienė, A.; Petrauskas, G. 2023. Technological Investigations of an Enamel-Decorated Drinking Horn Handle from Maudžiorai Cemetery in Western Lithuania. *Journal of Archaeological Science: Reports*. Volume 48, 103915, https://doi.org/10.1016/j.jasrep.2023.103915.
2. Boguzaite, R.; Ratautaite, V.; Mikoliunaite, L.; **Pudzaitis, V.**; Ramanaviciene, A.; Ramanavicius, A. 2021. Towards Analytical Application of Electrochromic Polypyrrole Layers Modified by Phenothiazine Derivatives. *Journal of Electroanalytical Chemistry* 886. https://doi.org/10.1016/j.jelechem.2021.115132.

3. Skirgaila, R.; **Pudzaitis, V.**; Paliksa, S.; Vaitkevicius, M.; Janulaitis, A. 2013. Compartmentalization of Destabilized Enzyme-MRNA-Ribosome Complexes Generated by Ribosome Display: A Novel Tool for the Directed Evolution of Enzymes. *Protein Engineering Design & Selection* 26 (7): 453–61. https://doi.org/10.1093/protein/gzt017.
4. Urbach, C.; Evrard, C.; **Pudzaitis, V.**; Fastrez, J.; Soumillion, P.; Declercq, J. P. 2009. Structure of PBP-A from Thermosynechococcus Elongatus, a Penicillin-Binding Protein Closely Related to Class A Beta-Lactamases. *Journal of Molecular Biology* 386 (1): 109–20. https://doi.org/10.1016/j.jmb.2008.12.001.

## PRESENTATION OF RESULTS AT CONFERENCES

1. **V. Pudžaitis**, G. Niaura, Savitvarkio monosluoksnio formavimosi ant aukso paviršiaus in situ tyrimas ATR-SEIRAS metodu. 9th conference of doctoral students and young researchers. „FizTeCh2019“, 2019 October 23-24., Vilnius, Lithuania: (Oral presentation) p. 2
2. **V. Pudžaitis**, M. Talaikis, G. Niaura, Self-assembling monolayer (SAM) and a model membrane (tBLM) formation observation on a gold surface by ATR-SEIRAS. 10th conference of doctoral students and young researchers. „FizTeCh2019“, 2019 October 22-23., Vilnius, Lithuania: (Oral presentation) p. 14
3. **V. Pudžaitis**, M. Talaikis, G. Niaura, In situ probing of SAM and tBLM layer formation on nanostructured gold by ATR-SEIRAS. Advanced Properties and Processes in Optoelectronic Materials and Systems „APROPOS 17“, 2020 September 29 – October 1 d., 2020 Vilnius, Lithuania: Abstract Book p. 71-72.
4. **V. Pudžaitis**, M. Talaikis, G. Niaura, ATR-SEIRAS probes dielectric environment of the submembrane layer of the tethered bilayer lipid membranes (tBLMs). 65th International Conference for Students of Physics and Natural Sciences „Open readings 2022“, 2022 March 15-18, 2022 Vilnius, Lithuania: Abstract book p. 190.
5. **V. Pudžaitis**, M. Talaikis, G. Niaura, Electrochemical SEIRAS Analysis of Imidazole Ring Functionalized Self-Assembled Monolayers. International conference of chemistry and chemical technology 2023, CCT-2023, March 10th Vilnius, Lithuania: Abstract book p. 101.
6. **V. Pudžaitis**, M. Talaikis, G. Niaura, Formation of tethered bilayer lipid membranes on gold surface probed by SEIRAS. 66th International Conference for Students of Physics and Natural Sciences „Open readings 2023“, 2023 April 15-18, Vilnius, Lithuania: Abstract book p. 309.

# REFERENCES


1. Growth, Dissolution and Pattern Formation in Geosystems. Jamtveit, B., Meakin, P., (Springer Netherlands, 1999). doi:10.1007/978-94-015-9179-9.
2. Morasch, M., Liu, J., Dirscherl, C.F. et al. Heated gas bubbles enrich, crystallize, dry, phosphorylate and encapsulate prebiotic molecules. *Nat. Chem.* **11**, 779–788 (2019). https://doi.org/10.1038/s41557-019-0299-5.
3. Marchand, A., Weijs, J. H., Snoeijer, J. H. & Andreotti, B. Why is surface tension a force parallel to the interface? (2012) doi:10.48550/ARXIV.1211.3854.
4. Belardi, B. & Fletcher, D. A. One and one is not two: taking a fresh look at membrane interfaces. *Nat Rev Mol Cell Biol* **19**, 747–748 (2018). https://doi.org/10.1038/s41580-018-0057-3.
5. Gözen, I. & Jesorka, A. Instrumental Methods to Characterize Molecular Phospholipid Films on Solid Supports. *Anal. Chem.* **84**, 822–838 (2012). doi:10.1021/ac203126f.
6. Ataka, K., Stripp, S. T. & Heberle, J. Surface-enhanced infrared absorption spectroscopy (SEIRAS) to probe monolayers of membrane proteins. *Biochimica et Biophysica Acta - Biomembranes* **1828**, 2283–2293 (2013). doi.org/10.1016/j.bbamem.2013.04.026.
7. Iyer, A. H., Krishna Deepak, R. N. V. & Sankararamakrishnan, R. Imidazole Nitrogens of Two Histidine Residues Participating in N–H···N Hydrogen Bonds in Protein Structures: Structural Bioinformatics Approach Combined with Quantum Chemical Calculations. *J. Phys. Chem. B* **122**, 1205–1212 (2018). doi:10.1021/acs.jpcb.7b11737.
8. Liao, S.-M., Du, Q.-S., Meng, J.-Z., Pang, Z.-W. & Huang, R.-B. The multiple roles of histidine in protein interactions. *Chemistry Central Journal* **7**, 44 (2013). doi:10.1186/1752-153X-7-44.
9. Su, Z., Leitch, J. J. & Lipkowski, J. Electrode-supported biomimetic membranes: An electrochemical and surface science approach for characterizing biological cell membranes. *Current Opinion in Electrochemistry* **12**, 60–72 (2018). doi: 10.1016/j.coelec.2018.05.020.
10. Rebaud, S., Maniti, O. & Girard-Egrot, A. P. Tethered bilayer lipid membranes (tBLMs): Interest and applications for biological membrane investigations. *Biochimie* **107**, 135–142 (2014). doi:10.1016/j.biochi.2014.06.021.
11. Šablinskas, V. & Čeponkus, J. Modernioji molekulių virpesinė spektrometrija. 240 (2014).
12. Poelman, D. R. *Emission characteristics of water in the universe*. (University of Groningen, 2007).
13. *Introduction to Infrared and Raman Spectroscopy*. (Elsevier, 1975). doi:10.1016/B978-0-12-182552-2.X5001-3.

14. Sinclair, R. G., McKay, A. F., Myers, G. S. & Jones, R. N. The Infrared Absorption Spectra of Unsaturated Fatty Acids and Esters [1]. *J. Am. Chem. Soc.* **74**, 2578–2585 (1952). doi.org/10.1021/ja01130a035.
15. Nyquist, R. Alkenes and Other Compounds Containing C=C Double Bonds. in *Interpreting Infrared, Raman, and Nuclear Magnetic Resonance Spectra* vol. 1 55–91 (Elsevier, 2001). doi.org/10.1016/B978-012523475-7/50168-6.
16. Ye, S., Li, H., Yang, W. & Luo, Y. Accurate Determination of Interfacial Protein Secondary Structure by Combining Interfacial-Sensitive Amide I and Amide III Spectral Signals. *J. Am. Chem. Soc.* **136**, 1206–1209 (2014). doi.org/10.1021/ja411081t.
17. Myshakina, N. S., Ahmed, Z. & Asher, S. A. Dependence of Amide Vibrations on Hydrogen Bonding. *J. Phys. Chem. B* **112**, 11873–11877 (2008). doi: 10.1021/jp8057355.
18. Barth, A. Infrared spectroscopy of proteins. *Biochimica et Biophysica Acta (BBA) - Bioenergetics* **1767**, 1073–1101 (2007).
19. Dioumaev, A. K. & Braiman, M. S. Modeling Vibrational Spectra of Amino Acid Side Chains in Proteins: The Carbonyl Stretch Frequency of Buried Carboxylic Residues. *J. Am. Chem. Soc.* **117**, 10572–10574 (1995).
20. Salehpour, S. & Dubé, M. A. Reaction Monitoring of Glycerol Step-Growth Polymerization Using ATR-FTIR Spectroscopy. *Macromolecular Reaction Engineering* **6**, 85–92 (2012).
21. Gillgren, T. & Gorzsás, A. A one-pot set-up for real-time reaction monitoring by FTIR spectroscopy. *Wood Sci. Technol.* **50**, 567–580 (2016).
22. Leadbeater, N. E. In situ reaction monitoring of microwave-mediated reactions using IR spectroscopy. *Chem. Commun.* **46**, 6693 (2010).
23. González, M. G., Cabanelas, J. C. & Baselga, J. Applications of FTIR on Epoxy Resins - Identification, Monitoring the Curing Process, Phase Separation and Water Uptake. in *Infrared Spectroscopy - Materials Science, Engineering and Technology* (ed. Theophanides, T.) (InTech, 2012). doi:10.5772/36323.
24. Hartstein, A., Kirtley, J. R. & Tsang, J. C. Enhancement of the Infrared Absorption from Molecular Monolayers with Thin Metal Overlayers. *Physical Review Letters* **45**, 201–204 (1980).
25. Osawa, M. Surface-Enhanced Infrared Absorption. in *Near-Field Optics and Surface Plasmon Polaritons* 163–187 (Springer Berlin Heidelberg). doi:10.1007/3-540-44552-8_9.
26. Janneh, M. Bandwidth Optimisation and Frequency Tuning of Plasmonic Functionalised Metasurfaces for Optical Sensing of Chemical and Biological Substances. *Procedia Engineering* 5 (2016).
27. Bjerke, A. E. & Griffiths, P. R. Surface-Enhanced Infrared Absorption Spectroscopy of *p* -Nitrothiophenol on Vapor-Deposited Platinum Films. *Appl. Spectrosc.* **56**, 1275–1280 (2002).
28. López-Lorente, Á. I., Wang, P. & Mizaikoff, B. Towards label-free mid-infrared protein assays: in-situ formation of bare gold nanoparticles for surface

enhanced infrared absorption spectroscopy of bovine serum albumin. *Microchim Acta* **184**, 453–462 (2017).
29. Fleischmann, M., Hendra, P. J. & McQuillan, A. J. Raman spectra of pyridine adsorbed at a silver electrode. *Chemical Physics Letters* **26**, 163–166 (1974).
30. Jeanmaire, D. L. & Van Duyne, R. P. Surface raman spectroelectrochemistry. *Journal of Electroanalytical Chemistry and Interfacial Electrochemistry* **84**, 1–20 (1977).
31. Hatta, A., Ohshima, T. & Suetaka, W. Observation of the enhanced infrared absorption of p-nitrobenzoate on Ag island films with an ATR technique. *Applied Physics A Solids and Surfaces* **29**, 71–75 (1982).
32. Hatta, A., Suzuki, Y. & Suetaka, W. Infrared absorption enhancement of monolayer species on thin evaporated Ag films by use of a Kretschmann configuration: Evidence for two types of enhanced surface electric fields. *Applied Physics A Solids and Surfaces* **35**, 135–140 (1984).
33. Osawa, M. Dynamic Processes in Electrochemical Reactions Studied by Surface-Enhanced Infrared Absorption Spectroscopy (SEIRAS). *Bulletin of the Chemical Society of Japan* **70**, 2861–2880 (1997).
34. Wang, H.-L., You, E.-M., Panneerselvam, R., Ding, S.-Y. & Tian, Z.-Q. Advances of surface-enhanced Raman and IR spectroscopies: from nano/microstructures to macro-optical design. *Light. Sci. Appl.* **10**, 161 (2021).
35. Langer, J. *et al.* Present and Future of Surface-Enhanced Raman Scattering. *ACS Nano* **14**, 28–117 (2020).
36. Pettinger, B., Picardi, G., Schuster, R. & Ertl, G. Surface-enhanced and STM-tip-enhanced Raman spectroscopy at metal surfaces. *Single Molecules* **3**, 285–294 (2002).
37. Dong, L. *et al.* Nanogapped Au Antennas for Ultrasensitive Surface-Enhanced Infrared Absorption Spectroscopy. *Nano Lett.* **17**, 5768–5774 (2017).
38. Su, H.-S., Chang, X. & Xu, B. Surface-enhanced vibrational spectroscopies in electrocatalysis: Fundamentals, challenges, and perspectives. *Chinese Journal of Catalysis* **43**, 2757–2771 (2022).
39. Osawa, M., Ataka, K.-I., Yoshii, K. & Nishikawa, Y. Surface-Enhanced Infrared Spectroscopy: The Origin of the Absorption Enhancement and Band Selection Rule in the Infrared Spectra of Molecules Adsorbed on Fine Metal Particles. *Applied Spectroscopy* **47**, 1497–1502 (1993).
40. Miyake, H., Hosono, E., Osawa, M. & Okada, T. Surface-enhanced infrared absorption spectroscopy using chemically deposited Pd thin film electrodes. *Chemical Physics Letters* **428**, 451–456 (2006).
41. Perry, D. A. *et al.* Surface-Enhanced Infrared Absorption on Elongated Nickel Nanostructures. *J. Phys. Chem. Lett.* **4**, 3945–3949 (2013).
42. Jensen, T. R., Van Duyne, R. P., Johnson, S. A. & Maroni, V. A. Surface-Enhanced Infrared Spectroscopy: A Comparison of Metal Island Films with Discrete and Nondiscrete Surface Plasmons. *Appl. Spectrosc.* **54**, 371–377 (2000).

43. Aroca, R. *Surface-Enhanced Vibrational Spectroscopy*. (Wiley, 2006). doi:10.1002/9780470035641.
44. *Encyclopedia of Biophysics*. (Springer Berlin Heidelberg, 2013). doi:10.1007/978-3-642-16712-6.
45. Xia, L. *et al.* Visualized method of chemical enhancement mechanism on SERS and TERS: Visualized method of chemical enhancement mechanism. *J. Raman Spectrosc.* **45**, 533–540 (2014).
46. Prati, S., Sciutto, G., Bonacini, I. & Mazzeo, R. New Frontiers in Application of FTIR Microscopy for Characterization of Cultural Heritage Materials. *Topics in Current Chemistry* **374**, 26 (2016).
47. Miki, A., Ye, S. & Osawa, M. Surface-enhanced IR absorption on platinum nanoparticles: an application to real-time monitoring of electrocatalytic reactions. *Chemical Communications* **2**, 1500–1501 (2002).
48. Dumas, P., Tobin, R. G. & Richards, P. L. Study of adsorption states and interactions of CO on evaporated noble metal surfaces by infrared absorption spectroscopy. *Surface Science* **171**, 579–599 (1986).
49. Persson, B. N. J. & Ryberg, R. Vibrational interaction between molecules adsorbed on a metal surface: The dipole-dipole interaction. *Phys. Rev. B* **24**, 6954–6970 (1981).
50. Persson, B. N. J. & Ryberg, R. Collective vibrational modes in isotopic mixtures of CO adsorbed on Cu (100). *Solid State Communications* **36**, 613–617 (1980).
51. Zhang, Z. & Imae, T. Study of Surface-Enhanced Infrared Spectroscopy. *Journal of Colloid and Interface Science* **233**, 99–106 (2001).
52. Sigrist, J. A., Lins, E. S., Morhart, T. A., Briggs, J. L. & Burgess, I. J. Optimization of a Commercial Variable Angle Accessory for Entry Level Users of Electrochemical Attenuated Total Reflection Surface-Enhanced Infrared Absorption Spectroscopy (ATR-SEIRAS). *Applied Spectroscopy* **73**, 1394–1402 (2019).
53. Suzuki, Y., Osawa, M., Hatta, A. & Suëtaka, W. Mechanism of absorption enhancement in infrared ATR spectra observed in the Kretschmann configuration. *Applied Surface Science* **33–34**, (1988).
54. Ataka, K. & Heberle, J. Biochemical applications of surface-enhanced infrared absorption spectroscopy. *Analytical and Bioanalytical Chemistry* **388**, 47–54 (2007).
55. Delgado, J. M., Orts, J. M., Pérez, J. M. & Rodes, A. Sputtered thin-film gold electrodes for in situ ATR-SEIRAS and SERS studies. *Journal of Electroanalytical Chemistry* **617**, 130–140 (2008).
56. Andvaag, I. R., Morhart, T. A., Clarke, O. J. R. & Burgess, I. J. Hybrid Gold-Conductive Metal Oxide Films for Attenuated Total Reflectance Surface Enhanced Infrared Absorption Spectroscopy. *ACS Applied Nano Materials* **2**, 1274–1284 (2019).
57. Brenner, A. & Riddell, G. E. Nickel plating on steel by chemical reduction. *Journal of Research of the National Bureau of Standards* **37**, 31 (1946).

58. Miyake, H., Ye, S. & Osawa, M. Electroless deposition of gold thin films on silicon for surface-enhanced infrared spectroelectrochemistry. *Electrochemistry Communications* **4**, 973–977 (2002).
59. Magagnin, L., Maboudian, R. & Carraro, C. Gold deposition by galvanic displacement on semiconductor surfaces: Effect of substrate on adhesion. *Journal of Physical Chemistry B* **106**, 401–407 (2002).
60. Porter, L. A., Choi, H. C., Ribbe, A. E. & Buriak, J. M. *Controlled Electroless Deposition of Nanostructured Precious Metal Films on Germanium Surfaces*.
61. Todeschini, M., Bastos da Silva Fanta, A., Jensen, F., Wagner, J. B. & Han, A. Influence of Ti and Cr Adhesion Layers on Ultrathin Au Films. *ACS Appl. Mater. Interfaces* **9**, 37374–37385 (2017).
62. Yan *et al.* Ubiquitous Strategy for Probing ATR Surface-Enhanced Infrared Absorption at Platinum Group Metal−Electrolyte Interfaces. *J. Phys. Chem. B* **109**, 7900–7906 (2005).
63. Bjerke, A. E., Griffiths, P. R. & Theiss, W. Surface-Enhanced Infrared Absorption of CO on Platinized Platinum. *Analytical Chemistry* **71**, 1967–1974 (1999).
64. Park, S., Wieckowski, A. & Weaver, M. J. Electrochemical Infrared Characterization of CO Domains on Ruthenium-Decorated Platinum Nanoparticles. *J. Am. Chem. Soc.* **125**, 2282–2290 (2003).
65. Pearce, H. A. & Sheppard, N. Possible importance of a "metal-surface selection rule" in the interpretation of the infrared spectra of molecules adsorbed on particulate metals; infrared spectra from ethylene chemisorbed on silica-supported metal catalysts. *Surface Science* **59**, 205–217 (1976).
66. Greenler, R. G. Infrared Study of Adsorbed Molecules on Metal Surfaces by Reflection Techniques. *The Journal of Chemical Physics* **44**, 310–315 (1966).
67. E. Y. Jiang. Introduction to Modern. *Thermo Electron Corporation, Madison, 2003* **2**, 1–6 (2003).
68. Wang, J. Modified electrodes for electrochemical sensors. *Electroanalysis* **3**, 255–259 (1991).
69. Chen, D. & Li, J. Interfacial design and functionization on metal electrodes through self-assembled monolayers. *Surface Science Reports* **61**, 445–463 (2006).
70. McGillivray, D. J. *et al.* Molecular-scale structural and functional characterization of sparsely tethered bilayer lipid membranes. *Biointerphases* **2**, 21–33 (2007).
71. Polavarapu, P. L. Ab initio vibrational Raman and Raman optical activity spectra. *The Journal of Physical Chemistry* **94**, 8106–8112 (1990).
72. Kakkar, A. K. Nano-Organometallics: Heterogenizing Homogeneous Catalysts via Thin Film Methodology. *Chemical Reviews* **102**, 3579–3588 (2002).
73. Bain, C. D. & Whitesides, G. M. Depth sensitivity of wetting: monolayers of .omega.-mercapto ethers on gold. *Journal of the American Chemical Society* **110**, 5897–5898 (1988).

74. Laibinis, P. E. & Whitesides, G. M. Self-assembled monolayers of n-alkanethiolates on copper are barrier films that protect the metal against oxidation by air. *Journal of the American Chemical Society* **114**, 9022–9028 (1992).
75. Torres, N. *et al.* Stability of antibacterial self-assembled monolayers on hydroxyapatite. *Acta Biomaterialia* **6**, 3242–3255 (2010).
76. Love, J. C., Estroff, L. A., Kriebel, J. K., Nuzzo, R. G. & Whitesides, G. M. Self-Assembled Monolayers of Thiolates on Metals as a Form of Nanotechnology. *Chemical Reviews* **105**, 1103–1170 (2005).
77. Chaki, N. K. & Vijayamohanan, K. Self-assembled monolayers as a tunable platform for biosensor applications. *Biosensors and Bioelectronics* **17**, 1–12 (2002).
78. Soda, K. Structural and thermodynamic aspects of the hydrophobic effect. *Advances in Biophysics* **29**, 1–54 (1993).
79. Špandyreva, M., Kuodis, Z. & Niaura, G. Sum frequency generation spectroscopy probing of formation of self-assembled monolayers from thiols with terminal phenylalanine ring and intrachain amide groups. *Chemija* **29**, 219–226 (2018).
80. Aleknavičienė, I., Talaikis, M., Budvytyte, R. & Valincius, G. The Impact of an Anchoring Layer on the Formation of Tethered Bilayer Lipid Membranes on Silver Substrates. *Molecules* **26**, 6878 (2021). doi:https://doi.org/10.3390/molecules26226878.
81. Watson, H. Biological membranes. *Essays in Biochemistry* **59**, 43–69 (2015).
82. Cooper, G. M. *The cell: a molecular approach.* (ASM Press [u.a.], 2000).
83. Lehninger, A. L., Nelson, D. L. & Cox, M. M. *Lehninger principles of biochemistry*. (W.H. Freeman, 2005).
84. Ikonen, E. Cellular cholesterol trafficking and compartmentalization. *Nat. Rev. Mol. Cell Biol.* **9**, 125–138 (2008).
85. Chapman, D. Phase transitions and fluidity characteristics of lipids and cell membranes. *Quart. Rev. Biophys.* **8**, 185–235 (1975).
86. Ottova-Leitmannova, A. *Advances in planar lipid bilayers and liposomes.* (Elsevier, 2006).
87. Sackmann, E. Supported Membranes: Scientific and Practical Applications. *Science* **271**, 43–48 (1996).
88. McConnell, H. M., Tamm, L. K. & Weis, R. M. Periodic structures in lipid monolayer phase transitions. *Proc. Natl. Acad. Sci. U.S.A.* **81**, 3249–3253 (1984).
89. Plant, A. L. Self-assembled phospholipid/alkanethiol biomimetic bilayers on gold. *Langmuir* **9**, 2764–2767 (1993).
90. Fini, H., Hassan, Q., Noroozifar, M. & Kerman, K. Electrografting a Hybrid Bilayer Membrane via Diazonium Chemistry for Electrochemical Impedance Spectroscopy of Amyloid-β Aggregation. *Micromachines* **13**, 574 (2022).
91. Lang, H., Duschl, C. & Vogel, H. A new class of thiolipids for the attachment of lipid bilayers on gold surfaces. *Langmuir* **10**, 197–210 (1994).

92. He, L. *et al.* Tethered Bilayer Lipid Membranes Based on Monolayers of Thiolipids Mixed with a Complementary Dilution Molecule. 1. Incorporation of Channel Peptides. *Langmuir* **21**, 11666–11672 (2005).
93. Ragaliauskas, T. *et al.* Fast formation of low-defect-density tethered bilayers by fusion of multilamellar vesicles. *Biochimica et Biophysica Acta (BBA) - Biomembranes* **1859**, 669–678 (2017).
94. McGillivray, D. J. *et al.* Structure of Functional Staphylococcus aureus α-Hemolysin Channels in Tethered Bilayer Lipid Membranes. *Biophysical Journal* **96**, 1547–1553 (2009).
95. Dziubak, D. & Sek, S. Physicochemical Characterization of Sparsely Tethered Bilayer Lipid Membranes: Structure of Submembrane Water and Nanomechanical Properties. *ChemElectroChem* **8**, 2564–2571 (2021).
96. Köper, I., Schiller, S. M., Giess, F., Naumann, R. & Knoll, W. Chapter 2 Functional Tethered Bimolecular Lipid Membranes (tBLMs). in *Advances in Planar Lipid Bilayers and Liposomes* vol. 3 37–53 (Elsevier, 2006).
97. Girard-Egrot, A. P. & Maniti, O. Why Do Tethered-Bilayer Lipid Membranes Suit for Functional Membrane Protein Reincorporation? *Applied Sciences* **11**, 4876 (2021).
98. Budvytyte, R. *et al.* Structure and properties of tethered bilayer lipid membranes with unsaturated anchor molecules. *Langmuir* **29**, 8645–8656 (2013).
99. Avci, F. G., Akbulut, B. S. & Ozkirimli, E. Membrane Active Peptides and Their Biophysical Characterization. *Biomolecules* **8**, 77 (2018).
100. Dubos, R. J. Studies on a bactericidal agent extracted from a soil bacillus. *Journal of Experimental Medicine* **70**, 1–10 (1939).
101. Wang, G. Unifying the classification of antimicrobial peptides in the antimicrobial peptide database. in *Methods in Enzymology* vol. 663 1–18 (Elsevier, 2022).
102. Huan, Y., Kong, Q., Mou, H. & Yi, H. Antimicrobial Peptides: Classification, Design, Application and Research Progress in Multiple Fields. *Front. Microbiol.* **11**, 582779 (2020).
103. Li, C. *et al.* Two optimized antimicrobial peptides with therapeutic potential for clinical antibiotic-resistant Staphylococcus aureus. *European Journal of Medicinal Chemistry* **183**, 111686 (2019).
104. Jung, Y. *et al.* Envelope-deforming antiviral peptide derived from influenza virus M2 protein. *Biochemical and Biophysical Research Communications* **517**, 507–512 (2019).
105. Madanchi, H., Shoushtari, M., Kashani, H. H. & Sardari, S. Antimicrobial peptides of the vaginal innate immunity and their role in the fight against sexually transmitted diseases. *New Microbes and New Infections* **34**, 100627 (2020).
106. Neshani, A., Zare, H., Akbari Eidgahi, M. R., Khaledi, A. & Ghazvini, K. Epinecidin-1, a highly potent marine antimicrobial peptide with anticancer and immunomodulatory activities. *BMC Pharmacol Toxicol* **20**, 33 (2019).

107. Ma, R. *et al.* In Vitro and MD Simulation Study to Explore Physicochemical Parameters for Antibacterial Peptide to Become Potent Anticancer Peptide. *Molecular Therapy - Oncolytics* **16**, 7–19 (2020).
108. Fjell, C. D., Hiss, J. A., Hancock, R. E. W. & Schneider, G. Designing antimicrobial peptides: form follows function. *Nat. Rev. Drug Discov.* **11**, 37–51 (2012).
109. Koehbach, J. & Craik, D. J. The Vast Structural Diversity of Antimicrobial Peptides. *Trends in Pharmacological Sciences* **40**, 517–528 (2019).
110. He, S. *et al.* A TFPI-1 peptide that induces degradation of bacterial nucleic acids, and inhibits bacterial and viral infection in half-smooth tongue sole, Cynoglossus semilaevis. *Fish & Shellfish Immunology* **60**, 466–473 (2017).
111. Mardirossian, M. *et al.* The Host Antimicrobial Peptide Bac71-35 Binds to Bacterial Ribosomal Proteins and Inhibits Protein Synthesis. *Chemistry & Biology* **21**, 1639–1647 (2014).
112. Le, C.-F., Fang, C.-M. & Sekaran, S. D. Intracellular Targeting Mechanisms by Antimicrobial Peptides. *Antimicrob Agents Chemother* **61**, e02340-16 (2017).
113. Cruz, G. F. *et al.* Photochemically-Generated Silver Chloride Nanoparticles Stabilized by a Peptide Inhibitor of Cell Division and Its Antimicrobial Properties. *J. Inorg. Organomet. Polym.* **30**, 2464–2474 (2020).
114. Zhang, Q.-Y. *et al.* Antimicrobial peptides: mechanism of action, activity and clinical potential. *Military Med. Res.* **8**, 48 (2021).
115. Wimley, W. C. Describing the Mechanism of Antimicrobial Peptide Action with the Interfacial Activity Model. *ACS Chem. Biol.* **5**, 905–917 (2010).
116. Vácha, R. & Frenkel, D. Simulations Suggest Possible Novel Membrane Pore Structure. *Langmuir* **30**, 1304–1310 (2014).
117. Uematsu, N. & Matsuzaki, K. Polar Angle as a Determinant of Amphipathic α-Helix-Lipid Interactions: A Model Peptide Study. *Biophysical Journal* **79**, 2075–2083 (2000).
118. Yeaman, M. R. & Yount, N. Y. Mechanisms of Antimicrobial Peptide Action and Resistance. *Pharmacol. Rev.* **55**, 27–55 (2003).
119. Matsuzaki, K., Yoneyama, S. & Miyajima, K. Pore formation and translocation of melittin. *Biophysical Journal* **73**, 831–838 (1997).
120. Yang, L., Harroun, T. A., Weiss, T. M., Ding, L. & Huang, H. W. Barrel-Stave Model or Toroidal Model? A Case Study on Melittin Pores. *Biophysical Journal* **81**, 1475–1485 (2001).
121. Jafari, M., Mehrnejad, F. & Doustdar, F. Insight into the interactions, residue snorkeling, and membrane disordering potency of a single antimicrobial peptide into different lipid bilayers. *PLoS ONE* **12**, e0187216 (2017).
122. Oren, Z. & Shai, Y. Mode of action of linear amphipathic α-helical antimicrobial peptides. *Biopolymers* **47**, 451–463 (1998).
123. Guilhelmelli, F. *et al.* Antibiotic development challenges: the various mechanisms of action of antimicrobial peptides and of bacterial resistance. *Front. Microbiol.* **4**, (2013).

124. Lee, T.-H., N. Hall, K. & Aguilar, M.-I. Antimicrobial Peptide Structure and Mechanism of Action: A Focus on the Role of Membrane Structure. *CTMC* **16**, 25–39 (2015).
125. Corrêa, J. A. F., Evangelista, A. G., Nazareth, T. D. M. & Luciano, F. B. Fundamentals on the molecular mechanism of action of antimicrobial peptides. *Materialia* **8**, 100494 (2019).
126. Gazit, E., Miller, I. R., Biggin, P. C., Sansom, M. S. P. & Shai, Y. Structure and Orientation of the Mammalian Antibacterial Peptide Cecropin P1 within Phospholipid Membranes. *Journal of Molecular Biology* **258**, 860–870 (1996).
127. Hale, J. D. & Hancock, R. E. Alternative mechanisms of action of cationic antimicrobial peptides on bacteria. *Expert Review of Anti-infective Therapy* **5**, 951–959 (2007).
128. Zdaniauskiene, A. *et al.* Electrochemical Shell-Isolated Nanoparticle-Enhanced Raman Spectroscopic Characterization of SAM Formed from Alkanethiol with Imidazole Ring and Intrachain Amide Group. *unpublished.*
129. Ogawa, E. The mechanism of the isotopic exchange reactions. *BCSJ* **11**, 425–427 (1936).
130. Niaura, G. Raman Spectroscopy in Analysis of Biomolecules. in *Encyclopedia of Analytical Chemistry* (ed. Meyers, R. A.) 1–34 (Wiley, 2014). doi:10.1002/9780470027318.a0212.pub3.
131. Frisch, M. J.; Trucks, G. W.; Schlegel, H. B.; Scuseria, G. E.; Robb, M. A.; Cheeseman, J. R.; Scalmani, G.; Barone, V.; Mennucci, B.; Petersson, G. A.; Nakatsuji, H.; Caricato, M.; Li, X.; Hratchian, H. P.; Izmaylov, A. F.; Bloino, J.; Zheng, G.; Sonnenb, D. J. Gaussian 09, Revision D.01; Gaussian Inc., Wallingford, CT. (2013).
132. Talaikis, M., Eicher-Lorka, O., Valincius, G. & Niaura, G. Water-Induced Structural Changes in the Membrane-Anchoring Monolayers Revealed by Isotope-Edited SERS. *J. Phys. Chem. C* **120**, 22489–22499 (2016).
133. Dunwell, M., Yan, Y. & Xu, B. A surface-enhanced infrared absorption spectroscopic study of pH dependent water adsorption on Au. *Surface Science* **650**, 51–56 (2016).
134. Jusys, Z. & Behm, R. J. Electrooxidation of formic acid on a polycrystalline Au film electrode–A comparison with mass transport limited bulk CO oxidation and kinetically limited oxalic acid oxidation. *Journal of Electroanalytical Chemistry* **800**, 60–76 (2017).
135. Jusys, Z. & Behm, R. J. The Effect of Anions and pH on the Activity and Selectivity of an Annealed Polycrystalline Au Film Electrode in the Oxygen Reduction Reaction-Revisited. *ChemPhysChem* **20**, 3276–3288 (2019).
136. Yaguchi, M., Uchida, T., Motobayashi, K. & Osawa, M. Speciation of Adsorbed Phosphate at Gold Electrodes: A Combined Surface-Enhanced Infrared Absorption Spectroscopy and DFT Study. *Journal of Physical Chemistry Letters* **7**, 3097–3102 (2016).
137. Nowak, C., Luening, C., Knoll, W. & Naumann, R. L. C. A Two-Layer Gold Surface with Improved Surface Enhancement for Spectro-Electrochemistry

Using Surface-Enhanced Infrared Absorption Spectroscopy. *Appl. Spectrosc.* **63**, 1068–1074 (2009).
138. Wandlowski, T., Ataka, K., Pronkin, S. & Diesing, D. Surface enhanced infrared spectroscopy—Au(1 1 1-20nm)/sulphuric acid—new aspects and challenges. *Electrochimica Acta* **49**, 1233–1247 (2004).
139. Garcia-Araez, N., Rodriguez, P., Navarro, V., Bakker, H. J. & Koper, M. T. M. Structural Effects on Water Adsorption on Gold Electrodes. *The Journal of Physical Chemistry C* **115**, 21249–21257 (2011).
140. Nishikawa, Yuji., Fujiwara, Kunihiro., Ataka, Kenichi. & Osawa, Masatoshi. Surface-enhanced infrared external reflection spectroscopy at low reflective surfaces and its application to surface analysis of semiconductors, glasses, and polymers. *Analytical Chemistry* **65**, 556–562 (1993).
141. Lu, G.-Q. *et al.* In Situ FTIR Spectroscopic Studies of Adsorption of CO, $SCN^-$, and Poly( *o* -phenylenediamine) on Electrodes of Nanometer Thin Films of Pt, Pd, and Rh: Abnormal Infrared Effects (AIREs). *Langmuir* **16**, 778–786 (2000).
142. Suzuki, Y., Goto, S. & Umetsu, H. Enhancement and band distortion of the IR absorption spectra of a methanol on silver evaporated thin films in UHV-ATR configuration. *The European Physical Journal D* **33**, 201–205 (2005).
143. Su, Z.-F., Sun, S.-G., Wu, C.-X. & Cai, Z.-P. Study of anomalous infrared properties of nanomaterials through effective medium theory. *The Journal of Chemical Physics* **129**, 044707 (2008).
144. Li, S. & Hong, M. Protonation, Tautomerization, and Rotameric Structure of Histidine: A Comprehensive Study by Magic-Angle-Spinning Solid-State NMR. *J. Am. Chem. Soc.* **133**, 1534–1544 (2011).
145. Ashikawa, I. & Itoh, K. Raman spectra of polypeptides containingL-histidine residues and tautomerism of imidazole side chain. *Biopolymers* **18**, 1859–1876 (1979).
146. Matulaitienė, I., Kuodis, Z., Eicher-Lorka, O. & Niaura, G. SERS characterization of imidazole ring terminated self-assembled monolayer formed from lipoic acid histamide on silver electrode. *Journal of Electroanalytical Chemistry* **700**, 77–85 (2013).
147. Ashikawa, I. & Itoh, K. Raman scattering study on tautomerism of l-histidine. *Chem. Lett.* **7**, 681–684 (1978).
148. Matulaitienė, I., Pociūtė, E., Kuodis, Z., Eicher-Lorka, O. & Niaura, G. Interaction of 4-imidazolemethanol with a copper electrode revealed by isotope-edited SERS and theoretical modeling. *Phys. Chem. Chem. Phys.* **17**, 16483–16493 (2015).
149. Garfinkel, D. & Edsall, J. T. Raman Spectra of Amino Acids and Related Compounds. VIII. Raman and Infrared Spectra of Imidazole, 4-Methylimidazole and Histidine [1-3]. *J. Am. Chem. Soc.* **80**, 3807–3812 (1958).
150. Mesu, J. G., Visser, T., Soulimani, F. & Weckhuysen, B. M. Infrared and Raman spectroscopic study of pH-induced structural changes of l-histidine in aqueous environment. *Vibrational Spectroscopy* **39**, 114–125 (2005).

151. Martusevičius, S., Niaura, G., Talaikyté, Z. & Razumas, V. Adsorption of l-histidine on copper surface as evidenced by surface-enhanced Raman scattering spectroscopy. *Vibrational Spectroscopy* **10**, 271–280 (1996).
152. Carter, D. A. & Pemberton, J. E. Raman spectroscopy and vibrational assignments of 1- and 2-methylimidazole. *J. Raman Spectrosc.* **28**, 939–946 (1997).
153. Takeuchi, H. Raman structural markers of tryptophan and histidine side chains in proteins. *Biopolymers* **72**, 305–317 (2003).
154. Miura, T., Satoh, T., Hori-i, A. & Takeuchi, H. Raman marker bands of metal coordination sites of histidine side chains in peptides and proteins. *J. Raman Spectrosc.* **29**, 41–47 (1998).
155. Kim, M., Hohman, J. N., Serino, A. C. & Weiss, P. S. Structural Manipulation of Hydrogen-Bonding Networks in Amide-Containing Alkanethiolate Monolayers via Electrochemical Processing. *J. Phys. Chem. C* **114**, 19744–19751 (2010).
156. Kuodis, Z. *et al.* Reflection Absorption Infrared Spectroscopy Characterization of SAM Formation from 8-Mercapto-N-(phenethyl)octanamide Thiols with Phe Ring and Amide Groups. *Molecules* **25**, 5633 (2020).
157. Saini, G. S. S. *et al.* Vibrational spectroscopic and density functional theory studies of chloranil–imidazole interaction. *Vibrational Spectroscopy* **56**, 66–73 (2011).
158. Richmond, W. N., Faguy, P. W. & Weibel, S. C. An in situ infrared spectroscopic study of imidazole films on copper electrodes. *Journal of Electroanalytical Chemistry* **448**, 237–244 (1998).
159. Kumar, S., Rai, A. K., Rai, S. B. & Rai, D. K. Infrared and Raman spectra of Histidine: an ab initio DFT calculations of Histidine molecule and its different protonated forms. *Indian J. Phys.* **84**, 563–573 (2010).
160. Hasegawa, K., Ono, T. & Noguchi, T. Vibrational Spectra and Ab Initio DFT Calculations of 4-Methylimidazole and Its Different Protonation Forms: Infrared and Raman Markers of the Protonation State of a Histidine Side Chain. *J. Phys. Chem. B* **104**, 4253–4265 (2000).
161. Myshakina, N. S. & Asher, S. A. Peptide Bond Vibrational Coupling. *J. Phys. Chem. B* **111**, 4271–4279 (2007).
162. Gotoh, R. & Takenaka, T. Inductive Effect of Polar Substituents on Carbon-Hydrogen Stretching Vibrations of Aliphatic Hydrocarbons. *Nippon Kagaku Zasshi* **81**, 1504–1509 (1960).
163. Lee, S.-H., Mirkin, N. G. & Krimm, S. A quantitative anharmonic analysis of the amide A band in alpha-helical poly(L-alanine). *Biopolymers* **49**, 195–207 (1999).
164. Lee, S.-H. & Krimm, S. Ab initio-based vibrational analysis of α-poly(L-alanine). *Biopolymers* **46**, 283–317 (1998).
165. Valiokas, R., Svedhem, S., Svensson, S. C. T. & Liedberg, B. Self-Assembled Monolayers of Oligo(ethylene glycol)-Terminated and Amide Group Containing Alkanethiolates on Gold. *Langmuir* **15**, 3390–3394 (1999).

166. Lee, H.-H., Gavutis, M., Ruželė, Ž., Valiokas, R. & Liedberg, B. Mixed Self-Assembled Monolayers with Terminal Deuterated Anchors: Characterization and Probing of Model Lipid Membrane Formation. *J. Phys. Chem. B* **122**, 8201–8210 (2018).
167. Javorskis, T. *et al.* Meso-scale surface patterning of self-assembled monolayers with water. *Colloids and Surfaces A: Physicochemical and Engineering Aspects* **628**, 127353 (2021).
168. Clegg, R. S. & Hutchison, J. E. Hydrogen-Bonding, Self-Assembled Monolayers: Ordered Molecular Films for Study of Through-Peptide Electron Transfer. *Langmuir* **12**, 5239–5243 (1996).
169. Kocherbitov, V., Latynis, J., Misiūnas, A., Barauskas, J. & Niaura, G. Hydration of Lysozyme Studied by Raman Spectroscopy. *J. Phys. Chem. B* **117**, 4981–4992 (2013).
170. Nelson, P. N. Chain Length and Thermal Sensitivity of the Infrared Spectra of a Homologous Series of Anhydrous Silver(I) *n* -Alkanoates. *International Journal of Spectroscopy* **2016**, 1–9 (2016).
171. Allara, D. L. & Nuzzo, R. G. Spontaneously Organized Molecular Assemblies. 2. Quantitative Infrared Spectroscopic Determination of Equilibrium Structures of Solution-Adsorbed. *Langmuir* **1**, 52–66 (1985).
172. Clegg, R. S. & Hutchison, J. E. Control of Monolayer Assembly Structure by Hydrogen Bonding Rather Than by Adsorbate−Substrate Templating. *J. Am. Chem. Soc.* **121**, 5319–5327 (1999).
173. Toyama, A., Ono, K., Hashimoto, S. & Takeuchi, H. Raman Spectra and Normal Coordinate Analysis of the N1−H and N3−H Tautomers of 4-Methylimidazole: Vibrational Modes of Histidine Tautomer Markers. *J. Phys. Chem. A* **106**, 3403–3412 (2002).
174. Zischang, J., Lee, J. J. & Suhm, M. A. Communication: Where does the first water molecule go in imidazole? *The Journal of Chemical Physics* **135**, 061102 (2011).
175. Varghese, S., Kannam, S. K., Hansen, J. S. & Sathian, S. P. Effect of Hydrogen Bonds on the Dielectric Properties of Interfacial Water. *Langmuir* **35**, 8159–8166 (2019).
176. Montenegro, A. *et al.* Asymmetric response of interfacial water to applied electric fields. *Nature* **594**, 62–65 (2021).
177. Lipkowski, J. Building biomimetic membrane at a gold electrode surface. *Phys. Chem. Chem. Phys.* **12**, 13874 (2010).
178. Penkauskas, T. & Preta, G. Biological applications of tethered bilayer lipid membranes. *Biochimie* **157**, 131–141 (2019).
179. Jackman, J., Knoll, W. & Cho, N.-J. Biotechnology Applications of Tethered Lipid Bilayer Membranes. *Materials* **5**, 2637–2657 (2012).
180. Cornell, B. A. *et al.* A biosensor that uses ion-channel switches. *Nature* **387**, 580–583 (1997).

181. Koenig, B. W. *et al.* Neutron Reflectivity and Atomic Force Microscopy Studies of a Lipid Bilayer in Water Adsorbed to the Surface of a Silicon Single Crystal. *Langmuir* **12**, 1343–1350 (1996).
182. Basit, H. *et al.* Tethered Bilayer Lipid Membranes on Mixed Self-Assembled Monolayers of a Novel Anchoring Thiol: Impact of the Anchoring Thiol Density on Bilayer Formation. *Langmuir* **27**, 14317–14328 (2011).
183. Naumann, R. *et al.* Proton transport through a peptide-tethered bilayer lipid membrane by the H+-ATP synthase from chloroplasts measured by impedance spectroscopy. *Biosensors and Bioelectronics* **17**, 25–34 (2002).
184. Tanaka, M. & Sackmann, E. Polymer-supported membranes as models of the cell surface. *Nature* **437**, 656–663 (2005).
185. Knoll, W., Köper, I., Naumann, R. & Sinner, E.-K. Tethered bimolecular lipid membranes—A novel model membrane platform. *Electrochimica Acta* **53**, 6680–6689 (2008).
186. Valincius, G. *et al.* Enzyme Activity to Augment the Characterization of Tethered Bilayer Membranes. *J. Phys. Chem. B* **110**, 10213–10216 (2006).
187. Andersson, J., Fuller, M. A., Wood, K., Holt, S. A. & Köper, I. A tethered bilayer lipid membrane that mimics microbial membranes. *Phys. Chem. Chem. Phys.* **20**, 12958–12969 (2018).
188. Talaikis, M., Valincius, G. & Niaura, G. Potential-Induced Structural Alterations in the Tethered Bilayer Lipid Membrane-Anchoring Monolayers Revealed by Electrochemical Surface-Enhanced Raman Spectroscopy. *J. Phys. Chem. C* **124**, 19033–19045 (2020).
189. Rakovska, B. *et al.* Structure and function of the membrane anchoring self-assembled monolayers. *Langmuir* **31**, 846–857 (2015).
190. Yang, X. *et al.* Nanomaterial-Based Plasmon-Enhanced Infrared Spectroscopy. *Adv. Mater.* **30**, 1704896 (2018).
191. Li, J. *et al.* Attenuated Total Reflection Surface-Enhanced Infrared Absorption Spectroscopy: a Powerful Technique for Bioanalysis. *J. Anal. Test.* **1**, 8 (2017).
192. Pudžaitis, V., Talaikis, M., Sadzevičienė, R., Labanauskas, L. & Niaura, G. Electrochemical SEIRAS Analysis of Imidazole-Ring-Functionalized Self-Assembled Monolayers. *Materials* **15**, 7221 (2022).
193. Forbrig, E. *et al.* Monitoring the Orientational Changes of Alamethicin during Incorporation into Bilayer Lipid Membranes. *Langmuir* **34**, 2373–2385 (2018).
194. Budvytyte, R., Pleckaityte, M., Zvirbliene, A., Vanderah, D. J. & Valincius, G. Reconstitution of Cholesterol-Dependent Vaginolysin into Tethered Phospholipid Bilayers: Implications for Bioanalysis. *PLoS ONE* **8**, e82536 (2013).
195. Harder, P., Grunze, M., Dahint, R., Whitesides, G. M. & Laibinis, P. E. Molecular Conformation in Oligo(ethylene glycol)-Terminated Self-Assembled Monolayers on Gold and Silver Surfaces Determines Their Ability To Resist Protein Adsorption. *J. Phys. Chem. B* **102**, 426–436 (1998).
196. Kobayashi, M. & Sakashita, M. Morphology dependent anomalous frequency shifts of infrared absorption bands of polymer crystals: Interpretation in terms

of transition dipole–dipole coupling theory. *The Journal of Chemical Physics* **96**, 748–760 (1992).
197. Vanderah, D. J., Pham, C. P., Springer, S. K., Silin, V. & Meuse, C. W. Characterization of a Series of Self-Assembled Monolayers of Alkylated 1-Thiaoligo(ethylene oxides) $_{4-8}$ on Gold. *Langmuir* **16**, 6527–6532 (2000).
198. Vanderah, D. J., Meuse, C. W., Silin, V. & Plant, A. L. Synthesis and Characterization of Self-Assembled Monolayers of Alkylated 1-Thiahexa(ethylene oxide) Compounds on Gold. *Langmuir* **14**, 6916–6923 (1998).
199. Vanderah, D. J., Valincius, G. & Meuse, C. W. Self-Assembled Monolayers of Methyl 1-Thiahexa(ethylene oxide) for the Inhibition of Protein Adsorption. *Langmuir* **18**, 4674–4680 (2002).
200. Vanderah, D. J. *et al.* Structural Variations and Ordering Conditions for the Self-Assembled Monolayers of HS($CH_2CH_2O$)$_{3-6}$$CH_3$. *Langmuir* **19**, 3752–3756 (2003).
201. Vanderah, D. J. *et al.* Isostructural Self-Assembled Monolayers. 1. Octadecyl 1-Thiaoligo(ethylene oxides). *Langmuir* **19**, 2612–2620 (2003).
202. Vanderah, D. J. *et al.* Isostructural Self-Assembled Monolayers. 2. Methyl 1-(3-Mercaptopropyl)-oligo(ethylene oxide)s. *Langmuir* **20**, 1311–1316 (2004).
203. Xue, X.-K. *et al.* Practically Modified Attenuated Total Reflection Surface-Enhanced IR Absorption Spectroscopy for High-Quality Frequency-Extended Detection of Surface Species at Electrodes. *Anal. Chem.* **80**, 166–171 (2008).
204. Porter, M. D., Bright, T. B., Allara, D. L. & Chidsey, C. E. D. Spontaneously organized molecular assemblies. 4. Structural characterization of n-alkyl thiol monolayers on gold by optical ellipsometry, infrared spectroscopy, and electrochemistry. *J. Am. Chem. Soc.* **109**, 3559–3568 (1987).
205. Laibinis, P. E. *et al.* Comparison of the structures and wetting properties of self-assembled monolayers of n-alkanethiols on the coinage metal surfaces, copper, silver, and gold. *J. Am. Chem. Soc.* **113**, 7152–7167 (1991).
206. Parikh, A. N. & Allara, D. L. Quantitative determination of molecular structure in multilayered thin films of biaxial and lower symmetry from photon spectroscopies. I. Reflection infrared vibrational spectroscopy. *The Journal of Chemical Physics* **96**, 927–945 (1992).
207. Sunder, S., Cameron, D. G., Casal, H. L., Boulanger, Y. & Mantsch, H. H. Infrared and raman spectra of specifically deuterated 1,2-dipalmitoyl-sn-glycero-3-phosphocholines. *Chemistry and Physics of Lipids* **28**, 137–147 (1981).
208. Ma, G. & Allen, H. C. DPPC Langmuir Monolayer at the Air−Water Interface: Probing the Tail and Head Groups by Vibrational Sum Frequency Generation Spectroscopy. *Langmuir* **22**, 5341–5349 (2006).
209. Feng, R.-J., Li, X., Zhang, Z., Lu, Z. & Guo, Y. Spectral assignment and orientational analysis in a vibrational sum frequency generation study of DPPC monolayers at the air/water interface. *The Journal of Chemical Physics* **145**, 244707 (2016).

210. Meuse, C. W., Niaura, G., Lewis, M. L. & Plant, A. L. Assessing the Molecular Structure of Alkanethiol Monolayers in Hybrid Bilayer Membranes with Vibrational Spectroscopies. *Langmuir* **14**, 1604–1611 (1998).
211. Sprik, M. Hydrogen bonding and the static dielectric constant in liquid water. *The Journal of Chemical Physics* **95**, 6762–6769 (1991).
212. Kontogeorgis, G. M. *et al.* Water structure, properties and some applications – A review. *Chemical Thermodynamics and Thermal Analysis* **6**, 100053 (2022).
213. Fumagalli, L. *et al.* Anomalously low dielectric constant of confined water. *Science* **360**, 1339–1342 (2018).
214. Su, Z., Juhaniewicz-Debinska, J., Sek, S. & Lipkowski, J. Water Structure in the Submembrane Region of a Floating Lipid Bilayer: The Effect of an Ion Channel Formation and the Channel Blocker. *Langmuir* **36**, 409–418 (2020).
215. Uchida, T., Osawa, M. & Lipkowski, J. SEIRAS studies of water structure at the gold electrode surface in the presence of supported lipid bilayer. *Journal of Electroanalytical Chemistry* **716**, 112–119 (2014).
216. Binder, H. Water near lipid membranes as seen by infrared spectroscopy. *Eur. Biophys. J.* **36**, 265–279 (2007).
217. Ewing, G. E. Thin Film Water. *J. Phys. Chem. B* **108**, 15953–15961 (2004).
218. Brubach, J.-B., Mermet, A., Filabozzi, A., Gerschel, A. & Roy, P. Signatures of the hydrogen bonding in the infrared bands of water. *The Journal of Chemical Physics* **122**, 184509 (2005).
219. Disalvo, E. A. & Frias, M. A. Water State and Carbonyl Distribution Populations in Confined Regions of Lipid Bilayers Observed by FTIR Spectroscopy. *Langmuir* **29**, 6969–6974 (2013).
220. Bonn, M., Bakker, H. J., Tong, Y. & Backus, E. H. G. No Ice-Like Water at Aqueous Biological Interfaces. *Biointerphases* **7**, 20 (2012).
221. Bülbül, E. *et al.* Confined hydration in nanometer-graded plasma polymer films: Insights from surface-enhanced infrared absorption spectroscopy. *Surfaces and Interfaces* **23**, 100922 (2021).
222. Burgess, I. *et al.* Electric Field-Driven Transformations of a Supported Model Biological Membrane—An Electrochemical and Neutron Reflectivity Study. *Biophysical Journal* **86**, 1763–1776 (2004).
223. Matyszewska, D. *et al.* PM-IRRAS Studies of DMPC Bilayers Supported on Au(111) Electrodes Modified with Hydrophilic Monolayers of Thioglucose. *Langmuir* **32**, 1791–1798 (2016).
224. Juhaniewicz-Dębińska, J., Konarzewska, D. & Sęk, S. Effect of Interfacial Water on the Nanomechanical Properties of Negatively Charged Floating Bilayers Supported on Gold Electrodes. *Langmuir* **35**, 9422–9429 (2019).
225. Valincius, G. & Mickevicius, M. Tethered Phospholipid Bilayer Membranes. in *Advances in Planar Lipid Bilayers and Liposomes* vol. 21 27–61 (Elsevier, 2015).
226. Skoda, M. W. A., Jacobs, R. M. J., Willis, J. & Schreiber, F. Hydration of Oligo(ethylene glycol) Self-Assembled Monolayers Studied Using Polarization Modulation Infrared Spectroscopy. *Langmuir* **23**, 970–974 (2007).

227. Malysheva, L., Onipko, A., Valiokas, R. & Liedberg, B. First-Principle DFT and MP2 Modeling of Infrared Reflection−Absorption Spectra of Oriented Helical Ethylene Glycol Oligomers. *J. Phys. Chem. B* **109**, 13221–13227 (2005).
228. Matulaitienė, I., Kuodis, Z., Matijoška, A., Eicher-Lorka, O. & Niaura, G. SERS of the Positive Charge Bearing Pyridinium Ring Terminated Self-Assembled Monolayers: Structure and Bonding Spectral Markers. *J. Phys. Chem. C* **119**, 26481–26492 (2015).
229. Park, J.-G. *et al.* Interfacial and Electrokinetic Characterization of IPA Solutions Related to Semiconductor Wafer Drying and Cleaning. *J. Electrochem. Soc.* **153**, G811 (2006).
230. Spinner, E. 718. Vibration-spectral band assignments for the pyridinium ion: pyridine deuteriochloride and 1-methylpyridinium chloride. *J. Chem. Soc.* 3870 (1963) doi:10.1039/jr9630003870.
231. Shivabalan, A. P. *et al.* Effect of pH on Electrochemical Impedance Response of Tethered Bilayer Lipid Membranes: Implications for Quantitative Biosensing. *Chemosensors* **11**, 450 (2023).
232. Zieleniecki, J. L. *et al.* Cell-Free Synthesis of a Functional Membrane Transporter into a Tethered Bilayer Lipid Membrane. *Langmuir* **32**, 2445–2449 (2016).
233. Vockenroth, I. K. *et al.* Stable insulating tethered bilayer lipid membranes. *Biointerphases* **3**, FA68–FA73 (2008).
234. Kuchinka, E. & Seelig, J. Interaction of melittin with phosphatidylcholine membranes. Binding isotherm and lipid head-group conformation. *Biochemistry* **28**, 4216–4221 (1989).
235. Leveritt, J. M., Pino-Angeles, A. & Lazaridis, T. The Structure of a Melittin-Stabilized Pore. *Biophysical Journal* **108**, 2424–2426 (2015).
236. Irudayam, S. J., Pobandt, T. & Berkowitz, M. L. Free Energy Barrier for Melittin Reorientation from a Membrane-Bound State to a Transmembrane State. *J. Phys. Chem. B* **117**, 13457–13463 (2013).
237. Almeida, P. F. & Pokorny, A. Mechanisms of Antimicrobial, Cytolytic, and Cell-Penetrating Peptides: From Kinetics to Thermodynamics. *Biochemistry* **48**, 8083–8093 (2009).
238. Huang, H. W. Action of Antimicrobial Peptides: Two-State Model. *Biochemistry* **39**, 8347–8352 (2000).
239. Frey, S. & Tamm, L. K. Orientation of melittin in phospholipid bilayers. A polarized attenuated total reflection infrared study. *Biophysical Journal* **60**, 922–930 (1991).
240. Kong, J. & Yu, S. Fourier Transform Infrared Spectroscopic Analysis of Protein Secondary Structures. *Acta Biochim. Biophys. Sinica* **39**, 549–559 (2007).
241. Jackson, M. & Mantsch, H. H. The Use and Misuse of FTIR Spectroscopy in the Determination of Protein Structure. *Critical Reviews in Biochemistry and Molecular Biology* **30**, 95–120 (1995).

242. Cooper, E. A. & Knutson, K. Fourier Transform Infrared Spectroscopy Investigations of Protein Structure. in *Physical Methods to Characterize Pharmaceutical Proteins* (eds. Herron, J. N., Jiskoot, W. & Crommelin, D. J. A.) vol. 7 101–143 (Springer US, 1995).
243. Grossutti, M., Leitch, J. J., Seenath, R., Karaskiewicz, M. & Lipkowski, J. SEIRAS Studies of Water Structure in a Sodium Dodecyl Sulfate Film Adsorbed at a Gold Electrode Surface. *Langmuir* **31**, 4411–4418 (2015).
244. Krimm, S. & Bandekar, J. Vibrational Spectroscopy and Conformation of Peptides, Polypeptides, and Proteins. in *Advances in Protein Chemistry* vol. 38 181–364 (Elsevier, 1986).
245. Lavialle, F., Adams, R. G. & Levin, I. W. Infrared spectroscopic study of the secondary structure of melittin in water, 2-chloroethanol, and phospholipid bilayer dispersions. *Biochemistry* **21**, 2305–2312 (1982).
246. Juhaniewicz, J. & Sek, S. Atomic Force Microscopy and Electrochemical Studies of Melittin Action on Lipid Bilayers Supported on Gold Electrodes. *Electrochimica Acta* **162**, 53–61 (2015).

# INFORMATION ABOUT AUTHOR

**Vaidas Pudžaitis**

1982-06-03 Naujoji Akmenė, Lithuania

## Education

| | |
|---|---|
| 2017 – 2023 | Doctoral degree, Center for Physical Sciences and Technology |
| 2005 – 2007 | Master degree in biochemistry, VU Faculty of Chemistry. |
| 2001 – 2005 | Bachelor degree in biochemistry, VU Faculty of Chemistry. |
| 1996 – 2001 | Franciscan high school in Kretinga |

## Work experience

| | |
|---|---|
| 2020/05 – 2023/09 | Group leader at the Science Research Department of LNDM Pranas Gudynas Restoration Center. |
| 2016/06 – 2019/12 | Sales manager at JSC Interlux. |
| 2010/01 – 2016/04 | Sales and service manager at OU Bruker Baltic. |
| 2008/09 – 2010/01 | Sales manager at JSC Grida. |
| 2007/10 – 2008/09 | Studies at UCL (Universite Catholique de Louvain), Belgium. |
| 2003/11 – 2007/09 | Junior biochemist at JSC Fermentas. |

UŽRAŠAMS

UŽRAŠAMS

UŽRAŠAMS

Vilniaus universiteto leidykla
Saulėtekio al. 9, III rūmai, LT-10222 Vilnius
El. p. info@leidykla.vu.lt, www.leidykla.vu.lt
bookshop.vu.lt, journals.vu.lt
Tiražas 20 egz.